Data-Driven Neuromechanical Modeling, Estimation, and Control for Hand-Assistive Robotic Interfaces

by

Avinash Baskaran

A dissertation submitted to the Graduate Faculty of
Auburn University
in partial fulfillment of the
requirements for the Degree of
Doctor of Philosophy

Auburn, Alabama
May 10, 2025

Keywords: Computational Neuromechanics, Rehabilitation Robotics, Optimal Control

Approved by

Dr. Chad G. Rose, Chair, Assistant Professor of Mechanical Engineering
Dr. Brendon Allen, Assistant Professor of Mechanical Engineering
Dr. Michael Zabala, Associate Professor of Mechanical Engineering
Dr. Gopikrishna Deshpande, Professor of Electrical and Computer Engineering

Abstract

Mechanical interactions at the hand affect its entire neuromuscular circuit — from hand kinematics and peripheral nervous activation, to motor and somatosensory cortex activation, to cognition and decision making. Neuromechanics is the approach of understanding mechanical interactions as the biproduct of these subsystems. An important domain of neuromechanical analysis is the development of hand-assistive robotics, a diverse range of technologies that facilitate neuromuscular rehabilitation for individuals with motor impairments, sensory feedback to accelerate skill acquisition, and assistance to support functional movement and strength. Hand assistive devices are typically designed for locally stationary neuromechanical states such as kinematics and muscle activation, providing maximally effective interactions only under fixed experimental conditions. In practice, neuromechanical states like fatigue and motor learning impose nonstationary transition dynamics that can impede interaction objectives and reduce performance quality. This thesis introduces a suite of computational neuromechanics tools comprising the NeuroSiGHT, NeuroMERGE, and NeuroGAIN algorithms. NeuroSiGHT integrates neuromuscular theory and topological data analysis to construct a robust partially observable Markov decision process model of stationary and nonstationary neuromechanical states from surface electromyography. NeuroMERGE refines these insights by introducing an active exploration strategy for assistive robots to estimate neuromechanical state transition dynamics unsupervised through controlled perturbations. NeuroGAIN extends this by employing generative architectures to forecast state transition dynamics and optimally evolve estimation and control strategies. To explicate its utility, the suite is validated in simulation and human participant experiments aiming at improving motor performance. The significant take-away of this thesis is reduction of neuromuscular fatigue and effort , and enhanced hand motor-cognitive efficiency in hand motor skill acquisition and performance. The neuromechanical suite enables practical neuromuscular interaction control at the hand.

Acknowledgments

The precious time I have spent as a student at Auburn has formed of lifelong friendships, pricesless insights, and a wealth of perspective. Foremost among my discoveries while at Auburn is the love I share with my wife, Katie. She has made this journey the greatest of my lifetime, and I cannot express enough my hope and optimism in taking the next steps of my journey with her. Thanking her adequaately has surely been the most challenging part of my time at Auburn and I know it will be a lifelong endeavour. I dedicate this work to my mother, whose multitasking as coach, teammate, and cheer team are unmatched. I give me deepest gratitude to my father and brother, for their support at every turn. I sincerely thank Dr. Chad G. Rose for the opportunity to study at the WeBR lab at Auburn University, and for shaping the engineer and friend that I am today. I thank my committee members, Dr. Zabala, Dr. Allen, and Dr. Deshpande for their time and effort in shaping this work and granting this degree. This work would not be possible without the generous support of funding organizations like the Alabama Space Grant Consortium, corporate partnerships including Blue Halo and Pison Technology, and interdisciplinary collaboration at Auburn with Dr. David Bevly, Dr. Scott Martin, Dr. Heidi Hausse, and Dr. Russell Mailen, as well as Curtis Hill and Steven Peeples at the Mashall Space Flight Center. Each of these individuals has supported and shaped my development as a researcher. I am sincerely grateful for the consistent support and encouragement of my peers at Auburn, including Rhet Hailey, David Hollinger, Jake Ward, and Fabian Schirmer among others. I would like to thank my friends Gunter Nawrocki and Danny Michael, for edifying, exhorting and comforting me in my faith. I would like to thank Dr. Ashish Deshpande at the University of Texas at Austin for fostering my undergraduate research experience and for connecting me to my lifelong friend and mentor, Dr. Rose. I sincerely thank Sujata Basyal for her thankless hours of checking and rechecking my math, Jonathan Ting for his wisdom and encouragement, and Kislaya Mishra for his willingness to teach and encourage me. I

would like to thank Davis Poole for lending his time and experience to my 3D printing endeavours, Zack Miller for inspiring me with his creativity, curiosity, and inginuity, and Paxton Albright for his depth of insight in working with USB webcams. I thank Ann Ryan Johnston, Patrick Neely, and David Edmondson for sharing their diligence and technical background in evaluating my presentations before conferences and interviews. I would like to thank Marissa Lazenby for her eagerness to learn mechatronics and system dynamics; it helped me brush up on the fundamentals! I thank Chaitra Gururaja, instructor of the Auburn Indian Music Ensemble for helping me connect to my culture and share it with others. Finally, I would like to acknowledge and thank Dr. Robert L. Read, my lifelong mentor and friend. I hope to have the impact on others that he had on me.

I thank my God every time I remember you. In all my prayers for all of you, I always pray with joy because of your partnership in the gospel from the first day until now, being confident of this, that he who began a good work in you will carry it on to completion until the day of Christ Jesus. - Philippians 1:3

Table of Contents

List of Tables

List of Figures

List of Acronyms

1. **sEMG** – Surface Electromyography
2. **DoF** – Degrees of Freedom
3. **HRI** – Human-Robot Interaction
4. **BBT** – Box and Block Test
5. **NM3F** – Non-negative Matrix Tri-Factorization
6. **POMDP** – Partially Observable Markov Decision Process
7. **MPC** – Model Predictive Control
8. **RL** – Reinforcement Learning
9. **EP** – Equilibrium Point
10. **EPRG** – Equilibrium Point Reference Governor
11. **ESC** – Extremum Seeking Control
12. **AGeNT** – Anthropomorphic Generalized Neuromechanical Testbed
13. **ETFE** – Empirical Transfer Function Estimate
14. **CoTS** – Commercial-Off-The-Shelf
15. **LSTM** – Long Short-Term Memory
16. **VAE** – Variational Autoencoder
17. **AR** – Accuracy and Reliability
18. **Power Grasp (PG)** – A full-hand grasp used for forceful grip, typically involving all fingers wrapped around an object (e.g., holding a hammer).

19. **Lateral Pinch (LP)** – A pinch between the thumb and the lateral side of the index finger (e.g., holding a key).

20. **Two-Finger Pinch (TP)** – A fine motor grasp involving the thumb and index finger (e.g., picking up a small object).

21. **Three-Finger Pinch (ThP)** – A precision grip using the thumb, index, and middle fingers (e.g., manipulating a pen).

22. **FPL** – Flexor Pollicis Longus

23. **FDP** – Flexor Digitorum Profundus

24. **EDC** – Extensor Digitorum Communis

25. **PT** – Pronator Teres

26. **PG** – Power Grasp

27. **LP** – Lateral Pinch

28. **TP** – Two-Finger Pinch

29. **ThP** – Three-Finger Pinch

30. **CMC** – Carpometacarpal (joint)

31. **PIP** – Proximal Interphalangeal (joint)

32. **DIP** – Distal Interphalangeal (joint)

33. **RoM** – Range of Motion

34. **I** – Intent: The motor plan or goal the user aims to execute.

35. **E** – Effort: The volitional activation level, derived from sEMG magnitude or synergy activation.

36. **F** – Fatigue: A time-frequency degradation metric of neuromuscular performance, derived from spectral shift.

37. **S** – Skill: The learned motor efficiency, modeled as reduced variability or increased precision over trials.

38. **x** – Neuromechanical state vector: Includes I, E, F, and S.

39. **f** – Transition dynamics: A function describing how neuromechanical states evolve over time.

40. **a** – Neuromuscular action or command (e.g., muscle activation)

41. **NeuroSiGHT** – Neuromechanical Simulation for Generalized Human Testing

42. **NeuroMERGE** – Neuromuscular Model-free Epistemic Risk-Guided Exploration

43. **NeuroGAIN** – Neuromechanical Generative Autoencoding Impedance Network

Chapter 1

Motivating Neuromechanical Models

This chapter motivates the development of computational neuromechanical models by highlighting the complex, individualized, and nonlinear nature of hand motor control and rehabilitation. It introduces a three-part computational suite comprising the NeuroSiGHT, NeuroMERGE, and NeuroGAIN algorithms that integrate physiological signals, control theory, and generative modeling to enable adaptive, user-specific hand assistive technologies. [1]

1.1 Fundamentals of Hand Neuromechanics

Neuromuscular impairments, such as those resulting from stroke or spinal cord injury, disrupt motor function [7, 8], sensory processing, and neuromuscular control [9], leading to difficulty performing activities of daily living (ADLs) [10]. The hand is a particularly vulnerable region due to its high degrees of freedom and complex mechanical demands in ADLs, yet it is essential to functional independence [11].

Robotic exoskeletons are being developed to assist with finger flexion and extension, enhance sensory feedback, and increase the number of therapy repetitions during early stages of recovery when neuroplasticity is high [10, 12]. These devices are also increasingly relevant in domains beyond rehabilitation, including surgery and emergency response, where reliable hand motor skills are crucial, and robotic tools are not yet reliably autonomous [13, 14].

Motor skill acquisition in such domains is bolstered by haptic feedback, which delivers tactile cues that can engage mechanisms of neuroplasticity and somatosensory reorganization [15–17].

[1] Portions of this chapter have been published in ASME Letters in Dynamic Systems and Control [1], MDPI Journal of Clinical Medicine [2], and IEEE Journal of Medical Robotics Research [3]. Portions have also been presented at the IEEE International Symposium of Medical Robotics [4], IEEE American Controls Conference [5], and IEEE Modeling Estimation and Controls Conference [6].

These cues may be cutaneous (e.g., vibrations) or kinesthetic (e.g., force-feedback), and have been shown to improve the rate and persistence of motor learning [18].

However, motor learning is not purely mechanical—it involves complex and nonlinear integration of sensory, cognitive, and dynamic control processes [19, 20]. Learners often show rapid early progress followed by plateaus [21], and excessive reliance on external feedback can undermine the transferability of learned skills [22]. To be effective, training systems must account for the evolving and individualized nature of motor performance.

Computational neuromechanics is an interdisciplinary field that seeks to model, simulate, and analyze the interactions between neural control signals, musculoskeletal dynamics, and sensory feedback during movement [23, 24]. It bridges neuroscience, biomechanics, and control theory by representing the neuromuscular system as a coupled dynamical system with sensory [25], motor [26], and mechanical components. These models capture how descending motor commands translate into muscle activations, how muscles generate forces and torques, and how those forces produce movement under biomechanical and environmental constraints [27]. Surface electromyography (sEMG) offers a window into voluntary muscle activity, providing predictive insight into intended movement as much as 200 milliseconds in advance [28, 29]. However, mapping sEMG signals to limb kinematics is challenging due to their nonlinear and context-dependent nature [30]. Neuromechanical models address this by integrating biomechanical knowledge to produce interpretable representations of motor state, enabling more robust exoskeleton control [4]. By integrating physiological signals—such as sEMG—with biomechanical simulations and control frameworks, computational neuromechanics enables estimation of internal states like motor intent, fatigue, effort, and motor learning, which are otherwise difficult to measure directly [26]. Such models support robust interpretation of sensor data [31], prediction of motor outputs, and the design of feedback or assistance strategies that adapt to user-specific dynamics [27]. They also enable synthetic experimentation on virtual limbs [32], allowing researchers to explore how changes in neuromuscular control affect performance or adaptation over time.

In addition to data-driven and statistical frameworks, biologically inspired neural control models provide critical insight into how the central nervous system may organize motor behavior [33–35]. One foundational theory is the Equilibrium Point Hypothesis (EPH), which posits that movements are generated not by directly specifying muscle forces or joint trajectories, but by shifting the limb's reference configuration—the posture at which net muscle torques are balanced [36–38]. According to this model, voluntary movement emerges from the interaction between neural command signals [39] and the passive dynamics of the musculoskeletal system [40], with sensory feedback playing a stabilizing role. Such frameworks are particularly relevant for hand modeling, where distributed coordination and impedance modulation are essential for grasp stability and fine motor control [41, 42]. Incorporating such control models into computational neuromechanics can enrich simulations by aligning them more closely with neurophysiological mechanisms [17, 43, 44], offering a complementary layer of interpretability beyond purely data-driven models.

In rehabilitation, computational neuromechanical approaches help personalize robotic interventions by modeling each user's impairments and predicting how they respond to therapy [12, 21], linking functional and neural outcomes [45]. In skill training contexts, such as surgery or remote manipulation [14], these models can provide insight into how motor skills are learned, generalized, and retained—particularly when augmented by haptic interfaces [20, 46]. This thesis extends the neuromechanics framework to a three-part computational suite that integrates classical time-frequency measurement modeling, unsupervised dynamical modeling, and generative forecasting for dexterous hand control.

1.2 Computational Neuromechanical Frameworks

Computational neuromechanics aims to model the dynamic interplay between neural signals, musculoskeletal dynamics, sensory processing, and task-level motor behavior [23, 24]. For hand function, this modeling challenge is amplified by the high degrees of freedom [47], dense sensory innervation [48], and nonlinear motor coordination involved in dexterous manipulation [49]. Effective models must account for time-varying state transitions [7], latent neuromuscular states

(such as intent, fatigue, or adaptation) [1], and measurement noise across multiple sensor modalities [16]. Frameworks developed for this purpose often span three conceptual spaces: the input space (comprising task constraints and sensor data), the model space (specifying the algorithmic or statistical modeling architecture), and the output space (describing the predicted or inferred neuromechanical states or functional metrics) [50]. Input modalities typically include surface electromyography (sEMG), kinematics, neuroimaging, and behavioral metrics from reaction time or motor tasks. Output measures span from muscle-level intent to higher-order indicators of motor performance and adaptation [20]. Models must manage not only complexity and variability in these data streams, but also computational demands and real-time feasibility [29].

For example, a comprehensive review of computational neuromechanical models used in mild traumatic brain injury (mTBI) characterization [51] which involved the screening and meta-analysis of over 800 studies and detailed extraction from 57 articles—identified four principal modeling approaches: stochastic/ANOVA models (STMs), linear regression (LNR), time–frequency decomposition (TFD), and machine learning (ML). The review revealed systematic trade-offs between interpretability, computational complexity, and adaptability. STMs offered robustness to noise and variability, making them suitable for real-time applications [52–54]; LNR provided clarity but limited expressiveness for nonlinear dynamics [55, 56]; TFD models excelled at representing transient, nonstationary processes like sEMG spectral shifts [57]; and ML models captured high-dimensional patterns but demanded large, curated datasets [58–61]. These insights generalize well to modeling of hand neuromechanics. Stochastic models remain critical for handling noisy signals such as sEMG and accelerometry, particularly under fatigue or during free-form movement [53, 62]. TFD models are ideal for analyzing time-varying muscle activations during repetitive or reactive hand tasks [57]. Machine learning, especially neural networks and decision trees, enables modeling of nonlinear relationships between multimodal sensor data and inferred motor states [59, 60], though careful tuning, feature selection, and training data diversity are essential to avoid overfitting and ensure generalizability. Linear regression and generalized linear models still

serve as valuable baselines and interpretable tools, particularly when modeling simpler movements or known biomechanical relationships [55, 63].

Signal preprocessing is a key determinant of model performance. Across the studies reviewed, preprocessing techniques such as normalization, feature selection, signal filtering, and artifact removal were critical to improving model robustness [54, 60, 64]. Signals from sEMG sensors were often band-pass filtered in the 20–450 Hz range to retain meaningful motor information while reducing electrical noise [58, 65]. Feature extraction techniques—such as mean absolute value, zero-crossing rate, and spectral entropy—enabled dimensionality reduction while preserving relevant physiological variance [66, 67]. For neuroimaging and high-dimensional inputs, principal component analysis (PCA) and independent component analysis (ICA) were frequently used [63, 68]. Data augmentation strategies such as jittering, time-warping, and spatial transformations were employed to enhance generalization, especially in ML-based studies [69, 70].

Model evaluation typically used cross-validation techniques, including k-fold (commonly 5- or 10-fold) and leave-one-out strategies, to test model generalizability [61, 71–73]. When dealing with imbalanced outcome classes—such as rare fatigue episodes or skill regression—resampling methods like SMOTE or bootstrapping were used to improve class representation [53, 55, 57]. Missing data were handled through imputation, ranging from simple mean-substitution to multiple imputation for longitudinal or multimodal datasets [59, 65, 74].

Importantly, computational constraints also shaped model choices. STM and GLM frameworks demonstrated scalability with relatively modest computational overhead [51, 53, 71]. TFD models, especially wavelet-based methods, offered favorable trade-offs between performance and complexity for frequency-rich signals like sEMG or EEG [52, 75]. ML models, while powerful, often incurred high memory usage and time complexity proportional to sample size, feature count, and network depth—making them less suitable for edge-device deployment unless optimized [69, 76]. From these findings, several broader conclusions emerge for hand neuromechanical modeling. First, modeling frameworks must be tailored not only to task demands but also to the nature of available data: simpler models may outperform complex ones when data are sparse or noisy [**aline**,

77]. Second, combining structural priors from biomechanics with data-driven adaptation (e.g., hybrid or warm-started models) enhances both interpretability and adaptability [78]. Third, effective preprocessing and feature engineering remain foundational to model robustness, regardless of the algorithm [54].

In hand-specific applications—such as assistive robotics, rehabilitation, and haptic skill training—these principles underscore the importance of computational frameworks that are physiologically grounded, robust to variability, and feasible for real-time implementation [79, 80]. The models introduced in this dissertation—NeuroSiGHT, NeuroMERGE, and NeuroGAIN—build on these insights by fusing structured neuromechanical priors with data-driven inference to enable robust estimation and control of hand neuromechanical states across diverse task conditions.

1.3 Implications for Hand Assistive Devices

The integration of computational neuromechanical modeling into the design and control of hand assistive devices offers significant opportunities for enhancing their function across both clinical and non-clinical domains. These devices—ranging from wearable robotic exoskeletons to haptic feedback systems—must interface with the highly dynamic and individualized neuromechanics of the hand, as depicted in Fig. 1.1. The models presented in this thesis enable these interfaces to be smarter, more adaptive, and better aligned with the user's internal motor state.

Robust estimation of neuromuscular intent, effort, and fatigue allows assistive devices to dynamically adjust the level of assistance provided [81, 82]. For example, by identifying when a user is intentionally initiating a grasp versus passively experiencing muscle activation, an exoskeleton can deliver graded support that encourages active engagement rather than over-reliance [29, 83]. Similarly, real-time detection of fatigue can trigger adaptive control strategies—such as modulating resistance or altering task demands—to avoid overexertion and sustain meaningful repetitions [14, 82]. The unsupervised topological modeling of motor intent dynamics to classify and adapt to complex motor behaviors without requiring extensive labeled training data [84]. Persistent attractor structures in the control space can be used to detect stable motor strategies and transitions,

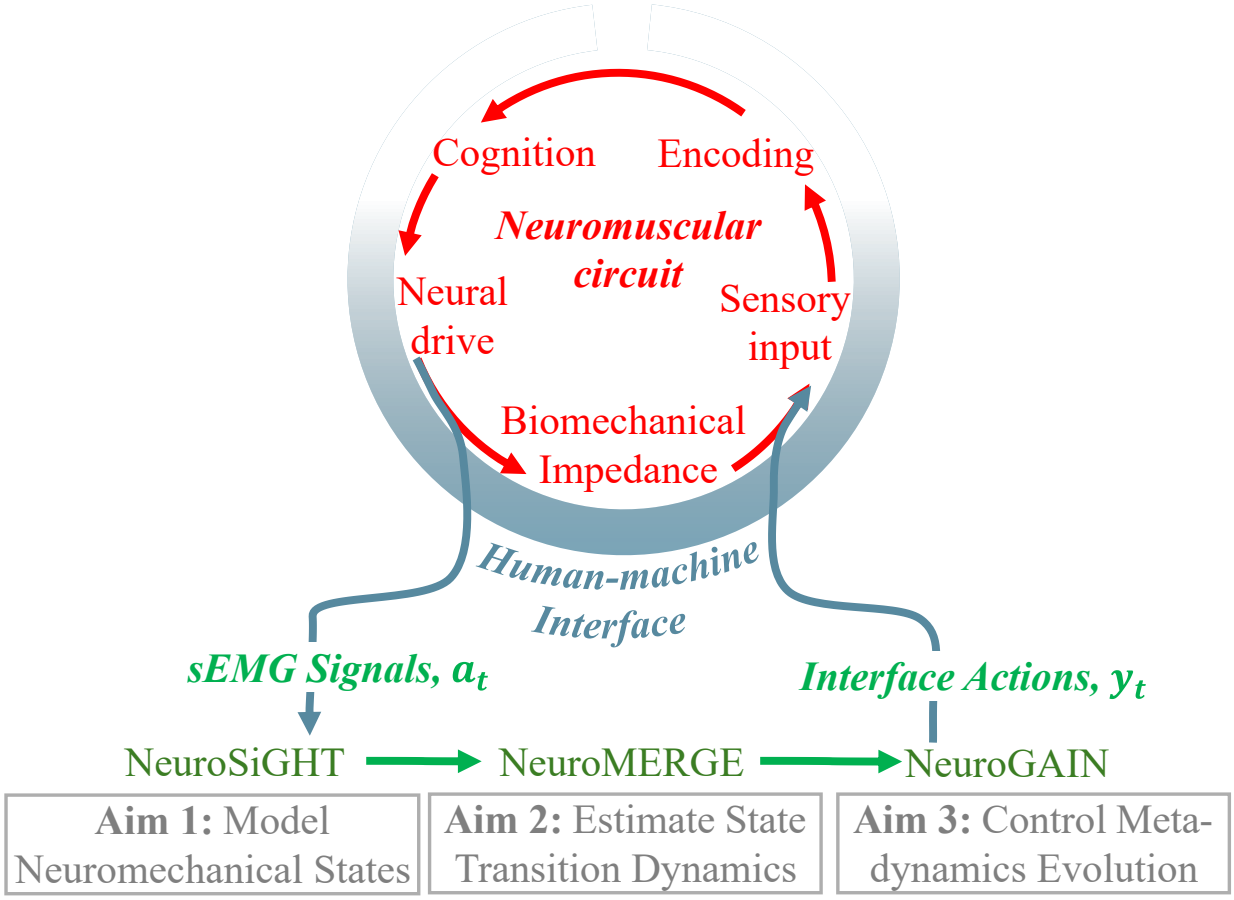

Figure 1.1: This thesis presents a computational neuromechanical suite to enhance human-machine interaction. The members of this suite are NeuroSiGHT, which models neuromechanical states, x, including intent, I, effort E, fatigue, F, and motor skill S. NeuroMERGE estimates neurmechanical state transition dynamics, f in response to feedback y and user neuromuscular action a. NeuroGAIN forecasts neuromechanical meta-dynamic evolution using a generative probabilistic framework P, for robust optimal control of hand-assistive robotic interfaces. The neuromechanical information flow of the suite is depicted in the above flowchart.

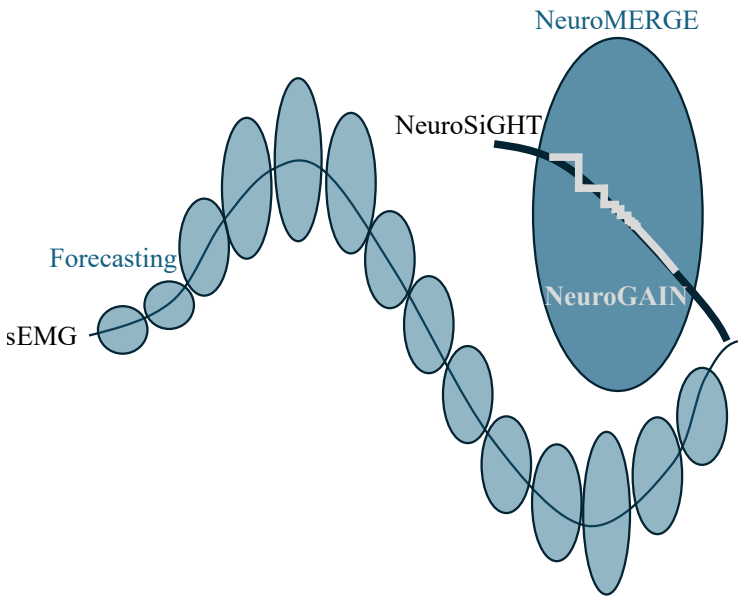

Figure 1.2: A depiction of the functional scope of each suite member in the context of generative model-predictive tracking is shown for additional clarity regarding the functionality of each member.

offering a basis for real-time progress monitoring and feedback personalization [6]. Generative models such as NeuroGAIN open new possibilities for predictive assistance [1]. By forecasting future states of motor behavior, assistive systems can preemptively shape haptic or mechanical feedback to guide the user along optimal movement trajectories [3]. This approach reduces response latency [82], improves synchronization between human and robot [29], and can enable anticipatory haptic guidance during surgical training or telepresence [14], as depicted in Fig. 1.2.

Importantly, the neuromechanical modeling framework supports both rehabilitation and augmentation [12, 24, 85]. In clinical populations, it enables more precise identification of motor deficits and the design of adaptive interventions that are both intensive and tolerable [82, 86]. In skilled operator contexts, such as teleoperation or prosthetics, it can enhance performance by stabilizing fine motor control and enriching sensory experience [83, 87]. Computational neuromechanics provides a critical foundation for the next generation of assistive and augmentative technologies [24, 88]. By embedding physiological insight into the core of control and feedback systems, these models enable devices that are not only responsive, but meaningfully aligned with the user's intent, capacity, and learning trajectory [16, 43].

1.4 Thesis Aims and Outline

This dissertation introduces a suite of computational neuromechanics tools to address fundamental aims in modeling, estimation, and control to improve HRI. These aims are:

1. Model neuromechanical states robustly across healthy participants.
2. Estimate neuromechanical state transition dynamics.
3. Control the evolution of transition dynamics (e.g., to reduce effort and fatigue and improve motor skill acquisition).

NeuroSiGHT, NeuroMERGE, and NeuroGAIN are the members of the suite, and each target the corresponding aim, as illustrated in Fig. 1.1 and 1.2 to advance robust and adaptive human-robot interaction.

NeuroSiGHT (Neuromechanical Simulation for Generalized Human Trials): A neuromechanical simulation framework that models motor performance, somatosensory processing, and skill acquisition using a structured, partially observable Markov decision process (POMDP). It incorporates principles from the Equilibrium Point Hypothesis and sEMG spectral analysis to estimate central and peripheral neuromuscular states. NeuroMERGE (Neuromechanical Model-free Epistemic Risk Guided Exploration): A framework for neuromechanical palpation, enabling assistive robots to actively probe and refine estimates of neuromechanical transition dynamics. This is achieved through controlled perturbations that improve estimation accuracy without requiring full state observability. NeuroGAIN (Neuromechanical Generative Autoencoding Impedance Network): A generative modeling strategy that forecasts neuromechanical state transitions and iteratively updates control strategies, allowing for anticipatory adaptation to changes in motor behavior or fatigue. These tools are unified by their focus on integrating structured prior knowledge with real-time adaptability, enabling robust modeling and control of both stationary and nonstationary neuromechanical states.

In Chapter 2, the development of these tools is presented, and their practical implementation is summarized in the form of algorithmic expressions. In Chapter 3, experimental validation of the

tools is summarized, including simulated and human-participant studies. In Chapter 4, simulation environments and practical embodiments of the computational models are discussed, and experiments exploring such methods are presented. Chapter 5 provides a conclusion that summarizes and contextualizes the contributions of this dissertation. Through these contributions, this thesis lays the foundation for next-generation hand assistive technologies that are not only intelligent and adaptive, but also safe, scalable, and personalized for diverse users and applications.

Chapter 2

A Novel Computational Neuromechanical Suite

This chapter presents the development and implementation of the three part computational neuromechanical suite. The suite comprises NeuroSiGHT, for computational neuromechanical modelling, NeuroMERGE, for excitation-based parameter estimation, and NeuroGAIN, for generative forecasting. Together the suite constitutes an approach for robust data-driven hand-assistive interfaces. [1]

2.1 Development and Implementation of NeuroSiGHT

NeuroSiGHT - Neuromechanical Simulation for Generalized Human Trials - is first presented. It follows an interpretation of the skin surface over superficial muscles as the nexus corresponding to the conversion of neural signals to kinematic outputs during movement. Muscle synergies, or spatiotemporal patterns in muscle activation that arise in sEMG signals, have been theorized as a potential solution space organized at the level of the central nervous system to simplify motor control problems [47]. As a model mapping neural commands to hand dynamics, it can be cast as a simulation framework for the human hand to develop hand assistive technologies.

Muscle synergies remain valid and meaningful metrics for individuals with disabilities as well, including those with spinal cord injuries (SCI) and stroke. Individuals with SCI exhibit a reduction in the number and complexity of muscle synergies due to neural damage, but partial recovery or compensatory mechanisms can result in task-specific increases in synergy numbers during rehabilitation [89]. Similarly, stroke survivors demonstrate altered and fewer muscle synergies compared to healthy individuals, reflecting impaired motor control and neural plasticity

[1] Portions of this chapter have been published in ASME Letters in Dynamic Systems and Control [1], and IEEE Journal of Medical Robotics Research [3], and have been presented at the IEEE International Symposium of Medical Robotics [4], IEEE American Controls Conference [5], and IEEE Modeling Estimation and Controls Conference [6].

[90, 91]. These synergies evolve dynamically with therapeutic interventions and exertion levels, creating substantial variability in neuromuscular signals both within and across individuals. The adaptive method proposed in this thesis was designed to overcome such intra- and inter-wearer variability by leveraging quasi-stable attractors in the synergy space. This framework enables robust unsupervised classification of motor intent, even when the number of synergies or their spatial-temporal patterns deviate significantly due to injury or recovery. By accommodating the evolving neuromechanical landscape in individuals with disabilities, this method addresses critical challenges in the design of assistive and rehabilitative robotic systems. It provides a data-efficient and user-adaptive approach for intent recognition, making it highly relevant to advancing rehabilitation technologies .

Spatial and Temporal Muscle Synergy Extraction

First, a reduced-dimensional linear measurement model of neuromuscular states, including intent, $\hat{I}$, effort, $\hat{E}$, and fatigue, $\hat{F}$, was developed. These states are selected as they can be assessed from sEMG signals alone without regard to environmental interactions, unlike motor skill. Non-negative matrix tri-factorization (NM3F) of sEMG signals is used to identify spatial and temporal neuromuscular synergies (Fig. 2.1) which encode these neuromuscular states in a low-order, domain reduced space [92]. Muscle activation modules, or synergies, can be extracted from measurements of muscle electrical activity via sEMG [93]. Neuromuscular compensation can be modeled in the domain of muscle synergies with the onset of muscle fatigue. However, while successfully demonstrating the separability of motor intent from motor activation/output level in the single linear domain of muscle synergies, adaptations in motor output level could be due either to muscle fatigue or changes in volitional effort, as shown in Fig. 2.2.

To meet the need for estimation that can separate intent, effort, and fatigue, this thesis addresses robust linear neuromuscular state estimation through an expanded probabilistic analysis of muscle spatial and temporal synergies extracted via NM3F (Fig. 2.1). It is desired to show that spatial synergy modules account for variability in intent as quasi-gaussian linear mixtures of fixed

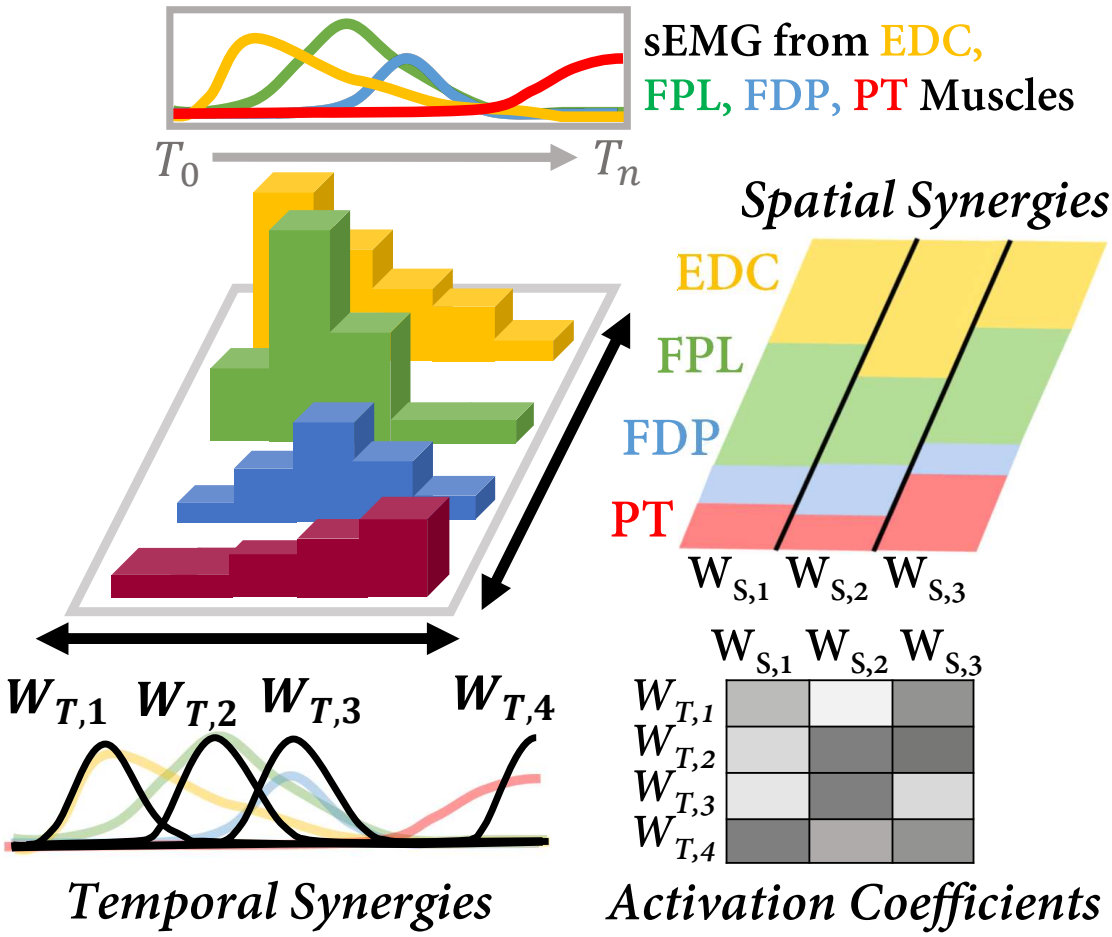

Figure 2.1: This thesis presents the estimation of neuromuscular states (hand pose intent, $\hat{I}(n)$, effort, $\hat{E}(n)$, and fatigue $\hat{F}(n)$) from spatial synergies, temporal synergies, and activation coefficients, via non-negative matrix tri-factorization (NM3F) of locally stationary epochs of sEMG data (n). Above, a schematic example is shown of the space-by-time decomposition of sEMG signals extracted from four forearm muscles.

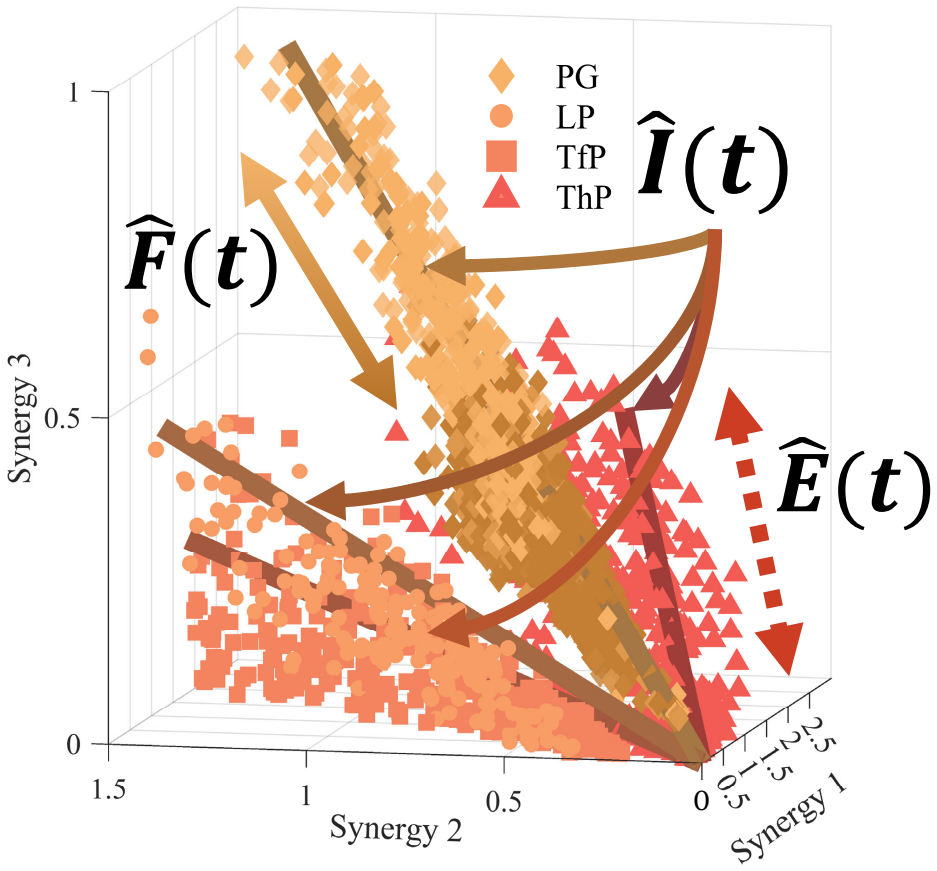

Figure 2.2: In a prior work [6], it was found that intent estimation $\hat{I}(t)$ (comprising power grasp (PG), lateral pinch (LP), two finger pinch (TP), and three finger pinch (ThP) hand poses), was linearly separable in the synergy-domain, while effort $\hat{E}(t)$ and fatigue $\hat{F}(t)$ were not linearly separable from each other without frequency terms.

reduced-dimensional vectors. Next, it is shown that activation coefficients account for variability of volitional effort. Finally, it is shown that temporal synergy modules encode time-frequency characteristics accounting for muscle fatigue. This thesis seeks to provide an alternative to high-dimensional classification, and computationally taxing nonlinear estimation methods [94].

Muscles in the forearm are activated by electrical wavelets with unique amplitude (spatial) and phase shift (temporal) characteristics. The amplitudes of muscle activation wavelets represent the contributions of measured muscles to the movement and are unique to the intended movement, and the phase and frequency measures of each wavelet represent the shape of the activation time series curve (i.e., a contribution profile). These inherently mixed amplitude (spatial) and phase (temporal) characteristics of muscle signals can be factored into temporal and spatial constituents using non-negative matrix tri-factorization (NM3F), which initializes random vectors with pre-allocated dimensions (i.e., using pre-specified number of spatial and temporal synergies). The spatial and temporal synergies are continous on the range [0 1]. The activation coefficient, which is not explicitly bounded, is used to correct the magnitude to minimize the reconstruction error. By NM3F, sEMG vectors, $V(n)$, with n denoting the measurement epoch, were decomposed into temporal $(W_{\mathrm{T}}(n))$ and spatial $(W_{\mathrm{S}}(n))$ modules with activation coefficients $(H(n))$ that reconstitute V. Despite the global non-stationary nature of sEMG signals, local independence and quasi-stationary assumptions have been found to hold for epochs less than five milliseconds, and this extends to the factors.

$$V(n) \approx W_T(n)H(n)W_S(n) \tag{2.1}$$

The method satisfies the reconstruction:

$$V(n) \approx \sum_{i=1}^{n_{TS}} \sum_{j=1}^{n_{SS}} W_T(n)H(n)W_S(n) \tag{2.2}$$

The Frobenius norm of the error was used as an objective function to minimize the reconstruction error:

$$e(n) = \sqrt{||V(n) - W_T(n)H(n)W_S(n)||^2} \tag{2.3}$$

For the isometric and dynamic hand poses evaluated, it was found that three spatial synergies and four temporal synergies were sufficient to account for over 90% of the variance of input sEMG signals. NM3F was implemented in MATLAB, with an iterative update rule on $W_{T,S}$ as defined by [95], which enabled robust on-line and off-line convergence at rates as high as 100 Hz. This thesis focuses on off-line post-hoc assessment of neuromuscular states. The update rule is:

$$W_{T,S}^{i,j} \leftarrow \frac{W_{T,S}^{i,j}}{\sqrt{\frac{[(V_{T,S}V_{T,S}^T)^+W_{T,S}]^{i,j} + [W_{T,S}W_{T,S}^T(V_{T,S}V_{T,S}^T)^-W_{T,S}]^{i,j}}{[(V_{T,S}V_{T,S}^T)^-W_{T,S}]^{i,j} + [W_{T,S}W_{T,S}^T(V_{T,S}V_{T,S}^T)^+W_{T,S}]^{i,j}}}} \tag{2.4}$$

Subject to:

$$\mathbb{E}[V] = \mathbb{E}[W_T \cdot H_T \cdot W_S] \quad = \mathbb{E}[W_T] \cdot \mathbb{E}[H_T] \cdot \mathbb{E}[W_S] \tag{2.5}$$

where

$$\begin{bmatrix} V \\ W_T \\ H \\ W_S \end{bmatrix} = \begin{bmatrix} V(t) \\ W_T(t) \\ H(t) \\ W_S(t) \end{bmatrix} \quad \forall \quad \begin{array}{l} t \in \tau + n \\ \tau \in [0, 5 \text{ ms}) \\ n >= 0 \end{array} \tag{2.6}$$

Therefore, in here, V, W_T, H, and W_S are assumed locally stationary quasi-independent variables. Thus, synergy-domain analysis provides for the separation of fixed quasi-independent spatial and temporal modules that characterize whole signal variability, as the optimization subproblems are essentially independent [95, 96], allowing for the decomposition to encode for neuromuscular states.

Modeling Intent

The first state considered here is intent, $I(t)$. Conventional time-domain linear regression modeling ($\hat{I}_*(t)$) on sEMG is often used for intent estimation in low-effort, low-fatigue conditions [97, 98]. [99]. Rather, given the bounds established in (2.1) and (2.5), the average extracted spatial synergies matrix W_{S1}, W_{S2}, and W_{S3} to represent a set of invariant statistical weightings of the n muscles used in each hand pose. This property and the local independence and quasi-stationary on the restricted domain provide that spatial synergies remain quasi-independent of temporal sEMG characteristics in local epochs (i.e., encoding uniquely spatial signal characteristics only). Thus, a weighted mixture of quasi-independent spatial synergies $\hat{I}(t)$ can provide reliable estimates of hand pose intent that remain robust to time-frequency dynamics like effort and fatigue. To realize the potential of linear analysis to estimate intent while remaining robust to fatigue and effort, per (2.7), MATLAB was used to perform pseudo-linear discriminant analysis as described in the last line of (2.7). Multiple Linear Regression is often utilized for fast, on-line classification of sEMG signals [83], because of the consistent contribution levels of each muscle to each pose (i.e., spatial synergies can be treated as locally invariant). In this pilot study, 50% of the experimental data was used to train the model, and 50% was used to test the model.

$$\begin{aligned}
\hat{I}_* &\triangleq \mathbb{E}[I|V_{M1}, V_{M2}, V_{M3}] \\
&= \sum_{i_k} i_k P(I = i_k | V_{M1}, V_{M2}, V_{M3}) \\
&\approx \sum_{i(k)} i_k P(I = i_k | W_{T,M1}, W_{T,M2}, W_{T,M3}) \\
&\Leftrightarrow b_0 + b_1 W_{S,M1}(t) + b_2 W_{S,M2}(t) + b_3 W_{S,M3}(t) = \hat{I}(t)
\end{aligned} \tag{2.7}$$

While the NM3F-based statistical framework within NeuroSiGHT enables efficient supervised estimation of neuromuscular states, it assumes access to labeled data and linear separability

in the synergy domain. However, during natural, continuous movement—especially in tasks involving fine motor control—the intent space exhibits globally stationary yet locally evolving structure, manifesting as recurring state transitions and quasi-periodic orbits. To leverage this structure without relying on labels or supervised training, NeuroSiGHT offers a second, online unsupervised intent detection approach that incorporates a topological layer to treat signal trajectories as evolving on smooth manifolds with persistent homologies. This unsupervised formulation models the dynamics of intent as stochastic transitions between attractor regions in the control space, enabling real-time classification and prediction by identifying underlying geometries and state transitions in the observed sEMG signals.

First, for limbs with fewer functional configurations (i.e. having functional configuration spaces of lower cardinality) in activities of daily living, such as the lower-limbs during locomotion, it is possible to develop robust linear mappings from sEMG signals to relevant body configurations despite reduced SNR. But for limbs with more dense configuration spaces, such as the hand, which exhibits a wide range of diverse functional configurations in activities of daily living, a robust mapping between sEMG and the configuration space is not constrained. This is because increasing the entropy of a signal that is correlated with the true behavior of a system (in this case, sEMG as it correlates with movement) reduces the mutual information of the signal and the true behavior of the system. This has an important implication with respect to varying cardinality of the true behavior (in this case, the increased number the limb functional configurations of the hand when compared to the leg).

For a system described by the stochastic mapping $f : A \rightarrow B$ where A is a control signal space (e.g., sEMG signals) and B is a target configuration space (e.g., hand joint angles or postures), with greater variability, distinct information is needed to sufficiently disambiguate neighboring states in B. As the cardinality of B increases, the precision required for the mapping to resolve each unique state also rises. That is, the greater distinctions must be made between hand poses from sEMG signals during identification with finite signal bandwidth and sensor resolution, the less accurate the identification will be. In the sEMG phase space, signal trajectories corresponding to flexion

and extension cycles during natural hand movement exhibited bounded orbits around stable basins of attraction and quasi-stable transition dynamics.

It is shown that these basins of attraction correspond to hand configurations, and that this persistent homology supports robustness constraints for unsupervised mappings despite high cardinality of the configuration space. Then a simple persistence-weighted Gaussian kernel is developed to realize the theoretical constraints in unsupervised movement classification accuracy using surface electromyography (sEMG) signals in a human participant study.

For straightforward formulation, mathematical principles are provided in symbolic form (i.e., referencing a generic system that corresponds to sEMG signals and movement) for concision and clarity. In Table 2.1, the symbols utilized in the development are mapped to real states in sEMG-based movement characterization toward a transition to describing experimental results. As muscle contractions can lead to isometric or dynamic force production of the limbs, sEMG-based inputs space cannot be constrained to be surjective to movement kinematics if environmental kinematic constraints are not also known. It is known that sEMG signals are necessarily surjective to joint mechanical impedances in both isometric and dynamic contractions through the hill-type muscle model, wherein muscle activations directly modulate joint dynamics rather than kinematics. The surjectivity of the muscle-to-movement mapping $f(v)+\eta$ is preserved through the space of mechanical impedance which directly related to kinematic outputs, and injective to kinematics when all kinematic constraints are known. Thus, the neuromechanical estimation maps sEMG to finger joint impedances, rather than flexion/extension angle. This is practical as it is robust to the task context and relevant in clinical and human-robot interaction schemes.

Let I_1 be the set of all possible configurations of the system, residing in a κ-dimensional space. The set I_1 is not explicitly parameterized beforehand. Let $V \subseteq \mathbb{R}^n$ denote the control space, defined as the space of n-dimensional control variables that influence the system configurations. The control variable is given by $v = [v_1, v_2, \ldots, v_n]^\top$, where $n < \kappa$. The control variable $v(t)$ evolves over time such that:

$$\|v(t) - v(t+1)\| \leq \xi, \tag{2.8}$$

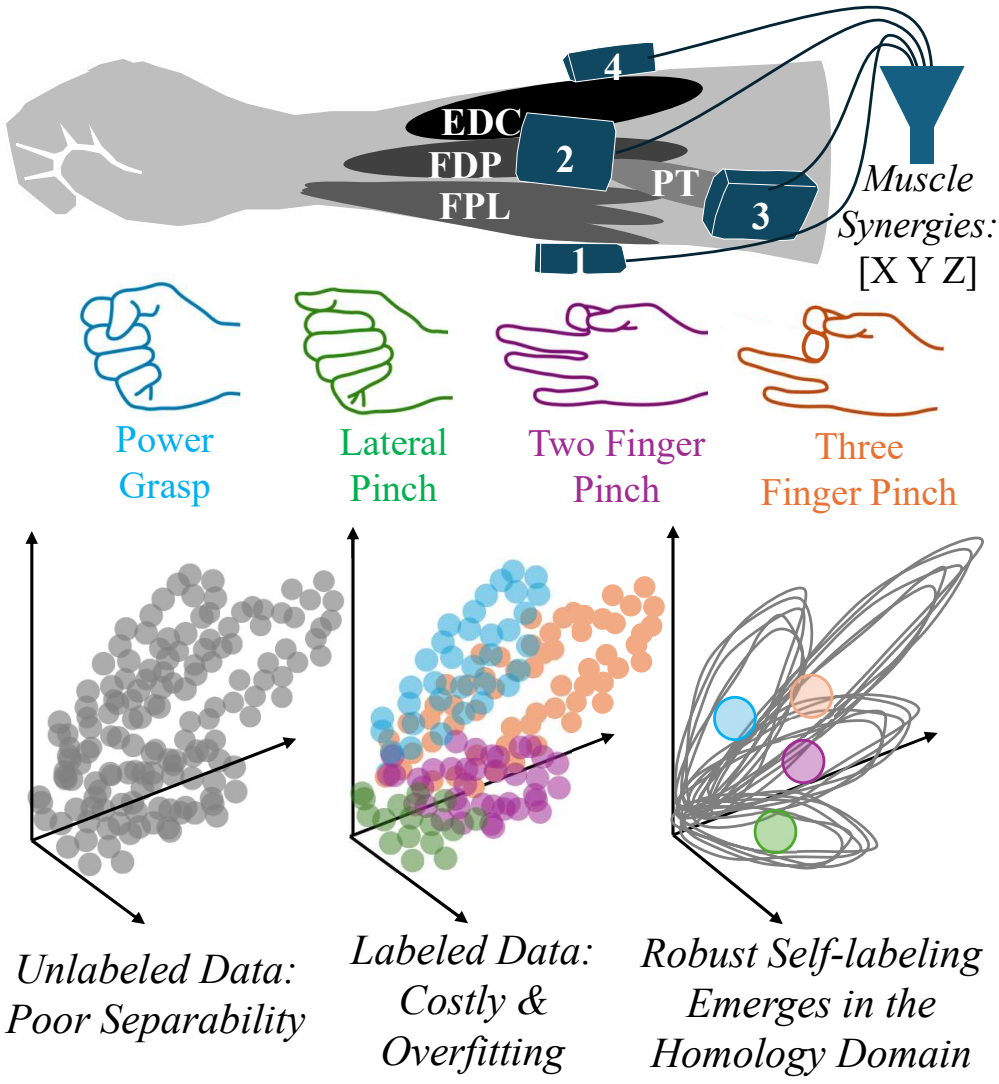

Figure 2.3: Even with the reduced dimensional input space of muscle synergies, mixed behavior can make it difficult to track intent online with unsupervised models. Supervised models are more computationally expensive and can tend toward overfitting. Yet the persistent homologies that arise in the neuromechanics of hand control motivate unsupervised statistical estimators with robustness constraints. Persistent orbits in synergies corresponding to flexion-extension action are depicted above.

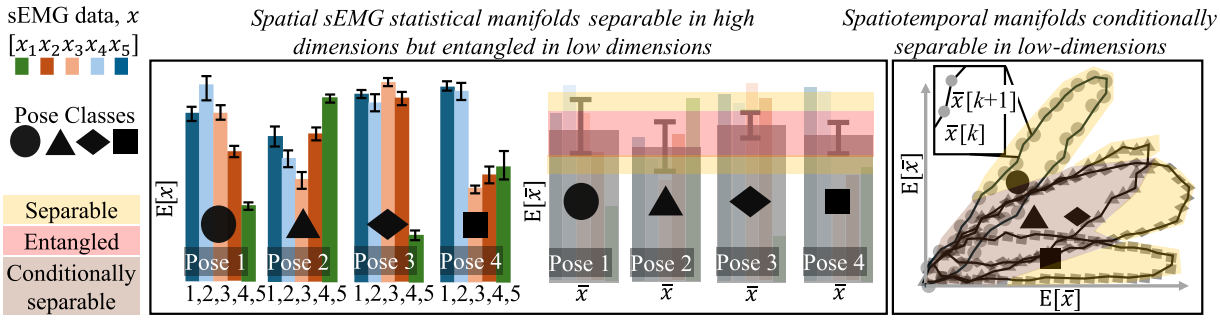

Figure 2.4: Here several schematic diagrams are provided to illustrate the differences in data separability due to channel capacity in spatial domains. In the center black box, (II), separable (B.), and entangled, i.e., un-separable (C.) statistical distributions of sEMG signals across spatial resolutions (five, corresponding to the five-D sEMG input space, and 1 corresponding to the mean of the five sEMG signals) are shown. Each of the four plots in B. correspond to one of four hand poses shown in (IB) in the left black box. The higher dimensional manifolds for each hand pose have unique geometry and are readily distinguishable. They can be identified in an sEMG data stream for online classification, but need to be pre-computed yielding a potentially overfit model.The 1-D manifolds are obfuscated; though they do not need to be pre-computed, any sEMG signals that fall within the large red obfuscation band can not be used to distinguish hand poses. It has been shown that spatiotemporal task-manifolds incorporate temporal dimensionality to mitigate task-manifold obfuscation. Here, it is proposed to use self-supervised learning in the Riemannian metric latent space to identify task-manifolds online without labels or training data.

where $\xi > 0$ is a constant.

Let $I_2 \subseteq I_1$ denote a predefined set of b target configurations:

$$I_2 = \{I_2^1, I_2^2, \ldots, I_2^b\}, \tag{2.9}$$

where $i_2^j \in I_1$ for all $j \in \{1, \ldots, b\}$.

The configurations of the system, $i_1(t) \in I_1$, are determined by a nonlinear mapping of the control variable $v(t)$, with additive noise:

$$I_1(t) = f(v(t)) + \eta(t), \tag{2.10}$$

where $f : V \to I_1$ is a nonlinear function and $\eta(t)$ is a bounded noise term. The mapping f is surjective, ensuring that all configurations in I_1 are reachable from V, and thus $I_2 \subseteq I_1$ is feasible.

The n-dimensional control space V contains b attractors, denoted by $\{A_1, A_2, \ldots, A_b\}$. Each attractor A_j corresponds to a configuration $i_2^j \in I_2$. An attractor A_j is defined as a region where trajectories of $v(t)$ stochastically converge.

The dynamics of $v(t)$ in V are modeled as a piecewise Ornstein-Uhlenbeck Process (OUP), where the dynamics are governed by the current attractor A_j:

$$dv(t) = \begin{cases} \Theta_j\big(A_j - v(t)\big)dt + \sigma_j d\mathscr{W}_t, & \text{if } v(t) \in \mathscr{R}_j, \\ 0, & \text{otherwise,} \end{cases} \tag{2.11}$$

where $\mathscr{R}_j$ is the region of influence of attractor A_j, $\Theta_j > 0$ is the mean-reversion rate, $\sigma_j > 0$ is the noise amplitude, $\mathscr{W}_t$ is a standard Wiener process. This formulation ensures that $v(t)$ oscillates around A_j with a stationary variance when within $\mathscr{R}_j$:

$$\mathrm{Var}[v(t)] = \frac{\sigma_j^2}{2\Theta_j}. \tag{2.12}$$

When the control variable $v(t)$ is within a radius r of an attractor A_j, the system transitions to the corresponding configuration $i_2^j \in I_2$:

$$\|v(t) - A_j\| \leq r \implies i_1(t) \approx i_2^j. \tag{2.13}$$

The radius r determines the tolerance for transitioning to the target configuration.

Given a time series $v = \{v(1), v(2), \ldots, v(T)\}$, the set of b n-dimensional manifolds $\{M_1, M_2, \ldots, M_b\}$ can be defined:

$$v(t) \in M_j \implies I_1(t) \approx I_2^j. \tag{2.14}$$

Each manifold $M_j \subseteq V$ represents regions in V where the control variable induces the corresponding target configuration.

The control variable $v(t)$ evolves incrementally over time $t = 1, 2, \ldots, T$, allowing iterative refinement of attractors, manifolds, and transition dynamics.

Under the conditions outlined in the system description, manifolds arising from self-symmetric graphs of Ornstein-Uhlenbeck processes (OUPs) exhibit limit cycles with regular geometric properties. These manifolds are smooth, symmetric, closed, and bounded, making them representable as conic sections in $\mathbb{R}^2$ which can be extended to higher dimensions.

Let $U \subset \mathbb{R}^2$ denote the set of all points constituting an elliptical manifold in two-dimensional space. The manifold U is defined by the implicit equation:

$$\frac{(x-x_c)^2}{a^2} + \frac{(y-y_c)^2}{b^2} = 1, \tag{2.15}$$

where (x_c, y_c) is the center of the manifold, and $a, b > 0$ represent the semi-major and semi-minor axes, respectively.

Let $I \subset U$ represent a discrete subset of points sampled from U. Each point $i \in I$ satisfies the parametric equations:

$$x(\Theta) = x_c + a\cos\Theta, \quad y(\Theta) = y_c + b\sin\Theta, \tag{2.16}$$

where $\Theta \in [0, 2\pi)$ denotes the parametric angle along the manifold. The set I is constructed by discretizing Θ into n points:

$$I = \{(x(\Theta_j), y(\Theta_j)) \mid \Theta_j = \frac{2\pi j}{n},\ j = 0, 1, \ldots, n-1\}. \tag{2.17}$$

If the elliptical limit cycle is perfectly known, high accuracy prediction of the signal trajectory from any initial state is constrained. The conditions for accurately modeling the limit cycle using a set of discrete points are described.

A minimum subset $M \subset I$ is defined as a discrete set of points sufficient to resolve the manifold. The set M must allow for unique determination of the parameters (x_c, y_c, a, b) and the orientation of the manifold. $|M| = 5$, since five independent points are required to uniquely solve the general quadratic form:

$$Ax^2 + Bxy + Cy^2 + Dx + Ey + F = 0, \tag{2.18}$$

subject to the constraint that the discriminant $B^2 - 4AC < 0$. Then for any subset $M \in E$, where U contains multiple ellipses, M represents a heteroclinic orbit that can connect elliptical trajectories, an important implication.

Let $D \subset I$ be a degenerate subset of points such that $|D| = |M| = 5$, but the points in D fail to resolve the manifold. Degeneracy occurs if: 1. The points in D are collinear, reducing the quadratic equation to a line. 2. The points in D are symmetrically distributed along a single axis, rendering the manifold's orientation indeterminate. 3. The points in D fail to provide sufficient geometric diversity to constrain the manifold's parameters.

An example of a degenerate set D is given by:

$$D = \{(0,0),(1,0),(2,0),(3,0),(4,0)\}, \tag{2.19}$$

where all points lie on a single line. This configuration fails to resolve the manifold, as the points do not span the required geometric dimensions.

Thus, it can be concluded:

- There exists a set $I \subset U$ of discrete points that constitute an manifold.
- There exists a subset $M \subset I$ with $|M| = 5$, the minimum number of points sufficient to resolve the manifold.
- There exists a degenerate subset $D \subset I$, with $|D| = |M| = 5$, but which is insufficient to resolve the manifold due to geometric degeneracy.

It can be shown that for M to be a regular set sufficient to resolve the manifold, it must describe an arc that subtends at least 180 degrees because it can then capture sufficient information about an ellipse.

A topological filter can be used to identify which points on an ellipse are degenerate in the sense that when taken in series, the degenerate points do not contain significant new information needed to resolve the ellipse, stream data from the ellipse without any foreknowledge about the

ellipse position, location, orientation, or shape and select appropriate M from the streamed points by removing the degenerate/redundant points. Topological filtration is a sequence of nested topological spaces that provides a multi-scale perspective on the structure of a dataset. Let X be a topological space. A filtration is defined as a sequence of subspaces:

$$\emptyset = X_0 \subseteq X_1 \subseteq X_2 \subseteq \cdots \subseteq X_n = X, \tag{2.20}$$

where X_j is a subspace of X for all j. For a dataset $\{x_1, x_2, \ldots, x_m\} \subseteq \mathbb{R}^n$, a filtration can be constructed using the Vietoris-Rips complex. For a given threshold ε, the Vietoris-Rips complex is defined as:

$$K_\varepsilon = \{\sigma \subseteq \{x_1, x_2, \ldots, x_m\} \mid \operatorname{diam}(\sigma) \leq \varepsilon\}, \tag{2.21}$$

where $\operatorname{diam}(\sigma)$ is the largest pairwise distance between points in the simplex σ. As ε increases, the complexes K_ε form a filtration.

Definition 1 (Simplicial Complex)**.** *A simplicial complex is a combinatorial representation of a topological space, built from simple geometric objects called simplices. A* 0*-simplex is a vertex, a* 1*-simplex is an edge, a* 2*-simplex is a triangle, and a* k*-simplex is the convex hull of* $k+1$ *affinely independent points. A simplicial complex* K *is a collection of simplices such that if* $\sigma \in K$*, all faces of* σ *are also in* K*, and if* $\sigma_1, \sigma_2 \in K$*, then* $\sigma_1 \cap \sigma_2$ *is either empty or a face of both.*

Definition 2 (Persistent Homology)**.** *Persistent homology captures the evolution of topological features such as connected components, loops, and voids across a filtration. For a filtration* $\{X_j\}_{i=0}^n$*, let* $H_k(X_j)$ *denote the* k*-th homology group, representing* k*-dimensional features. Inclusion maps* $X_j \hookrightarrow X_j$ *for* $i \leq j$ *induce homomorphisms* $f_{i,j} : H_k(X_j) \to H_k(X_j)$*. Persistent homology identifies features in* $H_k(X_j)$ *that persist across multiple* X_j*, revealing their significance in the filtration.*

Definition 3 (Birth-Death Intervals)**.** *Birth-death intervals quantify the persistence of these topological features. Let* β *be a feature in the filtration* $\{X_j\}$*. The birth of* β*, denoted* $b(\beta)$*, is the smallest index* i *such that* $\beta \in H_k(X_j)$*. The death of* β*, denoted* $d(\beta)$*, is the smallest index* j *such*

that $\beta \notin H_k(X_j)$. The persistence interval is given by:

$$[b(\beta), d(\beta)). \tag{2.22}$$

The length of the interval $d(\beta) - b(\beta)$ measures the significance of β, with longer intervals representing more robust topological features. Features with short persistence are often treated as noise. These birth-death intervals are visualized using persistence diagrams or barcode plots, providing a compact summary of the dataset's topological structure.

Let $I = \{x_1, x_2, \ldots, x_n\}$ be a set of points sampled from a piecewise smooth manifold M embedded in $\mathbb{R}^2$. Construct the Vietoris-Rips complex $K_\varepsilon(S)$ for a given threshold $\varepsilon > 0$. A simplex σ is included in $K_\varepsilon(S)$ if and only if the distance between all points in σ is less than or equal to ε. For sufficiently small ε, the simplices in $K_\varepsilon(S)$ form a combinatorial representation of the local geometry of M.

Since M is piecewise smooth, each segment of M can be locally approximated by a k-dimensional affine subspace. For a sufficiently dense sampling, the simplices in $K_\varepsilon(S)$ cover this local structure, preserving the connectivity and curvature of M within the resolution ε. Thus, the Vietoris-Rips complex $K_\varepsilon(S)$ captures the k-dimensional simplices that approximate the local structure of the manifold M.

Assumption 1. *The system trajectory $v(t)$ in the control space V evolves smoothly under the dynamics described earlier, ensuring that the resulting sampled trajectory points form non-degenerate simplices in the Vietoris-Rips filtration. Specifically, the points sampled from $v(t)$ do not align collinearly or symmetrically globally, leading to the dominance of degenerate simplices.*

Proposition 1. *For a system trajectory represented by a piecewise smooth manifold, the largest simplices (necessarily, triangles) in the Vietoris-Rips complex correspond to the regions of maximum curvature or transition points between conic sections.*

Proof: Let $M \subset \mathbb{R}^2$ be a piecewise smooth manifold, and $I = \{x_1, x_2, \ldots, x_n\} \subset M$ a dense sampling. For a threshold $\varepsilon > 0$, the Vietoris-Rips complex $K_\varepsilon(S)$ includes a simplex $\sigma = \{x_{i_1}, x_{i_2}, \ldots, x_{i_k}\}$

if:

$$\|x_{i_j} - x_{i_l}\| \leq \varepsilon \quad \forall 1 \leq j,l \leq k. \tag{2.23}$$

For three points $x_{i_1}, x_{i_2}, x_{i_3} \in I$, the simplex's area A is:

$$A = \frac{1}{2}\|x_{i_1} - x_{i_3}\| \cdot \|x_{i_2} - x_{i_3}\| \sin(\Theta), \tag{2.24}$$

where Θ is the angle between $x_{i_1} - x_{i_3}$ and $x_{i_2} - x_{i_3}$. In regions of high curvature, $\sin(\Theta)$ and A are maximized, reflecting deviation from linearity. At transitions between conic sections, pairwise distances $\|x_{i_j} - x_{i_k}\|$ are largest due to tangent discontinuities.

Thus, the largest simplices in $K_\varepsilon(S)$ form at regions of high curvature or geometric transitions, capturing the key structural features of M. □

Theorem 2.1. *A set of at least six unique middle vertices for largest triangle simplices in the Vietoris-Rips complex can be found from a set of at least six points on an ellipse if any three consecutive points do not lie on a straight line (i.e., points are sufficiently distributed). This set of unique middle vertices necessarily contains at least one ordered sequence corresponding to a non-degenerate set which subtends at least 180 degrees, and can resolve the ellipse.*

Proof: Let $E \subset \mathbb{R}^2$ denote an ellipse defined by:

$$\frac{(x - x_c)^2}{a^2} + \frac{(y - y_c)^2}{b^2} = 1, \tag{2.25}$$

and let $I = \{x_1, x_2, \ldots, x_n\} \subset E$ be a set of $n \geq 6$ points sampled from E, such that no three consecutive points are collinear. For a threshold $\varepsilon > 0$, the Vietoris-Rips complex $K_\varepsilon(S)$ includes all triangles $\{x_j, x_j, x_k\}$ where:

$$\|x_j - x_j\|, \|x_j - x_k\|, \|x_k - x_j\| \leq \varepsilon. \tag{2.26}$$

The largest triangles in $K_\varepsilon(S)$ maximize the area:

$$A = \frac{1}{2}\|x_j - x_k\|\|x_j - x_k\|\sin(\Theta), \tag{2.27}$$

where Θ is the angle between $x_j - x_k$ and $x_j - x_k$. Since I is sampled from an ellipse and the points are sufficiently distributed, such triangles necessarily exist and span significant portions of the ellipse. The "middle vertex" of each triangle is the vertex opposite the largest edge. For $n \geq 6$, at least six unique middle vertices can be identified due to the geometric diversity of I.

To resolve the ellipse, at least five non-degenerate points are required to uniquely determine the parameters (x_c, y_c, a, b). A set of six points ensures that at least one subset of five points spans an arc subtending at least 180 degrees, avoiding degeneracy. Thus, the set I contains a sequence sufficient to resolve the ellipse, with the Vietoris-Rips filtration identifying these points through its largest simplices. □

A table relating the symbols utilized in the mathematical development to neuromechanical states is provided in Table 2.1.

Modeling Effort

Next, the neuromuscular state of volitional (i.e., intentional) effort, $E(t)$, is considered. Effort carries both spatial and temporal characteristics and constraints that can only be accurately discerned from neuromuscular fatigue with higher-order time-frequency terms [95]. The root mean square of the sEMG instantaneous power spectrum, a spatial descriptor of a temporal distribution, is a well documented metric of muscle effort [39, 94]:

$$\hat{E}(t) \approx \sqrt{\frac{\sum_{i=1}^{t} V(i)^2}{t}} \tag{2.28}$$

Effort is related to finger mechanical impedance via the intent state; effort is akin to a scalar quantity applied over the intent or hand kinematic configuration space to achieve torque vectors. The NM3F activation coefficient, H, remains locally time- and globally time-frequency invariant

Table 2.1: Symbol definitions and their neuromechanical interpretations.

Symbol	Description
I_1	Configuration space of the system (e.g., full mechanical impedance space of all hand joints); $\dim(I_1) = \kappa$
κ	Dimensionality of I_1, corresponding to total neuromechanical degrees of freedom
V	Control space, (i.e., surface EMG signals used to drive the system); $V \subseteq \mathbb{R}^n$
$v(t)$	Control signal at time t, e.g., n-dimensional sEMG input vector
n	Number of measured sEMG channels (muscles)
I_2	Set of b target configurations (e.g., known hand poses); $I_2 \subseteq I_1$
b	Number of target configurations or attractors (e.g., labeled hand poses)
f	Nonlinear surjective mapping of control to configuration space, $f : V \to I_1$
$\eta(t)$	Bounded noise perturbing the control-to-configuration mapping
A_j	Attractor in control space associated with target configuration $I_2^j \in I_2$
Θ_j	Mean-reversion rate in the Ornstein-Uhlenbeck process for attractor A_j
σ_j	Noise amplitude in the Ornstein-Uhlenbeck process for attractor A_j
r	Radius of convergence to attractor A_j, defining when $v(t)$ yields $I_1(t) \approx I_2^j$
M_j	Control manifold in V corresponding to configuration $I_2^j \in I_2$
ξ	Upper bound on feasible signal change: $\|v(t+1) - v(t)\| \leq \xi$
T	Short-term prediction horizon (window for minimizing mean squared error)
H	Long-term prediction horizon (window for penalizing divergence or instability)
$I_1(t)$	True system configuration at time t
$I_1^{\text{pred}}(t)$	Predicted system configuration at time t
$\mathscr{E}(T)$	Mean squared error over prediction horizon T
$\mathscr{H}(H)$	Mean squared penalty for prediction divergence over horizon H
$\mathscr{L}(K, \Theta)$	Total loss function combining $\mathscr{E}(T)$ and $\mathscr{H}(H)$ using persistence-weighted kernel
K	Persistence-weighted Gaussian kernel (PWGK) applied to geometric features
Θ	Kernel parameters
$C = \{(x_j, \omega_j)\}$	Set of weighted geometric centroids extracted from local manifold structures
$w(a,b)$ or $\omega(a,b)$	Persistence-like weight for an ellipse with semi-axes a, b: $\omega = \sqrt{a^2 + b^2}$
K_ε	Vietoris-Rips complex at filtration threshold ε
M	Minimum subset of sampled points to resolve a conic manifold
D	Degenerate subset of M that fails to resolve the manifoldf

(temporal constraint), and agnostic of fixed spatial signal composites (spatial constraint). These temporal and spatial constraints result in a clustering interpretation whereby H absorbs unaccounted scaling (i.e. normalized cluster weights) between spatial and temporal clusters [100]. This scaling is readily interpreted as neuromuscular effort for the case of sEMG, yielding an effort

vector that retains the amplitude of activation at discrete points in time denoted in (2.29). The $(\cdot)^{-1}$ terms denote the Moore-Penrose matrix inverse, and $|nS|$ and $|nT|$ represent the number of spatial and temporal synergies respectively. The linear proportionality described on the second line of 2.29 is realized by comparing five millisecond epochs of activation coefficient with effort estimates from raw sEMG, per (2.28).

$$\begin{aligned} ||H|| &\approx W_T^{-1} V W_S^{-1} \\ &= \frac{1}{|nS|^{\frac{1}{2}}|nT|^{\frac{1}{2}}} \sum_{i \in nS} \sum_{j \in nT} V_{ij} \propto \hat{E}(t) \end{aligned} \tag{2.29}$$

Modeling Fatigue

Finally, the neuromuscular state of fatigue, $F(t)$, is considered. The power spectral density of sEMG data with respect to muscle activation frequency, w, is computationally expensive to obtain but readily provides muscle mean instantaneous activation frequency, a well-established metric of fatigue:

$$\hat{F}(t) = \frac{\sum_{i=0}^{\infty} S_V(\omega) \cdot \omega_i}{\sum_{i=0}^{\infty} S_V(\omega)} \tag{2.30}$$

The Wiener-Khinchin (autocorrelation) theorem provides that the power spectral density (PSD) of a stationary random variable is a non-negative real value equivalent to the Fourier transform of the sEMG autocorrelation function, R_{V_T} (k below denotes the sample space for the discrete-time case).

$$S_V(\omega) = \frac{1}{2\pi} \sum_{k=-\infty}^{\infty} R_{V_T}(k) e^{-i\omega k} \tag{2.31}$$

What remains is to show that W_T on the domain $[0\ 200ms)$ can be used to approximate the autocorrelation function R_{V_T}. Four temporal synergies were extracted, each representing the amplitude of unique phase components in V(τ) [47], such that V(τ) can be approximated by summing scaled (c_i) and phase shifted (t_i) temporal synergy vectors W_T.

$$V(t) \approx \sum_{i=1}^{N} c_i W_{T,i}(t - t_i) \tag{2.32}$$

By time-reversing the convolution of $W_{T,}n_{TS}(\tau)\forall n_{TS} > 0$, the autocorrelation function R_{V_T} can be obtained.

$$\begin{aligned} \hat{R}_{V_T}(l) &= \sum_{i=-\infty}^{+\infty} V_T(i) V_T(i-l) \\ &= \sum_{i=-\infty}^{+\infty} W_{T,1}(i) W_{T,2}(i) W_{T,3}(i) W_{T,4}(i) \end{aligned} \tag{2.33}$$

The mean instaneous frequency of the Fourier transform of R_{V_T} can be estimated as the time varying first order moment (i.e., the first order moment taken over discrete time epochs τ). Since (2.33) is a linear function of only W_T, temporal synergies can be used to estimate fatigue. By aggregating the temporal synergies, as in (2.33), muscle fatigue, which is measured as a nonlinear frequency-domain phenomenon, can then be expressed as a linear model in the time domain, as shown in (2.34).

$$\hat{F}_T = \mathbb{E}[\hat{R}_{V_T}] = \frac{\sum R_{V_T}}{N} \tag{2.34}$$

Modeling Neuromotor Control

Neuromotor control describes the coordination of movement by the central nervous system (CNS) through muscle activation, kinematics and dynamics generation, and sensory feedback. Several prominent system dynamic models describe these processes mathematically, providing a foundation for motor adaptation and control. The Equilibrium Point Hypothesis (EPH) proposes that voluntary movement arises from modulation of an internal equilibrium model of the musculoskeletal system specified by the CNS [36]. In this framework, the CNS sets an internal reference configuration, and the neuromuscular system is commanded to follow the reference to minimize an internal loss function via an intrinsic stiffness property. This paradigm is well aligned with the classical reference governor control scheme, allowing volitional joint torques at a given joint q to

be defined as $\tau_{\text{vol}} = K_{\text{RG}}(q_{\text{EP}} - q)$, Where K_{RG} is the CNS-defined reference governor gain, q_{EP} is the equilibrium position set by the CNS, and q is the actual joint position. Building on EPH, the principle of impedance control describes how the neuromuscular system regulates the reference configuration in response to force interactions by adjusting stiffness [101] in response to load torques, τ_{load} and internal kinematic targets, q_{EP}. This principle naturally connects muscle synergy-based finger mechanical impedance estimation (via intent, effort, and fatigue characterization) as mentioned previously.

The cerebellum plays a central role in feedback-based learning and is often conceptualized as a biological servomechanism that supports the fine-tuning of motor commands through predictive error correction [102]. This aligns with the internal model framework, where the cerebellum implements forward and inverse models to anticipate sensory consequences of motor actions and minimize discrepancies between predicted and actual outcomes [33, 103]. These internal models support motor adaptation and trajectory planning under uncertainty [50, 88], facilitating robust performance even in nonstationary environments. Robotics studies inspired by this principle have demonstrated how adaptive controllers can emulate cerebellar-like adjustments in response to perturbations and user effort dynamics [85, 86].

The force interaction dynamics are defined follows, where $M(q)$ is the inertia matrix, $C(q,\dot{q})$ represents Coriolis and centrifugal forces, $B(q)$ and $K(q)$ represents intrinsic damping and stiffness of joints, and $K_{RG}(q - q_{\text{EP}})$ defines the neuromuscular control torque:

$$M(q)\ddot{q} + C(q,\dot{q})\dot{q} + B(q)\dot{q} + K(q)q = \tau_{\text{vol}} - \tau_{\text{load}} \tag{2.35}$$

Optimal Feedback Control (OFC) extends this concept by assuming the CNS minimizes a cost function to optimize movement execution [27] where Q penalizes deviation from the task goal, and R penalizes excessive motor effort. The CNS is thought to rely on internal forward model to predict movement outcomes and compensate for system delays [33, 104]. The forward model, $\pi_{\text{Cognition}}$, predicts the sensory state associated with trajectory error, which the CNS uses to update the reference configuration. Together, these concepts can be combined into an integrated

neuromotor control model for the hand:

$$\min_{\tau_0,\tau_1,\ldots\tau_k} J = \sum_{t=0}^{T} \left(e_k^T Q e_k + \tau_{\text{vol},k}^T R \tau_k \right)$$

Subject to:

$$\begin{aligned} e_k &= q_{\text{target},k} - q_k \\ q_k &\leftarrow (\text{Eq. 2.35}) \\ \tau_{\text{vol},k} &= K_{\text{RG}}(q_{\text{EP},k} - q_k) \\ q_{\text{EP},k+1} &= \pi_{\text{Cognition}}(t, q_{\text{EP},k}, e_k) \end{aligned} \tag{2.36}$$

Eq. 2.61 models neuromotor control, where discrepancies between predicted and actual sensory feedback drive learning. It remains to clarify $\pi_{\text{Cognition}}$ by explaining the sensory feedback and embedding processes that drive overarching motor planning adaptations.

Modeling Somatosensory Processing

Somatosensory processing encompasses the neural transduction of mechanical stimuli into sensory signals for proprioception, tactile feedback, and motor control. The CNS interprets force, texture, vibration, and proprioception through spatiotemporal coding of mechanical stimuli. Mechanoreceptors serve as the primary transducers of tactile stimuli, converting mechanical deformation of the skin into neural signals that encode essential information such as vibration, pressure, and skin stretch. The somatosensory system comprises four distinct classes of mechanoreceptors, each exhibiting unique response characteristics to frequency and amplitude of tactile input. Johansson et al, 1983 [105] demonstrated through microneurography that Meissner corpuscles (MCs) are tuned to low-frequency vibrations (10–50 Hz), making them crucial for detecting slip and grip adjustments, whereas Pacinian corpuscles (PCs) respond to high-frequency vibrations (200–300 Hz), allowing for fine texture discrimination and tool-mediated sensing. Merkel cells exhibit sustained responses to indentation and edges, playing a central role in static pressure detection, while Ruffini endings respond to lateral skin stretch, supporting proprioceptive feedback [106, 107]. The

mathematical encoding of mechanoreceptor responses can be described as a function of stimulus amplitude A and frequency f, where S_i represents the receptor sensitivity and R_i represents the receptor response for each of the four receptors $i \in [1:4]$, f_i denotes its characteristic frequency, and σ_i determines the bandwidth of frequency tuning:

$$R_i = S_i \cdot A \cdot \exp\left(-\frac{|f - f_i|}{\sigma_i}\right) \tag{2.37}$$

This formulation captures the experimentally observed bandpass filtering behavior of mechanoreceptors, where receptors attenuate signals outside their optimal frequency range exponentially [106].

The spatial integration of mechanoreceptor inputs governs tactile acuity, texture discrimination, and proprioception. Gardner et al., 2013 [48] demonstrated that tactile information is spatially integrated via overlapping receptive fields, where higher mechanoreceptor densities (e.g., fingertips) lead to finer spatial resolution, whereas sparser distributions (e.g., forearm) yield coarser perception. As summarized by Mountcastle et al., 2005 [107], cortical receptive fields in the somatosensory cortex integrate signals from multiple mechanoreceptors to construct an interpretable representation of object shape and surface texture. However, spatial integration is not uniform; it is modulated by lateral inhibition, a mechanism that enhances contrast by suppressing neighboring mechanoreceptor responses. This can be described by a difference-of-Gaussians (DoG) model, which approximates the receptive field structure, where $G_{\text{center}}(x,y)$ represents excitation from mechanoreceptors at the stimulus location, $G_{\text{surround}}(x,y)$ represents inhibition from adjacent mechanoreceptors, and λ is an inhibitory gain parameter:

$$R_{\text{true},i} = G_{\text{center}}(x,y) R_{\text{center},i}(f) - \lambda G_{\text{lateral}}(x,y) R_{\text{lateral},i}(f) \tag{2.38}$$

This formulation, supported by findings from [107], explains why edges and textures feel sharper than uniform pressure distributions—receptive fields enhance contrast by suppressing redundant spatial information.

Weber-Fechner's Law and Stevens' Power Law are foundational psychophysical principles that describe sensory perception. Weber et al., 1996 [108], proposed that the relationship between stimulus intensity S and perceived magnitude P follow a logarithmic law, implying that human perception is more sensitive to relative than absolute changes in input intensity. Stevens et al., 1957 [109] refined this with a power-law formulation, demonstrating that the perceived intensity of tactile stimuli follows an exponentially scaled function of actual stimulus intensity, where k is a scaling factor that maps the computed sum of receptor responses with arbitrary human perception units of felt intensity, and n is an empirically determined exponent that varies across sensory modalities. For tactile perception, $n = 0.6$, indicating that perceptual growth compresses at higher stimulus magnitudes:

$$P_i = k_i(R_{\text{true},i})^n \tag{2.39}$$

This formulation explains that small tactile forces feel disproportionately distinct, while large forces saturate perception.

The somatosensory system is tightly coupled with motor control through short-latency reflex loops, enabling rapid and automatic adjustments to tactile disturbances [23, 36, 110]. Reflexive responses are critical for grip force modulation, posture stabilization, and involuntary withdrawal from noxious stimuli [41, 89, 106]. Macefield et al., 1996 [111] demonstrated that cutaneous afferents can directly modulate spinal motor reflexes, bypassing higher cortical processing to produce fast, context-dependent motor responses [12]. Similarly, Prochazka et al., 2011 [110], formalized reflexive motor control as a gain-modulated feedback loop, where reflex amplitude is dynamically scaled based on task demands [110]. Reflexive responses can be modeled using a proportional gain control system, where the reflex-generated force, F_{reflex} is scaled by a reflex gain factor G_r, A is the input intensity (e.g., skin indentation, vibration, or force), and A_{thresh} is the activation threshold for triggering a reflex: $F_{\text{reflex}} = G_r \cdot (A - A_{\text{thresh}})$. G_r is not constant, it is adjusted based on predictive control mechanisms via reflex modulation. For instance, in grip control, reflex gain increases under uncertainty to prevent slippage [27, 88]. Reflex response is thereby modeled as nonlinear as

follows, where γ represents the reflex nonlinearity exponent:

$$F_{\text{reflex}} = G_r \cdot (A - A_{\text{thresh}})^{\gamma}, \quad \gamma > 1. \tag{2.40}$$

This accounts for graded force adjustments, where small perturbations produce minimal response, while larger disturbances evoke strong corrective forces.

Reflex gain G_r additionally adapts to ongoing motor state. For example, in locomotion, proprioceptive reflexes are modulated differently during stance vs. swing phase [112, 113]. During the weight-bearing stance phase, proprioceptive reflexes are facilitatory, enhancing extensor activity to support body weight [114], stretch reflexes of the ankle plantarflexors (soleus, gastrocnemius) are amplified, for postural stability and propulsion, Golgi tendon organ (GTO) reflexes from the extensors become excitatory during stance, to enhance force production, and muscle spindle feedback from the hip extensors (gluteus maximus, hamstrings) to help stabilize the limb and prevent collapse [115]. Here the reflex gain model is discretized to a fixed set of task primitives, or hand poses: power grasp, lateral pinch, two finger pinch, and three finger pinch. Functional magnetic resonance imaging (fMRI) studies have demonstrated that different hand poses, elicit unique activation patterns in the primary somatosensory cortex, akin to somatosensory “bins", or classes, corresponding to specific hand configurations [70, 116, 117]. Per this formulation, $G_r \in \mathbb{R}^4$.

Ernst et al, 2002 [118] model integration of visual and haptic information statistically, demonstrating that the nervous system assigns greater weight to the more reliable sensory modality. Kording et al., 2004 [88] further formalized this as a Bayesian inference process, where multiple sensory estimates are fused while accounting for their uncertainties. This sensory integration follows a Bayesian weighted averaging model, where the estimated sensory state $\hat{x}$ is given as follows, where x_1 and x_2 represent the sensory inputs (e.g., proprioceptive and haptic signals), w_1 and w_2 are weighting factors assigned based on sensory reliability, and $\hat{x}$ is the final integrated sensory estimate. Then, $\hat{e}_k$ represents the trajectory deviation as interpreted through the perceptual system,

incorporating the nonlinear scaling effects of sensory processing:

$$\hat{e}_k = \frac{\sum_i (w_i P_i)}{\sum_i w_i}, \tag{2.41}$$

The weighting factors w_i are determined by the inverse variance of the noise associated with each modality, ensuring that more reliable inputs (lower noise) contribute more to the final estimate, $w_i = \frac{1}{\sigma_i^2}$, where σ_i^2 represents the variance of the sensory estimate for modality i.

This Bayesian integration mechanism accounts for related mechanisms like Multisensory Reweighting, where the nervous system shifts greater reliance onto proprioceptive feedback when visual feedback is degraded (e.g., in darkness), Sensory Calibration, where haptic and proprioceptive feedback adjust to compensate for changes in body-environment interactions, Motor Adaptation, where the relative weighting of sensory signals dynamically adjusts during learning and skill acquisition, and sensory uncertainty, where the brain filters sensory feedback using internal forward models [119].

Then (2.61) is refined as: $q_{\text{EP},k+1} = \pi_{\text{Cognition}}(q_{\text{EP}}, k, \hat{e}_k)$, and the right hand side of 2.35 becomes $\tau_{\text{vol}} - \tau_{\text{load}} - \tau_{\text{reflex},t}$

Adaptive motor planning encompasses conscious and unconscious motor learning responses to feedback and exposure. Several major psychophysical principles guide modern interpretations of adaptive motor planning. The Guidance Hypothesis emphasizes that reducing external guidance is essential for long-term retention and independent skill acquisition [22]. The Challenge Point Framework highlights the importance of calibrating task difficulty to match the learner's skill level, optimizing engagement and learning outcomes [120]. Dual-Task Interference Theory explores how concurrent cognitive demands affect motor performance, underscoring the value of multitasking scenarios in training environments, such as surgery, where simultaneous task management is critical [121].

Numerical and computational approaches further formalize these principles. ACT-R (Adaptive Control of Thought-Rational) provides a computational framework for modeling symbolic

and subsymbolic cognitive processes during development [34]. It utilizes production rules, declarative memory equations, and activation functions to describe skill acquisition dynamics analytically. Optimal Control Theory frames skill acquisition as a dynamic optimization process, governed by Hamilton-Jacobi-Bellman equations, where learning strategies are adjusted to maximize performance over time [122]. Similarly, Vygotsky's Zone of Proximal Development (ZPD) has been modeled using Markov Decision Processes (MDPs) to represent optimal learning trajectories within the ZPD [123]. Extensions such as the Curriculum MDP (CMDP) and Human-skill Curriculum MDP (H-CMDP) incorporate environmental dynamics and proxies like confidence and accuracy to systematically track and optimize skill development [20].

Hierarchical Bayesian Models capture learning as probabilistic inference, describing how knowledge evolves and integrates new information using Bayesian updates and hierarchical priors [88]. These models offer a statistical perspective on how learners adapt strategies and integrate feedback. Connectionist models, such as multi-layer neural networks, simulate developmental progression through error minimization, providing insights into cognitive adaptation during skill acquisition [124].

To model skill acquisition dynamics, the learner's skill state is defined as: $\mathbf{s}[k] = [s_1, s_2]^T$, where s_1 represents accuracy in achieving target kinematics and s_2 represents precision, or repeatability of movement kinematics. Accuracy and precision are major facets of good performance in dexterous motor tasks [46]. Importantly, this enables a system dynamics interpretation where the skill state acts as a (discrete) second order filter, where T_s is the sampling period. The non-stationary learning policy $\pi_{Cogn.}$ is refined with regard to an 'expert' neuromuscular command (which would drive the musculoskeletal dynamics 2.35 to optimal target kinematics):

$$q_{\mathrm{EP}}[k+1] = \begin{bmatrix} \frac{2-s(2)[k]T_s^2}{1+s(1)[k]T_s} & -\frac{1}{1+s(1)[k]T_s} \\ 1 & 0 \end{bmatrix} q_{\mathrm{EP}}[k] \quad + \begin{bmatrix} \frac{T_s^2}{1+s(1)[k]T_s} \\ 0 \end{bmatrix} q_{\mathrm{EP,expert}}[k] \tag{2.42}$$

Using this interpretation, the update rule is defined, where η is a learning rate, modulated by task difficulty, $\beta|m_k - m_{k-1}|$ accounts for curriculum state transitions that impede neural disengagement and plateau effects, and $N([0\ 0]^T, \sigma_s^2)$ represents gaussian process noise:

$$\mathbf{s}[k+1] = \mathbf{s}_{\mathrm{m}} - (\mathbf{s}_{\mathrm{m}} - \mathbf{s}[k])\, e^{-\eta(1+\beta|m_k - m_{k-1}|)P[k]} \qquad + N\left([0\ 0]^T, \sigma_s^2\right) \tag{2.43}$$

Cognitive load affects skill acquisition, particularly in multi-task scenarios [121] where motor execution competes with cognitive demands. The total cognitive demand is modeled as:

$$C(k) = C_{\mathrm{motor}}(k) + C_{\mathrm{cognitive}}(k). \tag{2.44}$$

When $C(k) > C_{\max}$, the learning rate η is reduced:

$$\eta(k) = \eta_0 \cdot e^{-\gamma(C(k) - C_{\max})}. \tag{2.45}$$

This function captures plateaus arising from cognitive overload.

POMDPs are defined as a tuple $(S, A, O, k, Z, R, \gamma)$, with state S, action A, Observation O, Transition probability $T(s'|s,a)$, Observation probability $Z(o'|s,a)$, Reward function $R(s,a)$, and discount factor $\gamma \in [0,1]$ defining the importance of future rewards. A non-stationary POMDP consolidating neuromotor control, somatosensory processing, and adaptive motor planning models is defined in Table 1.

Table 2.2: Non-stationary POMDP formulation for neuromotor control, somatosensory processing, and adaptive motor planning in NeuroSiGHT.

Component	**Definition**
S (State)	$[q_k, \dot{q}_k, s_k]$
A (Action)	$\tau_{\mathrm{vol},k}$
O (Observation)	$\hat{e}_k$
$T(s'\|s,a)$ (Transition)	(Eq. 2.35) (Eq. 17)
$Z(o\|s',a)$ (Observation Model)	(Eq. 15)
$R(s,a)$ (Reward Function)	$R = -(e_k^T Q e_k \tau_{\mathrm{vol},k}^T R \tau_{\mathrm{vol},k})$
γ (Discount Factor)	(Eq. 22)

Now the theoretical performance of policy optimization for a hand held haptic interface is explained, assuming no gross slip or deformation. The haptic interface doubles as the human kinematic input interface to enhance. The haptic signal has tunable amplitude and frequency and can written as an expansion:

$$h_k = A_k \sum_{j=1,3,5,\ldots}^{\infty} \frac{1}{j} \sin\left(k f_k j + \phi_k\right) \tag{2.46}$$

With (2.43), (2.42), and (2.61), a consolidated process model for neuromotor control, somatosensory processing, and adaptive motor planning under haptic guidance policies is obtained.

Next, a straightforward policy optimization case is formulated for the given POMDP model and express theoretical performance constraints. Following this, an algorithmic wrapper is presented for the consolidated model to be utilized in the case study. A straightforward gradient-based network policy optimization is presented for clarity and brevity. Such an approach seeks to maximize the $R \triangleq -J$ from (2.61). A reward function drives haptic policy behavior:

$$\pi_\theta(A_k, f_k | e_k, s_k) = P(A_k, f_k; \theta_k) \tag{2.47}$$

$$R(e_k, A_k, f_k) = -e_k Q e_k - A_k^2 R_A - f_k^2 R_f \tag{2.48}$$

A loss function drives haptic policy updates:

$$J(\theta) = \mathbb{E}\left[\sum_{t=0}^{T} \gamma^t R(e_k, A_k, f_k)\right] \tag{2.49}$$

A Gaussian policy distribution for amplitude and frequency: $A_k = \mathcal{N}(\mu_{A,\theta}(e_k, s_k), \sigma^2_{A,\theta}$, and $f_k = \mathcal{N}(\mu_{f,\theta}(e_k, s_k), \sigma^2_{f,\theta}$ is assumed. The policy gradient is:

$$\nabla_\theta J(\theta) = \mathbb{E}\left[\sum_{t=0}^{T} \nabla_\theta \log \pi_\theta(A_k, f_k | e_k, s_k) R(e_k, A_k, f_k)\right] \tag{2.50}$$

This is expanded to clarify the role of the network parameters:

$$\nabla_\theta J(\theta) = \mathbb{E}\left[\sum_{t=0}^{T}(\nabla_\theta \log P(A;\theta) + \nabla_\theta \log P(f;\theta))R(e,A,f)\right] \tag{2.51}$$

2.2 Development and Implementation of NeuroMERGE

NeuroMERGE - Neuromuscular Model-free Epistemic Risk Guided Exploration - aims to establish safe autonomy in human-robot interactions. It establishes constraints adaptive on safety and efficiency objectives for reinforcement learning (RL) hand exoskeleton control using simultaneous autoepistemic and neuromuscular feedback to modulate exploration by an augmented policy gradient agent. The hand has over 27 degrees of freedom (DoFs) [17], each with unique nonlinear musculotendinous properties. Developers of hand assistive robots typically neglect the six DoFs associated with whole arm and wrist movement (gray joints in Fig 2.6) and assume that the twelve abduction/adduction DoFs of the biaxial joints (red joints in Fig 2.6) have sufficient passive stiffness to support hand poses without assistance. Each finger ($n = 1,...,5$) can be described as a chain of three hinge joints representing flexion/extension of the distal (x_D), proximal (x_P), and metacarpal (x_M) finger joints ($X \triangleq [[x_{D,1}\ x_{P,1}\ x_{M,1}]^T ... [x_{D,5}\ x_{P,5}\ x_{M,5}]^T]$). The biomechanical torque at each joint of the wearer's hand τ_{hand} can be described as the sum of conserved intrinsic dynamics and non-conserved (i.e., volitional) joint torques [40]. Other dynamic parameters associated with this hand model include inertial M, coriolis C, and gravitational parameters G.

$$\tau_{hand} = M(X)\ddot{X} + C(X)\dot{X} + G(X) + \tau_{vol.} \tag{2.52}$$

Previously, non-negative matrix tri-factorization (NM3F) [95] is extended to obtain a measurement model for τ_{hand} and X from surface electromyography (sEMG) signals V_n, which precede finger movement by up to 200 ms [28]. This can be restated as a probabilistic NM3F-based filter utilized to remove temporally (W_T) and spatially (W_S) non-stationary muscle activation patterns from V_n (2.4) to extract A, a stationary space of locally Markov processes or 'Markov blanket',

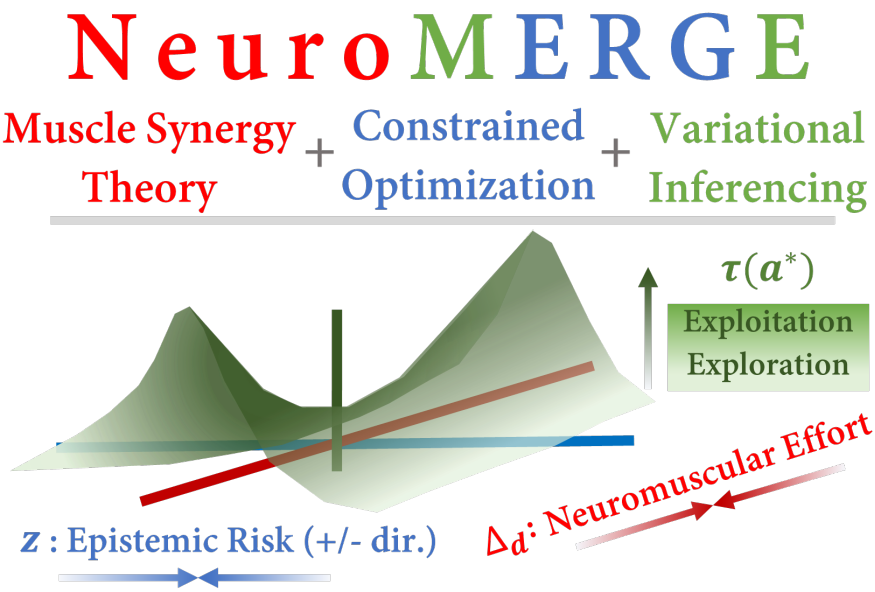

Figure 2.5: This thesis introduces Neuromuscular Model-free Epistemic Risk-Guided Exploration (NeuroMERGE), a RL architecture which bounds exploration with a multivariate non-convex boundary. Arrows represent training start to end.

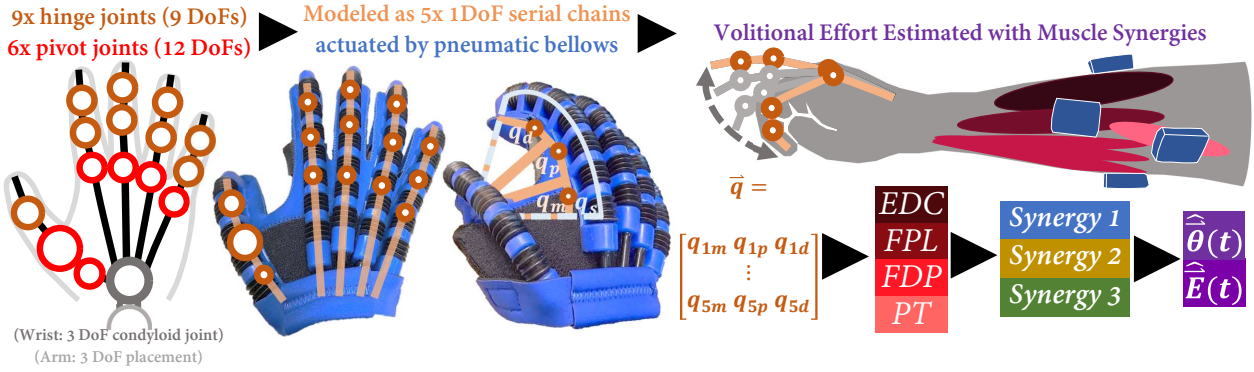

Figure 2.6: From left to right, a schematic-level hand neuromuscular model is presented, which is utilized to reduce the 27 degree of freedom (DoF) workspace of the hand to five flexion/extension DoFs. one nominal DoF, ($\hat{E}$) for the single finger flexion/extension experiment is considered and presented in this thesis.

which summarizes globally non-stationary [125] neuromuscular activation underlying $\tau_{hand}(t)$ [1]. By this, an estimate of $\tau_{hand}(t)$ scored against the running estimate of the max voluntary dynamics ($\hat{\tau}_{hand,max}(t-1) \leftarrow max(\hat{\tau}_{hand,max}(t), \hat{\tau}_{hand}(t))$) is obtained.

Modeling Soft Robotic Mechanics

A series elastic actuator energy conservation model [126] is adapted to represent the hand-mounted soft robot torques τ_{robot}. The model incorporates parameterized functions of pneumatic bellow actuator pressure P (i.e., control variable), volume V, strain energy density f_F, size f_r, differential thickness f_D (owing to the saw-tooth configuration of the bellow surface), and silicone rubber flexural rigidity ($EI\theta^2/2$), with parameters of wall thickness b_1, internal radius b_2, and thickness differential ϕ. See [126] for more specific definition of these terms and their bounds.

$$\tau_{robot} = \frac{P\Delta V}{q_s} - \int_0^a \int_0^{2\pi} \begin{bmatrix} f_F(f_r(b_1) \\ + f_D(b_2, \phi)) \end{bmatrix} d\phi d\tau - \frac{EIq_s^2}{2} \tag{2.53}$$

To model the role of RL in the FEP optimization problem, the free energy principle (FEP) is extended in (2.54 per Kawahara et al., 2022 [127] to online policy gradient agents. The update of initially small policy network parameters θ^* are represented as the maximization of the sum of the Kullback-Leiblier divergence D_{KL} of prior and posterior policy network distributions, $q(\theta)$ and $q(\theta_t|s_{t+1})$, the imitation of the prior ($\mathbb{E}_\pi$) of the policy π, and a cumulative reward (loss) function r for actions a in the state space s on $t = [0 \quad T]$.

$$\theta^* = \arg\max_{\theta} \mathbb{E}_\pi \begin{bmatrix} \sum_{\mathrm{T}=t}^{T} [\gamma^{T-t} [\eta D_{KL}[q(\theta_{\mathrm{T}}|s_{\mathrm{T}+1})|q(\theta_{\mathrm{T}})] \\ + \beta\, \mathbb{E}_\pi[\log p(a_t|s_t)] + r(s_{\mathrm{T}}, a_{\mathrm{T}})]] \end{bmatrix} \tag{2.54}$$

$$EQUATION : [\theta] \rightarrow a_t \tag{2.55}$$

$$EQUATION : a_t \rightarrow P(t) \tag{2.56}$$

The net torque τ at the hand is $\tau = \tau_{hand} - \tau_{robot}$. To enable the wearer to move freely without experiencing physical impediment to movement, τ_{hand} should be compensated by τ_{robot}, so that the biomechanics are canceled by the robot mechanics (expressed as the objective *maximize* : $r = -|\tau|$).

Remark 1: (Safety and Efficiency are Encoded in the Multi-Objective Policy Optimization Model) The solution space of the FEP framework represents the maximization of both exploration ($\eta D_{KL}[\cdot]$) and exploitation ($\beta \mathbb{E}_{pi}[\cdot]$). From this formulation, it is natural that the hyperparameters η and β be considered for the cause of modulating the exploration-exploitation tradeoff toward safety, however ensuring safety and near-optimal policy convergence using static a-priori gains η and β to govern the tradeoff has been explored and determined to be an NP-hard problem [128]. The static formulation is useful in describing the any-time estimate of the optimal solution space but lacks sufficient depth to dynamically constrain the space according to safety requirements. Dynamically constrained RL has been proposed to address this challenge but has not been thoroughly investigated in HRI.

Remark 2. (There Exist Safe And Unsafe (Risky) Sets In The HRI State Space) Let $\max(\bar{\mathrm{T}}_{robot}) = \max(\bar{\mathrm{T}}_{hand})$ and $\min(\bar{\mathrm{T}}_{robot}) = \min(\bar{\mathrm{T}}_{hand}) = 0$. From (2.52) and (2.53) it is evident that the robot can generate torques that overpower the wearer at sub-maximal volitional effort, impeding movement, straining the neuromuscular system, and causing significant neuromuscular fatigue [1, 6, 125]. From (2.54), it can be seen that any sub-optimal policy will result in impedance to movement (i.e., $r(s_{\mathrm{T}}, a_{\mathrm{T}}) < 0$), and that sub-optimal policies are favored while the state-space is unexplored (i.e., while $\beta \mathbb{E}_{\pi}[\cdot] \leq \eta D_{KL}[\cdot]$) A variable safe subset of the robot action space which does not overcome user volitional torque can be defined: $|\bar{\tau}_{robot,safe}(t)| \triangleq f(\bar{\tau}_{hand}(t)) \leq \max(|\bar{\tau}_{robot}|)$. The exploration can be considered risky if $\tau_{robot}(t)$ exceeds the safe set: $[-\tau_{robot,safe}(t) \quad \tau_{robot,safe}(t)]$. Toward a proof of concept, this thesis considers assistance for unimpaired adults and define the safe set as $[-\tau_{hand}(t) \quad \tau_{hand}(t)]$.

Inclusion of feedback of wearer effort and agent autoepistemic risk in on-line on-policy model-free policy optimization is proposed. There is much open-source support and documentation for policy gradient (PG) methods, which are well-suited for on-policy model-free robot control [129]. PG is incorporated in an approximate dynamic programming scheme (PG-ADP) to realize the proposed approach.

The typical PG-ADP update rule consists of updating the policy π via the gradient of the action value function Q:

$$\begin{aligned} Q_i &\triangleq r_i + \gamma Q(s_{t+1}, \pi(s_{t+1}) \\ \pi_{i+1} &= \pi_i - \alpha \nabla_a Q_i(a,s)|_{s,a_i} \end{aligned} \tag{2.57}$$

The Q-function term of this update rule is the natural target for adaptive penalties derived from the epistemic logical model (2.54) driven by safety and efficiency considerations [128]. A update penalty, $B \triangleq f(\Delta_d(t), z(t))$, was developed which varies with an estimate of autoepistemic loss describing the divergence between successive policies $z(t)$, and which relaxes with neuromuscular effort $\Delta_d(t) = -\tau_{hand}(t)$. The autoepistiemic loss z quantifies the amount by which previous diverges from the current estimated optimal policy, $z = D_{KL}[q(\theta_{\mathrm{T}}|s_{\mathrm{T}+1})|q(\theta_{\mathrm{T}})]$, and Δ_d signifies the size of the safe set. Both are non-negative.

$$B(\Delta_d(t), z(t)) \triangleq \begin{cases} 1 & \text{if } z^2 < \Delta_d^2 - 1 \\ (\Delta_d^2 - z^2) & \text{if } \Delta_d^2 - 1 \leq z^2 \leq \Delta_d^2 \\ 0.01 & \text{if } z^2 > \Delta_d^2 \end{cases} \tag{2.58}$$

This definition of B is motivated by traditional control barrier functions for nonlinear effort-aware HRI control [130] with epistemic - instead of physical - state estimates. The penalty is implemented as a gain on Q alongside the discount factor in the gradient term in the PG-ADP scheme: $\pi_{i+1} = \pi_i - \alpha B \nabla_a \cdot Q_i(s,a)|_{s,a_i}$.

Proof 1. (Convergence Toward Optimality): Per the policy gradient theorem, for any $0 < B(t) < 1$, assume $0 \leq Q(s_t, a_t) \leq R(s_t, a_t) + \gamma_1 Q(s_{t+1}, \pi(s_{t+1}))$, and that the optimal policy π^* is

obtained at Q_∞:

$$\lim_{i\to\infty} Q_i(s_{t+1},a_{t+1}) = R(s_t,a_t) + \gamma Q_i(x_{t+1},\pi_i^*(s_{t+1})] \tag{2.59}$$

Nondecreasing gradient ascent (i.e., progression towards near-optimality) is established per [131]. First a new Q-function, $\Phi_{j+1}(s_t,a_t) = R(s_t,a_t) + \gamma\Phi(x_{t+1},\pi(s_{t+1}))$ is defined, and assume that $\underline{Q}$ is generated by $R(s_t,a_t) + \gamma\underline{Q}(x_{t+1},\pi(s_{t+1})$ with $\underline{Q} = 0$. Then, for all j, the action value function sequence Φ is nondecreasing and will converge to $\underline{Q}$ as $i \to \infty$. The iterative Q-function process $P_i(x_t,a) = R(s_t,a_t) + \gamma P_{i-1}(x_{t+1},\pi(s_{t+1})]$ is defined. By induction, with $P_i = Q_\infty$, then for $i = \infty$, then $P_\infty = Q_\infty$ so that $\pi = \pi^*$. Thus, the iterative policy gradient method converges to the optimal policy as training progresses.

Proof 2. (The Penalty Function B Dictates Divergence from the Any-Time Estimated Optimal Policy (i.e., Divergence from the Safe Set): Let $\mathcal{A} = \alpha B$. In the modified PG-ADP scheme, $\mathcal{A}$ acts as a regularizer, diminishing the variance of policy gradient ascent trajectories, the mean of which rises from the null policy to the optimal policy along the safe set following the reward dynamics ($r := -\tau$) [132]. To prove this, it is shown how the deviation between any-time estimated optimal and successively updated stationary gaussian policies, $\pi(a|s,\theta) \approx \mathcal{N}(\theta^T\phi(s),\sigma^2)$ (with mean defined as the linear combination between state features ϕ and θ) are related to $\mathcal{A}$ [133]. By policy gradient theorem, the difference between successive updated policies can be bounded:

$$\begin{aligned} &\pi(a|s,\theta_{i+1}) - \pi(a|s,\theta_i) \geq \\ &\mathcal{A}\nabla_\theta\pi(a|s,\theta)^T\nabla_\theta Q(\theta) - \frac{\mathcal{A}}{\sqrt{2\text{ß}\sigma^3}}(|\nabla_\theta Q(\theta)|^T|\phi(s)|)^2 \end{aligned} \tag{2.60}$$

Then, per [133], Pinsker's inequality is utiized to upper-bound the Kullback-Liebler measure of the divergence between the policies, so that supremum norm between policies can be upper-bounded as $||\pi_{\theta_{i+1}} - \pi_{\theta_i}||_\infty \leq \frac{\mathcal{A}M}{\sigma}||\nabla_\theta Q(\theta)||_1$, where the M upper bounds ϕ per $\phi_i(s) < M \; \forall \; s \in S, i \to \infty$. From this relation, the upper-bound on updates varies directly with B, such that B drives the policy update dynamics.

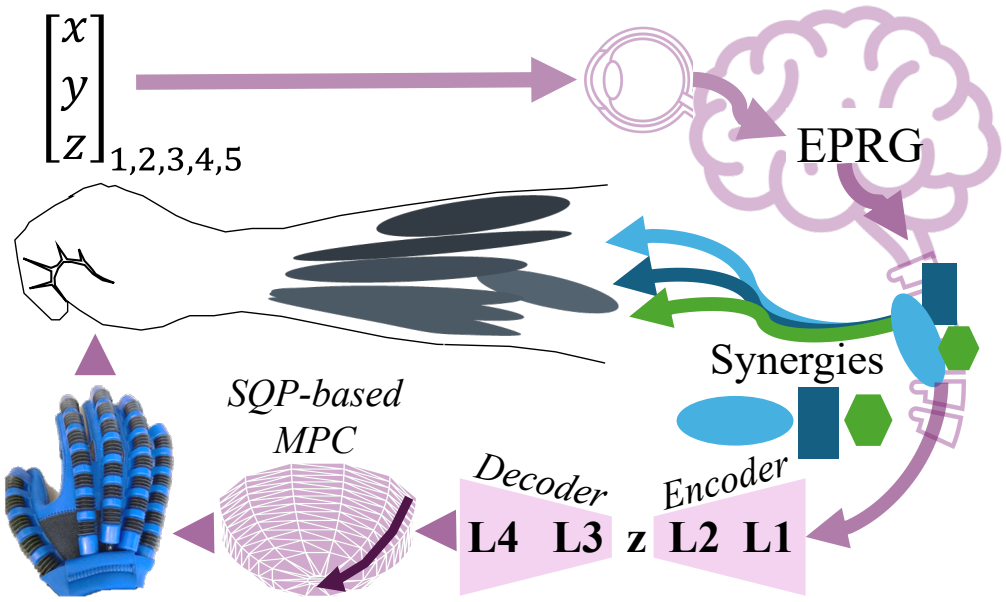

Figure 2.7: NeuroGAIN-MPC, Neuromechanical Generative Autoencoding Impedance Network with Model-Predictive Control, is presented for an assistive soft hand exoskeleton to reduce wearer effort and fatigue. NeuroGAIN uses an autoencoder-based generative neuromechanical model to treat the wearer as a position-based equilibrium point reference governor (EPRG)and forecast EPRG effort and intent from muscle synergies extracted from surface electromyography (sEMG) signals.

2.3 Development and Implementation of NeuroGAIN

NeuroGAIN - Neuromechanical Generative Auto-encoding Impedance Networks - was developed to learn hidden features and state transition dynamics online, reducing modeling overhead and enhancing adaptability to stochastic effects like muscle fatigue [134]. This approach builds on NM3F to collapse muscle activation signals into low-dimensional muscle synergies from sEMG data, reducing input dimensionality for data-efficient prediction. Offline capability of NeuroGAIN to accurately forecast neuromuscular effort associated with complete hand poses using as little as five ms of sEMG time series data at the start of pose.

A model of hand neuromechanical control was constructed from $\hat{I}$, $\hat{E}$, and $\hat{F}$ using EPH [42]. EPH is a neuromechanical paradigm explaining voluntary movement control as joint reference positions sent to muscle synergy-based motor controllers at the central nervous system (CNS) whereby the CNS acts as a reference governor [37]. Under this EPH-based reference governor (EPRG) scheme, isometric hand grasp force regulation is considered a joint torque control process

with joint position feedback [135]. Skin was assumed infinitely stiff, then the state of the arm can be represented as: $\mathbf{x}_{arm} = [\theta_{arm}^T \quad \dot{\theta}_{arm}^T]^T$ lawhere θ_{arm} is the vector of shoulder, elbow, and wrist joint angles. Then $\tau_{active} := \mathbf{K_{EPRG}}$ are volitional joint torques, κ is a linear function of the state, $r(t)$ is the experience-based neuromuscular reference to achieve the kinematic (target) constraint $y \in \mathscr{Y}$, and $v(t)$ is the reference trajectory produced by EPRG to satisfy $y \in \mathscr{Y}$ when object manipulation is introduced. The system evolution constraint $x \in \mathscr{X}$ varies with physical capabilities of muscles, tendons, and joints. A pre-trained data-based linear fatigue model $\hat{F}(t) = \mathscr{M}(\hat{E}(t))$ and $\mathscr{X}(t,\hat{F})$ are utilized from prior work [1]. T is the subsequent time step.

$$
\begin{aligned}
\tau_{active} =& \hat{I} \times \hat{E} = \mathbf{K_{EPRG}}(x) = \kappa(v(t), x(t)) \\
v(t) =& \underset{v \in \mathscr{R}(r(t),x(t))}{\arg\min} \; ||v(t) - r(t))|| \\
&\text{Subject to:} \qquad \hat{F} \leftarrow \mathscr{M}(\hat{E}(t)) \\
& x(t+T) \in \mathscr{X}(t,\hat{F}) \; \forall \; T \geq 0 \\
& \mathbf{K_{EPRG}}(t+T) \in \mathscr{K}_{EPRG} \; \forall \; T \geq 0 \\
& y(t+T) \in \mathscr{Y}(t) \; \forall \; T \geq 0 \\
& \mathscr{X}(t) = \left\{ x \;|\; \begin{array}{l} \theta_{\min} \leq \grave{}(t) \leq \theta_{\max} \\ \dot{\theta}_{\min} \leq \dot{\theta}(t) \leq \dot{\theta}_{\max} \end{array} \right\} \\
& \mathscr{K}_{EPRG} = \{0 \leq K_{EPRG} \leq 2\} \\
& \mathscr{Y} \leftarrow \text{Target Kinematics}
\end{aligned}
\tag{2.61}
$$

The set $\mathscr{X}(t)$ constrains joint motion with muscle fatigue, ensuring that EPRG solutions remain feasible. This definition encapsulates the limitations imposed by the neuromechanical model and the physical properties of the musculoskeletal system.

NeuroGAIN employs an LSTM-VAE framework (Fig. 2.8) to learn dependencies and predict synergy activation sequences. LSTM nodes model hidden temporal dynamics including muscle

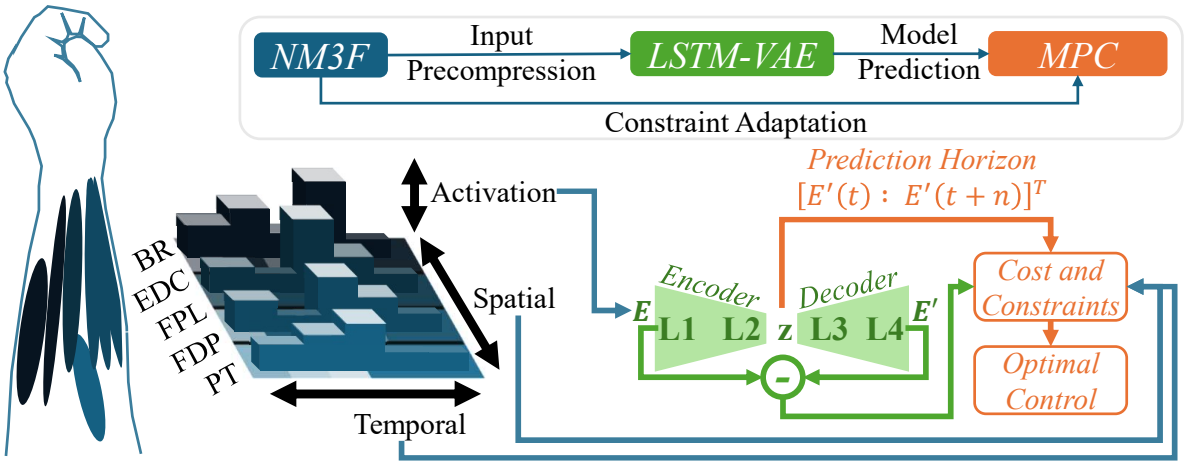

Figure 2.8: This thesis implements NeuroGAIN [3] as the modeling stage in MPC. NeuroGAIN uses an LSTM-VAE network to forecast effort from muscle synergies for exoskeleton MPC. Constraints include intended hand pose from spatial synergies, and fatigue from temporal synergies.

fatigue [136] using input, forget, and output gates that are sensitive to temporal features. LSTM-processed data passes through the VAE, where an encoder compresses the data into a latent space, mapping the LSTM outputs to a latent set [137, 138].

The LSTM-VAE produces hidden state $h(t)$ to compute parameters of the latent distribution. The latent variable z models the spatial s of the input [139] and is sampled using the reparameterization trick by the decoder to reconstruct $\hat{E}$ using $\hat{h}$ and $\hat{\hat{E}}$. Gradient of the sum of the reconstruction loss and the Kullback-Leibler (KL) Divergence is used to update parameters for the LSTM and VAE networks [140]: $\frac{\partial \mathscr{L}}{\partial W_n} = \sum_i \frac{\partial \mathscr{L}}{\partial n_t} \cdot x_t^T$.

2.4 Algorithmic Implementations

Next, algorithmic summaries of the data-driven approaches developed in this chapter are provided.

Algorithm 1 Dynamic Ergodic Decomposition for Attractor Identification

Require: sEMG data stream $\{x_t\}_{t=1}^{T}$, window size n, merge threshold τ
Ensure: Dynamic attractor regions $\{X_\alpha\}$ and centroids $\{c_\alpha\}$

Initialize $\mathscr{X} \leftarrow \emptyset$, $\{X_\alpha\} \leftarrow \emptyset$, $\{c_\alpha\} \leftarrow \emptyset$
for each time step $t = 1$ to T **do**
    Append x_t to buffer $\mathscr{X}$
    if $|\mathscr{X}| > n$ **then**
        Remove the oldest point from $\mathscr{X}$
    end if
    Compute centroid $c_t \leftarrow \frac{1}{|\mathscr{X}|}\sum_{x\in\mathscr{X}} x$
    Initialize new attractor candidate $X_t \leftarrow \mathscr{X}$
    merged $\leftarrow$ **false**
    for each $X_\alpha \in \{X_\alpha\}$ with centroid c_α **do**
        Compute distance $d \leftarrow \|c_t - c_\alpha\|$
        if $d \leq \tau$ **then**
            Merge: $X_\alpha \leftarrow X_\alpha \cup X_t$
            Update centroid:

$$c_\alpha \leftarrow \frac{n_\alpha c_\alpha + n_t c_t}{n_\alpha + n_t}$$

            merged $\leftarrow$ **true**
            break
        end if
    end for
    if not *merged* **then**
        Add new attractor: append X_t to $\{X_\alpha\}$ and c_t to $\{c_\alpha\}$
    end if
end for

Then an update rule for network parameters is defined as $\theta_{k+1} = \theta_k + \eta\nabla_\theta J(\theta)$.

Algorithm 2 NeuroSiGHT Policy Optimization

Initialize parameters θ_0, prior neuromechanical model $\mathscr{M}$, hand-wrist OpenSim model $\mathscr{H}$, task goal q^*, learning rate η, exploration decay γ
Load OpenSim hand-wrist model $\mathscr{H}$ and prior neuromechanical model $\mathscr{M}$
Set $\pi_{\theta_0}(A_0, f_0|e_0, s_0)$ using pre-trained priors from $\mathscr{M}$
Define Gaussian policy priors $A_k = \mathscr{N}(\mu_{A,\theta}, \sigma^2_{A,\theta})$, $f_k = \mathscr{N}(\mu_{f,\theta}, \sigma^2_{f,\theta})$
for each trial $k = 1$ to T **do**
    Compute Sensory Prediction Error: $\hat{e}_k = \frac{\sum_i (w_i P_i)}{\sum_i w_i}$
    Update Equilibrium Point: $q_{\text{EP},k+1} = \pi_{\text{Cognition}}(q_{\text{EP}}, k, \hat{e}_k)$
    Compute Haptic Feedback Action: $(A_k, f_k) \sim \pi_\theta(A_k, f_k|e_k, s_k)$
    Apply Haptic Feedback: $h_k = A_k \sum_{k=1,3,5,\ldots}^{\infty} \frac{1}{i}\sin(t f_k i + \phi_k)$
    Update Skill State: $\mathbf{s}[k+1] = \mathbf{s}_\text{m} - (\mathbf{s}_\text{m} - \mathbf{s}[k])e^{-\eta(1+\beta|m_k - m_{k-1}|)P[k]} + N([0,0]^T, \sigma_s^2)$
    Compute Policy Gradient: $\nabla_\theta J(\theta) = \mathbb{E}\left[\sum_{t=0}^{T} \nabla_\theta \log \pi_\theta(A_k, f_k|e_k, s_k) R(e_k, A_k, f_k)\right]$
    Update Policy Parameters: $\theta_{k+1} = \theta_k + \eta\nabla_\theta J(\theta)$
    Reduce Exploration Over Time: $\eta \leftarrow \eta \cdot e^{-\gamma k}$
end for
return Optimized policy π_θ

The PG-ADP scheme with penalization was implemented using MATLAB [141].

Algorithm 3 NeuroMERGE Implementation

Initialize policy parameterization π with small network weights θ
Initialize $\Delta_d = 0.01$
for Each Episode **do**
    Initialize Q_T
    for $t = 1$ to T_{episode} **do**
        $\tau_{robot}(t) = \pi(s_{t-1}, a_{t-1}, r_t, s_t|\theta)$
        Execute τ_{robot} in the HRI state space
        for $t = t$ to $t = t + 5$ ms (Markov Blanket) **do**
            Measure and Extract $V_n(t) = W_T A_n W_S$
            Estimate $\hat{\tau}_{hand}(t) \approx A / \hat{\tau}_{mvc}$
            Update Observation $s_{t+1} = \hat{\tau}_{hand}(t)$
        end for
        Record s_{t+1}, r_{t+1}
        $\Delta_D \leftarrow \Delta_D + r_t$
        $z \leftarrow D_{KL}[q(w_t)|p(s_{t+1,w_t})]$
        $B = (\Delta_d^2 - z^2)$
        $\pi \leftarrow \pi + \alpha B \sum_{t=1}^{T-1} \nabla_\theta Q_t(s_t|a_t)$
    end for
end for

The LSTM-VAE update rule is defined in Algorithm 1, where E_t is the input sequence at time step t, h_{t-1} is the hidden state from the previous time step, c_t is the cell state, σ is the sigmoid function, $\mathrm{w}_f, \mathrm{w}_i, \mathrm{w}_c, \mathrm{w}_o$ are the weights, and b_f, b_i, b_c, b_o are the biases for the forget, input, cell, and output gate biases respectively, and $\odot$ denotes element-wise multiplication:

Algorithm 4 UPDATE LSTM-VAE

Input: Sequence E
Compute LSTM hidden states:
$$c_t = \sigma(\mathrm{w}_f \cdot [\mathrm{h}_{t-1}, E_t] + \mathrm{b}_f) \odot c_{t-1} +$$
$$\sigma(\mathrm{w}_i \cdot [\mathrm{h}_{t-1}, E_t] + \mathrm{b}_i) \odot \tanh(W_c \cdot [\mathrm{h}_{t-1}, E_t] + \mathrm{b}_c)$$
$$h(t) = \sigma(\mathrm{w}_o \cdot [\mathrm{h}_{t-1}, E_t] + b_o) \odot \tanh(c_t)$$
Compute latent distribution parameters:
$$\mu = \mathrm{w}_\mu \mathrm{h}_T + \mathrm{b}_\mu \quad \log \sigma^2 = \mathrm{w}_\sigma \mathrm{h}_T + \mathrm{b}_\sigma$$
Compute latent variable z:
$$z = \mu + \sigma \odot \varepsilon \quad \text{where} \quad \varepsilon \sim \mathscr{N}(0, I)$$
Decoder initial hidden state: $\mathrm{h}_0 = g(z)$
Reconstruct sequence: $\hat{E}_t = \mathrm{w}_{\hat{E}} \cdot \hat{\mathrm{h}}_t + \mathrm{b}_{\hat{E}}$
Compute loss function:
$$\mathscr{L} = \sum_{t=1}^{T} \|E_t - \hat{E}_t\|^2 + \left(\frac{\beta}{2} \sum_{j=1}^{d} \left(1 + \log(\sigma_j^2) - \mu_j^2 - \sigma_j^2 \right) \right)$$
Update parameters: $\Theta \leftarrow \Theta - \eta \frac{\partial \mathscr{L}}{\partial \Theta}$

Algorithm 5 NeuroGAIN-MPC in VR-HRI

1: ■ **Initialize 'Hidden' Neuromechanical HRI Model**: Using open-source anthropometric datasets, establish the EPRG, exoskeleton, and block parameters
2: ■ ■ **Initialize NeuroGAIN-MPC**:
Set parameters for ***Model***, a NeuroGAIN agent
3: **for** episode in episodes **do**
4: ■ **Use** (3.8) **to Update BBT Task Objective** $\mathscr{Y}$
5: ■ **Use** (2.61) **to obtain** $r(t)$
6: ■ **Calculate Human State**

$$\blacksquare\ \boldsymbol{\phi}_{\mathbf{passive}} = a \cdot e^{bx+f} + c \cdot e^{dx+g} \quad \blacksquare\ \boldsymbol{\phi}_{\mathbf{active}} = \mathbf{K}_{\mathbf{EPRG}}(x, \mathscr{Y})$$

$$\blacksquare\ \boldsymbol{\phi}_{\mathbf{human}}(x, \mathscr{Y}) = \boldsymbol{\phi}_{\mathbf{active}} + \boldsymbol{\phi}_{\mathbf{active}}$$

$$\blacksquare\ \hat{E}(t) \leftarrow \boldsymbol{\phi}_{\mathbf{human}} \times \hat{I}^T(t) \quad \blacksquare\ \hat{E}(t) \leftarrow NM3F(V(t))$$

$$\blacksquare\ \blacksquare\ \hat{F}(t) \leftarrow \mathscr{M}(E(t))$$

7: ■ ■ **Calculate Robot Input with NeuroGAIN-MPC**

$$\blacksquare\ \blacksquare\ \hat{E}(t : t+h) = \text{predict}(\hat{E}(t), \textbf{\textit{Model}})$$

$$\blacksquare\ \blacksquare\ \mathscr{C} = (\hat{E}(t : t+h))^2$$

■ ■ Compute (3.5) then (3.7) to obtain $\boldsymbol{\phi}_{\mathbf{e}}$, τ_{HRI}

8: ■ ■ **Call Algorithm 1 to update *Model***
9: ■ ■ **Forward HRI Environment**

$$\blacksquare\ \theta \approx \int \mathbf{M}^{-1}(\boldsymbol{\phi}_{\mathbf{HRI}} - \boldsymbol{\phi}_{\mathbf{grav}} - \mathbf{D}\dot{} - \mathbf{F}\grave{})$$

■ $\theta \leftarrow$ Haptic Interface Sensors

$$\blacksquare\ \blacksquare\ \mathbf{P}_{\mathbf{bulb}} = [x\ \ y\ \ z]^T = [T_{103}\ \ T_{213}\ \ T_{323}]^T$$

$$\blacksquare\ \tau_{Touch} = K_p(\mathbf{e}) + K_d(\mathbf{e}/dt)$$

10: **end for**

■ MATLAB Simulation ■ Human Participant Experiment

This chapter presented the development and implementation of the members of the computational neuromechanical suite. The next chapter explores experimental validation of each member of the suite.

Chapter 3

Experimental Utility Validation of the Neuromechanical Suite

This chapter presents experimental validation of each member of the computational neuromechanical suite. Studies 1-3 correspond to validation of NeuroSiGHT, study 4-5 corresponded to validation of NeuroMERGE, and study 6 corresponds to validation of NeuroGAIN. First, the design of each study is described in Sections 3.1- 3.6, then the results for each study are presented and contextualized in Section 3.7. All human participant experiments were approved by Auburn University's Institutional Review Board (#22-080 EP 2202). [1]

3.1 Study #1: Linear Supervised Neuromechanical Models

The first study was conducted to evaluate the capacity of NeuroSiGHT to accomplish linear modeling of neuromechanical states. Fifteen healthy adults (thirteen male, two female) aged 20-30 were recruited. Delsys Trigno electrodes were used to collect all sEMG data. An experimental protocol with three unique dynamic conditions, summarized in Fig. 3.1, was executed. In Condition 1, participants were instructed to hold a bulb dynamometer with negligible contractile dynamics [142] using a power grasp for three 60 second trials. They were provided visual feedback to maintain constant sEMG RMS output at 70% of their maximum voluntary contraction (MVC) level (Fig. 3.1, row 1). Intent and effort were thereby fixed (i.e., a single pose was repeated at a fixed effort level) while fatigue level was allowed to vary.In Condition 2, ten of the fifteen participants repeated full-range flexion and extension of the right index metacarpophalangeal joint in one second intervals for one minute (Fig. 3.1, row 2). Resistance which was noticeable without imposing fatigue was established using a soft robotic therapy glove. The glove provided either

[1] Portions of this chapter have been published in ASME Letters in Dynamic Systems and Control [1], and IEEE Journal of Medical Robotics Research [3], and presented at the IEEE American Controls Conference [5].

no resistance or resistance (GLOVE NR and GLOVE R, respectively) by pressurizing a bellows rigidly affixed along the index finger from 0 to 80 kPa. Intent and fatigue were thereby fixed while effort was allowed to vary.

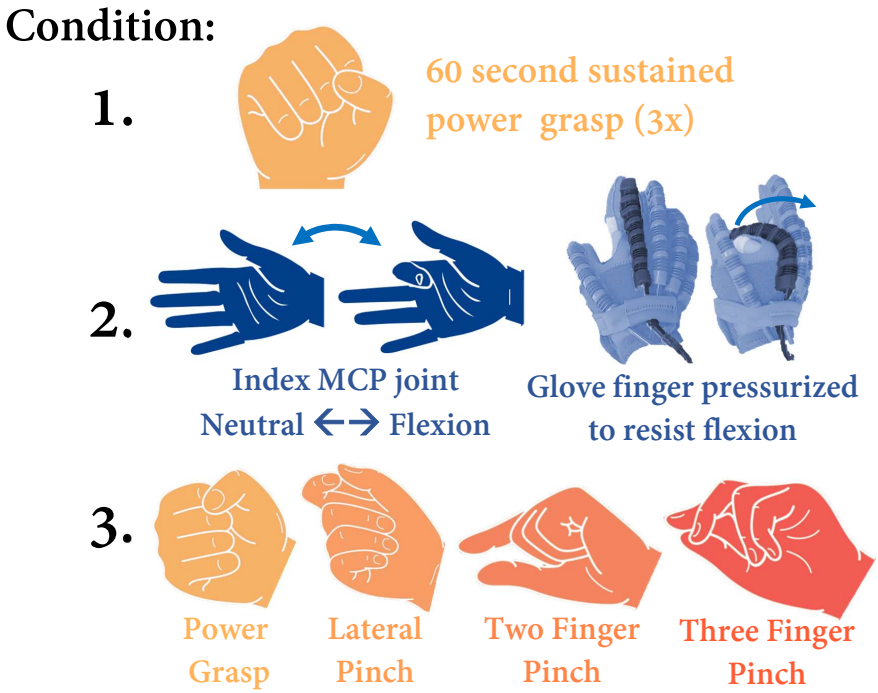

Figure 3.1: Three experimental conditions were utilized to examine the utility of NM3F sEMG factors for linear neuromuscular state estimation.

In Condition 3, the same participants performed quasi-isometric hand poses (shown in orange to red in Fig. 3.1, row 3) at effort levels compatible with everyday activities (e.g., grasping a door knob, pinching a lock and key). PG sEMG RMS level was 50% MVC, so that pose intent was varied while effort and fatigue were fixed, providing a benchmark for comparison between Condition 1 and Condition 3.

Surface electromyography (sEMG) signals were collected using Delsys Trigno electrodes placed on the Flexor Digitorum Profundus (FDP) (Responsible for flexing the fingers at the distal joints in pinching and grasping), Flexor Digitorum Superficialis (FDS) (Controls flexion at the middle joints of the fingers, aiding in dexterous movements), Flexor Pollicis Longus (FPL) (Flexes the thumb, critical for all pinch grips), Extensor Digitorum Communis (EDC) (Extends the fingers and stabilizes the hand during gripping), Pronator Teres (PT) (Pronates the forearm, turning

the hand palm down), Extensor Carpi Radialis Longus (ECRL) (Extends and abducts the wrist.) Electrodes were applied to cleaned skin surfaces.

3.2 Study #2 Topological Unsupervised Model

The second study aims to validate the topological data analysis method for unsupervised manifold recognition for both a simulated 2-DoF pendulum with a switching set-point, as well as for human participant intent detection via sEMG . An inverted pendulum simulation was implemented in MATLAB with second-order underdamped oscillator dynamics governed by a piecewise time-varying equilibrium offset. The configuration space $I_1 \subset \mathbb{R}^2$ represents angular position and velocity in the θ_1 (rotation about the pendulum y axis) and θ_2 (rotation in the pendulum x axis; gravity was in the negative z direction in the global reference frame).

$$i_1(t) = [\theta_1(t), \dot{\theta}_1(t)\dot{\theta}_2(t)]^\top, \tag{3.1}$$

The control space $V \subset \mathbb{R}^1$ corresponds to the applied torque $v(t)$. The dynamics evolve according to the straightforward nonlinear equation:

$$\ddot{\theta}(t) = \frac{v(t)}{J} - \frac{b}{J}\dot{\theta}(t) - \frac{mgL}{J}\sin(\theta(t)), \tag{3.2}$$

but for this demonstration, a linearized underdamped harmonic oscillator subject to a time-varying equilibrium offset $A_i(t)$ was considered:

$$\ddot{x}(t) + 2\zeta\omega\dot{x}(t) + \omega^2\big(x(t) - A_i(t)\big) = 0, \tag{3.3}$$

where $x(t)$ represents angular position deviation from equilibrium, ζ was the damping ratio, ω the natural frequency, and $A_i(t)$ the time-varying attractor in V.

Three attractor transitions are simulated, each active over one-third of the simulation time. These transitions shift the system's equilibrium, leading to distinct regions in the control trajectory

corresponding to piecewise attractor convergence. This emulates the manifold transitions described in Chapter 2:

$$\|v(t) - A_i\| \leq r \Rightarrow s_1(t) \approx s_2^i. \tag{3.4}$$

The control variable $v(t)$ behaves deterministically here but may be interpreted as the mean trajectory of an Ornstein-Uhlenbeck process with low noise. The system was simulated over $t \in [0, 10]$s with $\zeta = 0.01$, $\omega = 2\pi$, and switching attractor values (i.e., set-points for the underdamped pendulum control scheme) $\{1, 3, -0.5\}$ applied at equal time intervals.

The resulting trajectory $s_1(t)$ which contains the position and velocity in the pendulum's θ_1 direction and position in the θ_2 direction to accomplish a 3D, spatially interpretable result, was segmented into overlapping windows, and each segment was analyzed using a persistence-weighted kernel based on geometric primitives derived from the phase portrait. A Vietoris-Rips filtration was applied to identify non-degenerate manifolds and reject geometrically redundant subsequences.

The persistence-like weights ω_i were computed for each elliptical segment, and centroids $x_i \in \mathbb{R}^2$ extracted to build point sets $C = \{(x_i, \omega_i)\}$ used in kernel evaluation.

This simulated system demonstrates the emergence of persistent, bounded manifolds in response to control attractor transitions. Three distinct elliptical manifolds in the $(\theta, \dot{\theta})$ space are observed, each corresponding to an attractor region. The largest simplices from the Vietoris-Rips complex consistently formed at curvature transition points, confirming Proposition 1.

Secondly, the dataset from Study # 1 is utilized to establish unsupervised intent classification through TDA as described in the previous chapter. The goal of was to demonstrate the utility of TDA to uncover local nonlinear phenomena in globally linear neuromechanical states like intent and to use these for accurate and robust tracking.

The goal of the simulation and human participant data analysis in Study #3 was to validate NeuroSiGHT's capabiliy to classify manifolds in OUP-like systems in an unsupervised manner to enable on-line data-driven HRI design approaches.

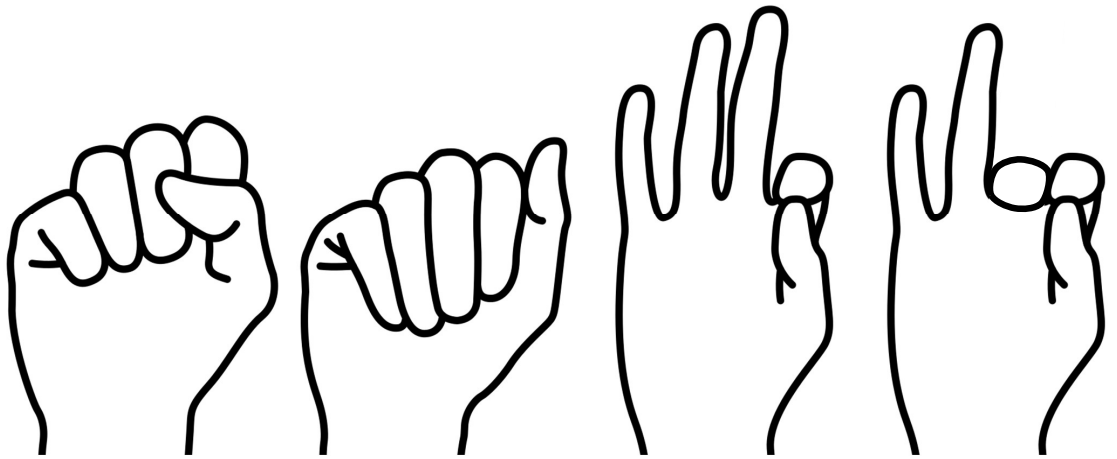

Figure 3.2: This thesis explores the unsupervised classification of intent from sEMG corresponding to the repetition of four unique hand poses used in activities of daily living. These are listed and illustrated above.

3.3 Study #3 Motor Skill Acquisition Model

The third study was developed to compare the behavioral trajectories of human participants performing a visuomotor learning task with the expected performance and skill acquisition profile. This task involved reaching to a sequence of visual targets in a 3D space using the 3D Systems Touch interface as an input device. The experimental platform, adapted from the Reach Ninja paradigm [20], was localized to wrist movements and is herein referred to as Wrist Ninja. Wrist Ninja is a rigorous, goal-directed task that requires participants to maneuver a stylus-operated cursor to contact a series of 3D visual targets displayed on a screen. Targets were randomly placed across a constrained volume and updated every 5 seconds. The task required precise and accurate cursor control using wrist movements alone, presenting a nontrivial sensorimotor mapping and promoting adaptive motor learning over time. The Touch interface served as the physical conduit for recording kinematic performance and delivering trajectory data for analysis.

Fifteen healthy adults (aged 20–35) without prior exposure to Wrist Ninja or the Touch haptic interface were recruited to form a naive participant base. The goal of this study was to validate NeuroSiGHT's ability to capture motor skill dynamics in human motor function, a key capability to enable scalable data-driven HRI design. Results from both human and simulated trials were

analyzed over time, to verify how trajectory accuracy, movement precision, and task error evolved during early and late training stages. Success in modeling skill would be verified by skill ascent matching an exponential profile, which would indicate the utility of a linear second order differential equation model for skill ascent as proposed. The similarity of these behavioral learning profiles across human and simulated learners served as the primary metric for validating NeuroSiGHT's capability in modeling human motor learning under real-world task constraints.

3.4 Study #4: Estimation of Simulated State Transition Dynamics

The fourth study examines the hypothesis that joint motor-cognition between humans and robotic agents can be captured in a bounded exploration topography and navigated to converge to a stable control policy. To evaluate this hypothesis, NeuroMERGE was trained in a simulated passive environment with reliable repeatability between episodes and trials. MATLAB's Cart-Pole (CP) environment was selected for its low dimensionality and fast rendering/reset times which enabled training at higher loop rates and larger time scales than are practical in physical settings. Then, to evaluate the utility of the NeuroMERGE agent in HRI, it was trained in a practical HRI dynamic environment.

The CP simulation renders underdamped second order dynamics of a rod with one end fixed to a rotational joint attached to a sliding cart, functioning similarly to phalanges and pivot joints of fingers, respectively[35] (Fig. 3.3). At each episode, the cart was reset to the origin and the rod was set to a random angular displacement between ± 0.05 radians from the vertical axis. The agent moves the cart in response to observations of rod angular position and velocity and cart linear position and velocity, ($s_T = [x\ \dot{x}\ \theta\ \dot{\theta}]^T$).

The objective of the agent in the CP was to maximize the episodic cumulative reward averaged over epochs of 3 episodes and can be expressed as: $maximize: \frac{1}{3}R = \sum_{i=n+2}^{n} r_{pend}(i)$ where r_{pend} was a binary decision variable taking values of 1 (pendulum has not yet fallen) and 0 (pendulum has fallen) for each time step within an episode. The maximum possible average episodic reward was 250 (maximum no. of steps/per episode), and the episode was concluded when the pendulum

falls beyond 12° of the perpendicular axis. The agent's training was concluded when the average episodic reward reaches 220, i.e., when 88% success rate for maintaining the pendulum within +/- 12° of the vertical, a nominal standard for RL performance[143].

In this case, the objective was analogous to, but distinct from the objective in the HRI case. The penalty function was implemented as $B = f(R(t-1), \hat{z})$. Fixed constant torque disturbances (0, $\pm$0.125, $\pm$0.25, $\pm$0.5, $\pm$0.75 N) were injected in the simulation to induce exploration along the effort axis. No other non-autonomous dynamics were simulated for CP, i.e., the agent was caused to vary along the effort axis between experimental trials, but only in localities defined by the constant input disturbance as seen in the top right tile of Fig 3.17. In practice, effort provided by the human in HRI schemes would vary with human intervention, but a constant amount of effort was simulated that does not respond to assistance to simplify the experimental parameters. The NeuroMERGE agent was trained with no exploration control, i.e. $B = 1$, then with the proposed control implementation, until the objective was satisfied. In both cases, the agent reached the reward threshold.

To evaluate the practical utility of the NeuroMERGE agent in a dynamic environment, it was trained to minimize user effort during index finger motion with an exoskeleton (Fig. 3.3. This environment enables evaluation of NeuroMERGE in HRI with continuous naturalistic task-oriented volitional effort rather than fixed or no effort levels. To simplify training, the one-dimensional flexion/extension task constraint was leveraged and Markov Blanket established by NM3F to implement NeuroMERGE in a reset-free paradigm in which the agent can iterate episodes while the human operator moves continuously in the state space [144].

Three participants, two male and one female aged 25-30 were recruited. The participants wore Delsys sEMG electrodes on the FDP, FPL, EDC, PT muscles. They were instructed to flex and extend the index finger slowly over 2 second periods while the index actuator of the exoskeleton was driven by a 12V, 1.8 amp (30W) two-way air pump capable of up to 80 kPa continuous vacuum pressure. Actuator pressure was measured with an in-line pressure sensor and participants

were instructed to keep remaining fingers passive. Due to the loop rate (<150 Hz) NeuroMERGE was allowed to train for 60s.

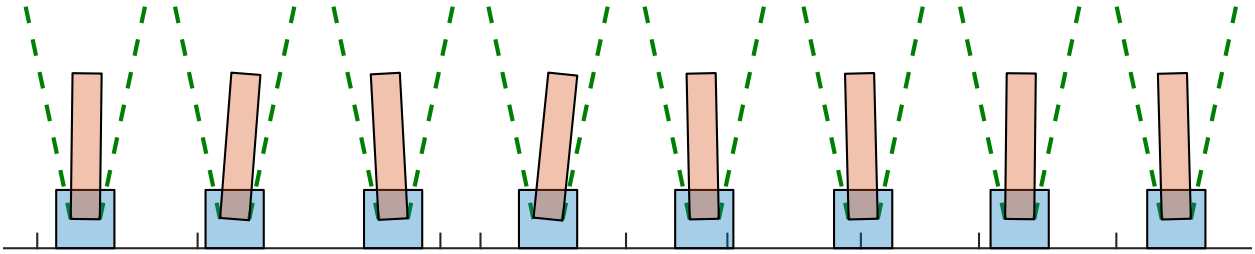

Figure 3.3: A simulated cart-pole environment bearing kinematic similarities to index finger joints was used to evaluate NeuroMERGE. The pole was free to rotate about a underdamped rotational joint attached to a sliding cart controlled by the RL agent. The movement of the cart-pole environment and the performance of the optimized policy are visualized.

The goal of this study was to validate NeuroMERGE's ability to form and navigate a bounded manifold governing the behavior of a controlled dynamic system and the risk associated with exploration actions.

3.5 Study #5 Estimation of Neuromechanical State Transitions

The next study was designed to evaluate the practical utility of NeuroMERGE in online human-robot interaction tasks. To accomplish this, a hand HRI environment was used wherein three adult participants were outfitted with sEMG sensors over the FPL, FDP, EDC, and PT muscles.

The effort estimation model developed in NeuroSiGHT was used to obtain an analog of finger joint mechanical impedance (assuming a-priori a binary intent profile associated with single finger flexion and extension configurations). Participants wore a soft hand exoskeleton and were instructed to flex and extend their index finger slowly every two seconds for 60 seconds (bottom), and the NeuroMERGE agent was trained on-line to minimize effort by driving an air pump to drive the index finger actuator, as shown in Fig 3.4. The MATLAB RL implementation was connected via USB to a Raspberry Pi Pico, which drove an H-bridge motor driver powering a 12V DC pump

Figure 3.4: Three adult participants were outfitted with sEMG sensors over the FPL, FDP, EDC, and PT muscles, and with a soft hand exoskeleton. Participants flexed and extended their index finger slowly every two seconds for 60 seconds, and the NeuroMERGE agent was trained on-line to minimize effort by driving an air pump to drive the index finger actuator.

for the hand pneumatic exoskeleton. The exoskeleton's joints are considered as pneumatically decoupled.

The goal of this study was to validate NeuroMERGE capabilties when connected with NeuroSiGHT's neuromechanical state modeling capabilities for adaptive state transition parameter estimation in a practical data-driven HRI configuration.

3.6 Study #6 Generative Neuromechanical Model-Predictive Control

The sixth study was designed to explore NeuroGAIN in an HRI paradigm comprised of three nested systems shown in Fig. 3.5: the human neuromuscular system (inner), the exoskeleton (middle), and a simulated Box and Blocks Test (BBT) functional task space (outer). In our study, NeuroGAIN-MPC was used in the middle layer with simulated or real human inputs in the other layers.

BBT is a hand functional assessment tool in which participants pick and place blocks from one side of a box to the other over a divider (the BBT obstacle) to demonstrate fundamental motor skills associated with ADLs [145]. Symptoms of neurological impairment, such as tone or spasticity prevent stable object grasping [146, 147] and become apparent with impeded BBT repetition [145].

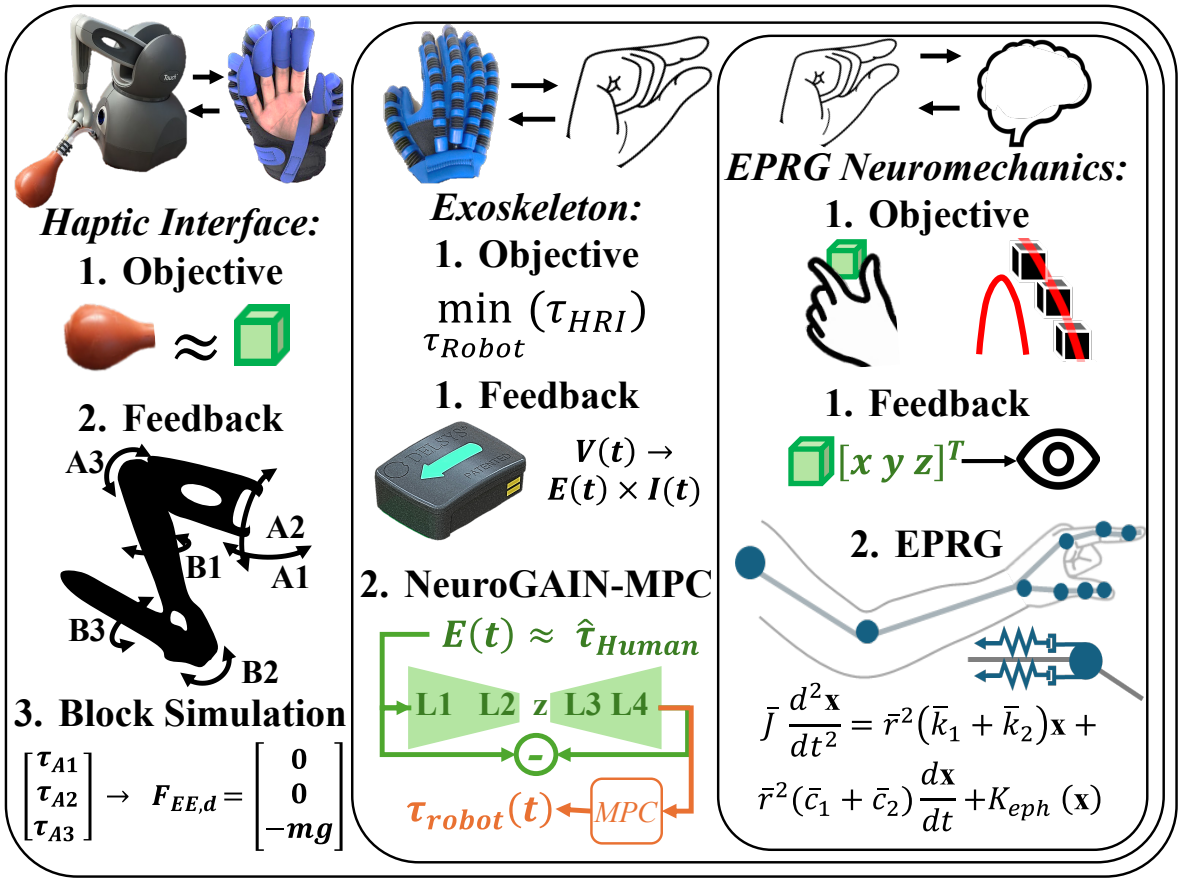

Figure 3.5: Each nested system in our HRI paradigm has an objective, feedback modality and control algorithm. The innermost layer was the wearer, presumed to use visual feedback and EPRG control to achieve a desired block trajectory in the BBT task. The next layer was the hand exoskeleton which uses sEMG-derived inputs and NeuroGAIN-MPC to assist the wearer. Then, the final layer was the haptic interface, which simulates the BBT task. This thesis focuses on NeuroGAIN in the middle layer to augment the mechanical interaction between the inner and outer layers.

Muscle fatigue has also been noted to impede BBT repetition for individuals with neurological impairments, reducing the quality of BBT-based assessment of impairment [148, 149].

Sequential quadratic programming (SQP) was used in a model-predictive control (MPC) setup. SQP iteratively solves a series of quadratic programming sub-problems, that each approximate the nonlinear optimization problem more closely allowing the MPC to handle the nonlinearities and system constraints to ensure optimal and feasible control actions. The SQP subproblem can be formulated at each iteration k as follows, where a quadratic cost function on forecasted neuromuscular demand was $\mathscr{C} \leftarrow \sum_t^{t+h} \hat{E}(t)^2$ with forecast horizon $t+h$ of $\hat{E}$ being obtained from NeuroGAIN:

$$\begin{aligned} &\underset{\Delta\tau_{e,t},\ldots,\Delta\tau_{e,t+h}}{\arg\min} \quad \sum_{t}^{t+h} \left[\nabla_{\tau_{e,t}} \mathscr{C}(x_t, \tau_{e,t}^k) \Delta\tau_{e,t} + \frac{1}{2} \Delta\tau_{e,t}^\top H_t \Delta\tau_{e,t} \right] \\ &\text{Subject to:} \quad x_{t+1} = f(x_t, \tau_{e,t}^k, z) + \nabla_{\tau_{e,t}} f(x_t, \tau_{e,t}^k, z) \Delta\tau_{e,t} \\ &\qquad\qquad \tau_{e,t} t^k + \Delta\tau_{e,t} \in \mathscr{U} \end{aligned} \tag{3.5}$$

Where $\Delta\tau_{e,t}$ represents the change in exoskeleton control actions at iteration k, H_t was the Hessian of the Lagrangian function with respect to $\tau_{e,t}$. MATLAB's `fmincon` function was used with the `SQP` algorithm, which uses a Quasi-Newton method to approximate or update the Hessian matrix, employing the Broyden–Fletcher–Goldfarb–Shanno (BFGS) update formula. Next, $\nabla_{\tau_{e,t}} \mathscr{C}(x_t, \tau_{e,t}^k)$ was the gradient of the cost function with respect to $\tau_{e,t}$ at the k-th iteration, $\nabla_{\tau_{e,t}} f(x_t, \tau_{e,t}^k, z)$ was the Jacobian of the system dynamics with respect to $\tau_{e,t}$ at the k-th iteration. The Lagrangian function for the original problem was given by $\mathscr{L}(x_t, \tau_{e,t}, \lambda) = \mathscr{C}(x_t, \tau_{e,t}) + \lambda^\top (f(x_t, \tau_{e,t}, z) - x_{t+1})$, where λ are the Lagrange multipliers associated with the constraints.

To validate the NeuroGAIN-MPC, a simulation environment was constructed in MATLAB, which enables collection of high-volume training data free from stochastic nonlinearities imposed by physical realities (e.g., intermittent joint torques, surface contact forces, and sensor noise). The environment simulates motor control under the equilibrium point hypothesis via EPRG.

The MATLAB simulation environment featured a model of the human hand with anthropomorphic flexion and extension degrees of freedom (DoFs) in each of the carpometacarpal (CMC), proximal interphalangeal (PIP), and distal interphalangeal (DIP) joints, and abduction/adduction of the CMC joints. To accomplish this, the OpenSIM model was modified to enable whole arm movement (i.e., including scapulohumeral rhythm). Hand link lengths, neutral joint angles, and nonlinear passive joint stiffnesses were designed according to anthropomorphic data.[146, 150] The model was as follows where $\boldsymbol{\phi}_{\mathbf{passive}}(x)$ was the passive torque, a_j and c_j are scaling constants for the exponential terms, b_j and d_j are coefficients that determine the rate of exponential growth with respect to the joint angle, and f_j and g_j are to neutral angles. $\boldsymbol{\phi}_{\mathbf{passive}}(x) = a_j \cdot e^{b_j x + f_j} + c_j \cdot e^{d_j x + g_j}$

Next, the neuromechanical EPRG model of volitional (active) joint torques ($\boldsymbol{\phi}_{\mathbf{active}} = \mathbf{K}_{\mathbf{EPRG}}(x)$) was integrated to obtain a fully defined computational model of human biomechanical and neuromechanical movement. A numerical simulation of the soft pneumatic hand exoskeleton was built based on published model parameters [151]. The hand exoskeleton operates on a contracted set of the state space, x_{hand}, constituting the MCP, PIP, and DIP joints of the index, middle, ring, and little fingers, and the CMC, MP, and IP joints of the thumb. Parameters of the exoskeleton include actuator pressure P, actuator volume V, strain energy density f_F, actuator size f_r, and differential thickness f_D, and flexural rigidity $EIx^2_{hand,n}/2$. Parameters include wall thickness a_e, internal radius b_e, and thickness differential ϕ.

$$\boldsymbol{\phi}_{\mathbf{e}} = \frac{P\Delta V}{x} + \int_0^{a_e}\int_0^{2\pi} \left[f_F(f_r(a_e) + f_D(b_e,\phi))\right] d\phi d\tau + \frac{EIx^2}{2} \tag{3.6}$$

The human-robot interaction dynamics are as follows:

$$\begin{aligned} \boldsymbol{\phi}_{\mathbf{human}}(x,t) &= \boldsymbol{\phi}_{\mathbf{active}}(t) + \boldsymbol{\phi}_{\mathbf{passive}}(x) \\ \tau_{HRI} &= \boldsymbol{\phi}_{\mathbf{human}} + \boldsymbol{\phi}_{\mathbf{e}} \end{aligned} \tag{3.7}$$

The simulation environment, illustrated in Fig. 3.16 includes a block as the virtual object operated through the bulb and Touch interface, which acts as a dynamometer with high surface

friction to measure grasp force and impose quasi-static constraints on finger kinematics. Next a task-level objective of moving the virtual block in free space was encoded to drive the human neuromechanical model. This was done by augmenting the target kinematics, $\mathscr{Y}$, which drive the EPRG problem. Target human joint kinematics were defined which are needed to support the weight of the bulb dynamometer and to track trajectories of the bulb dynamometer in free space to obtain an objective to drive the EPRG model:

$$\mathscr{Y} = \arg\min_{x} \ (||\Sigma_i F_i(x) - W_{bulb}|| + ||P_{bulb}(t) - T_{bulb}(t)||) \tag{3.8}$$

The target trajectory $T_{bulb} = [t \ 0 \ \ sin(t)]$ was designed to correspond to moving blocks from one side of the box to the other over a barrier. The dynamics of the system are given by:

$$\dot{x} = \begin{bmatrix} \dot{\theta} \\ \ddot{\theta} \end{bmatrix} = \begin{bmatrix} \dot{\theta} \\ \mathbf{M}^{-1}(\boldsymbol{\phi}_{HRI} - \boldsymbol{\phi}_{grav} - \mathbf{D} - \mathbf{F}) \end{bmatrix} \tag{3.9}$$

where $\boldsymbol{\phi}_{grav}$ was the vector of gravitational torques, $\mathbf{D}$ was the damping matrix, $\mathbf{F}$ was the friction matrix. The components of the system dynamics include an inertia matrix for the system represented as a diagonal matrix with moments of inertia for each joint $\mathbf{M} = \text{diag}(I_1, I_2, I_3, \ldots, I_{21})$, gravitational torques, passive internal joint damping ($\mathbf{D} = [d\dot{\theta}_1 ... d\dot{\theta}_{21}]^T$) and spring ($\mathbf{F} = [k(\theta_1 - \theta_{neutral,1} ... k(\theta_{21} - \theta_{neutral,21})]$) stiffnesses which sum to provide $\boldsymbol{\phi}_{\mathbf{passive}}$, active torques computed via EPRG which yield $\boldsymbol{\phi}_{\mathbf{active}}$, and gravitational torques computed as follows:

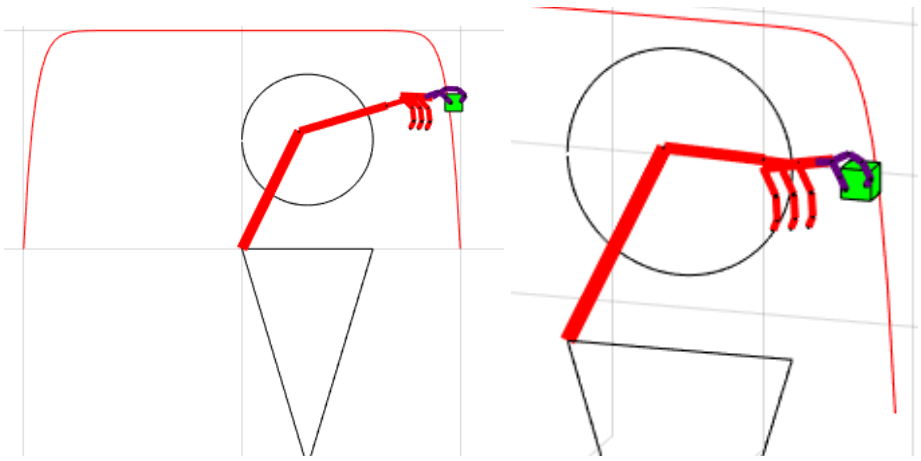

Figure 3.6: In this thesis, we construct a MATLAB simulation environment with EPRG-based control of the 2DoF shoulder, and single DoF elbow, wrist, and finger joints for each of five fingers. We use MATLAB's fmincon function with SQP to deliver joint torques according to the EPRG dynamic model.

$$\boldsymbol{\phi}_{grav} = \begin{bmatrix} 0 \\ 0 \\ 0 \\ m_2 g \frac{L_2}{2} \cos(\theta_4) + m_3 g (L_2 + \frac{L_3}{2}) \cos(\theta_4 + \theta_5) \\ m_2 g \frac{L_2}{2} \sin(\theta_4) + m_3 g (L_2 + \frac{L_3}{2}) \sin(\theta_4 + \theta_5) \\ m_3 g \frac{L_3}{2} \cos(\theta_5) \\ \vdots \\ m_{\text{finger\_DIP}} g \frac{L_{\text{finger\_DIP}}}{2} \cos(\theta_{21}) \end{bmatrix} \tag{3.10}$$

The exoskeleton only acts on the three principle joints of the index and thumb fingers. The shoulder, elbow, and other fingers are operated by the EPRG controller:

$$\boldsymbol{\phi}_{exo} = [\underbrace{0, \ldots, 0}_{6}, \tau_{e1}, \tau_{e2}, \tau_{e3}, \tau_{e4}, \tau_{e5}, \tau_{e6}, \underbrace{0, \ldots, 0}_{9}]^T.$$

Next, it was desired to validate NeuroGAIN-MPC in the physical HRI scheme previously represented in the simulation environment. This HRI scheme was implemented in a study approved by Auburn University's Institutional Review Board (#22-080 EP 2202) that included five healthy adults (three male and two female) aged 20-30. As shown in Fig. 3.7, Delsys Trigno electrodes

were placed on the Digitorum Profundus, Flexor Pollicis Longus, Extensor Digitorum Communis, Pronater Teres, and Brachioradialis muscles. The HRI scheme included human participants wearing the CoTS soft hand exoskeleton on their dominant hands, and manipulating an instrumented bulb dynamometer secured to the end effector of a 6-DoF haptic interface, the 3D Systems Touch.[152]

The Touch haptic interface and a computer monitor provide the participant with a virtual reality (VR) environment where the end effector dynamics simulate the weight of a block in free space. The Touch was augmented with a pressure-sensitive, minimally compressible bulb dynamometer, commonly used for hand grasp measurements [142]. The computer monitor displays a 2D representation of the BBT (as visualized in Fig. 3.7). The participant uses the Touch interface to move the cursor on the screen to a 2D "block" and squeezes the bulb to pick up the block. The Touch interface simulates block weight.

The task involves picking up the block, moving it to the opposite side of the divider, and placing it into the box without contacting the divider (the BBT obstacle) or the simulation environment's borders. The participant performs 75 BBT repetitions while wearing the hand exoskeleton. Of these, 25 were without assistance with 0 kg bulb weight (to ensure minimal fatigue), 25 were without assistance with 0.5 kg bulb weight (to ensure accrual of fatigue), and 25 were with assistance from the NeuroGAIN-MPC with 0.5 kg bulb weight. The trials were performed in this order with 30 seconds of rest between conditions.

The Touch interface simulates the BBT block such that the desired force at the end effector was $\mathbf{F}_{ee} = [0, 0, -mg]^T$, where m was the mass of the block, and g was the gravitational acceleration. The dynamics of the robot are modeled with joint angles θ_{t_1}, θ_{t_2}, and θ_{t_3} that are internally measured, and the forward kinematics maps these angles to the end-effector Cartersian position $\mathbf{P}_{\text{bulb}} = (x, y, z)^T$ for data logging. Joint torques required at each joint to simulate block weight, i.e., basic impedance control, was computed with position feedback using decoupled natural orthogonal complement as described in [39].

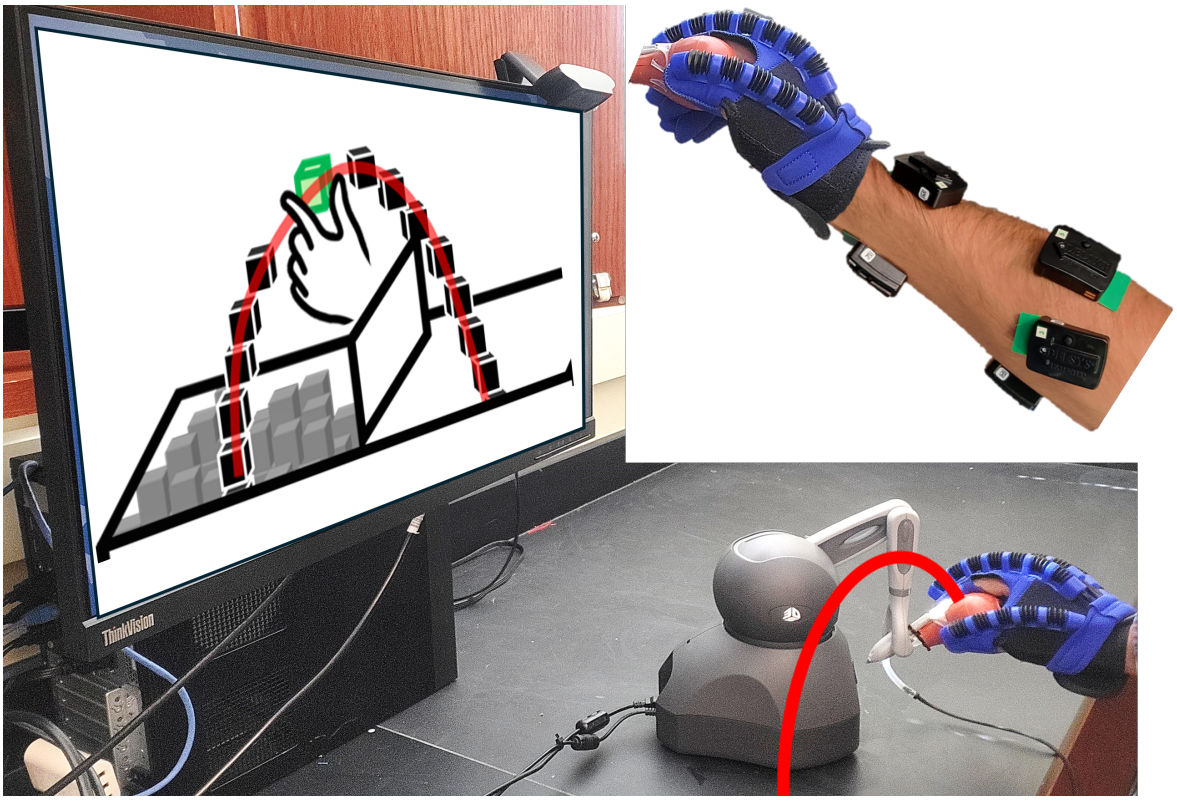

Figure 3.7: A 6-DoF haptic interface was used to render a virtual 2-D BBT task on a computer monitor. The wearer interacts with the haptic interface while receiving assistance from a soft pneumatic hand exoskeleton. The hand exoskeleton was driven using NeuroGAIN-MPC. The haptic interface has a bulb dynamometer attached to its end point to collect grasp pressure. Shown in the inset are the locations of the sEMG sensors. The participant performs 75 BBT repetitions while wearing the hand exoskeleton, 25 without assistance with 0 kg bulb weight (to ensure minimal fatigue), then 25 BBT repetitions without assistance with 0.5 kg bulb weight (to ensure accrual of fatigue), then 25 BBT repetitions with assistance from the NeuroGAIN-MPC with 0.5 kg bulb weight.

The goal of this study was to connect the capabilities of NeuroSiGHT to model dynamic HRI with the capabilties of NeuroGAIN to predict and control HRI trajectories in the neuromechanical regime. This was accomplished in the BBT functional task space with great relevance to rehabilitation applications.

3.7 Study Results and Discussion

Study #1

The results of the first study are presented to validate the muscle synergy-based linear quasi-supervised modeling of intent, effort, and fatigue. The performance of the linear regression model of pose intent trained from a set of four hand repeated poses (PG, LP, TP, and ThP) is shown in Fig.3.8. Next, true and synergy-domain estimated volitional effort levels, and fatigue levels in quasi-static and dynamic conditions are presented (Fig. 3.9). Further, Table 3.1 shows the correlation coefficients (R^2) between effort and fatigue in the estimates as well as the true states as measured from sEMG instaneous amplitude and frequency respectively.

Fatigue, effort, and intent were allowed to vary individually in each of three experimental conditions. True and estimated variability of each state in each condition is described in columns 3, 4, and 5 of Table 3.1, illustrating the reliability of the experimental protocol. To characterize the performance of the synergy-domain linear estimation approach, correlation and root mean square error of estimated intent, effort, and fatigue were examined.

Table 3.1: Descriptive Statistics

	Fatigue-Effort Correlation	$\hat{I}$	E/	F/
Condition	Estimated/True (R^2)	var.	$\hat{E}$ var.	$\hat{F}$ var.
1	0.4053 0.1872	0.00	1.26 1.42	60.45 52.90
2	0.0925 0.1954	0.44	59.12 63.18	0.00 3.36
3	0.0617 0.0047	53.06	1.05 2.48	0.00 0.00

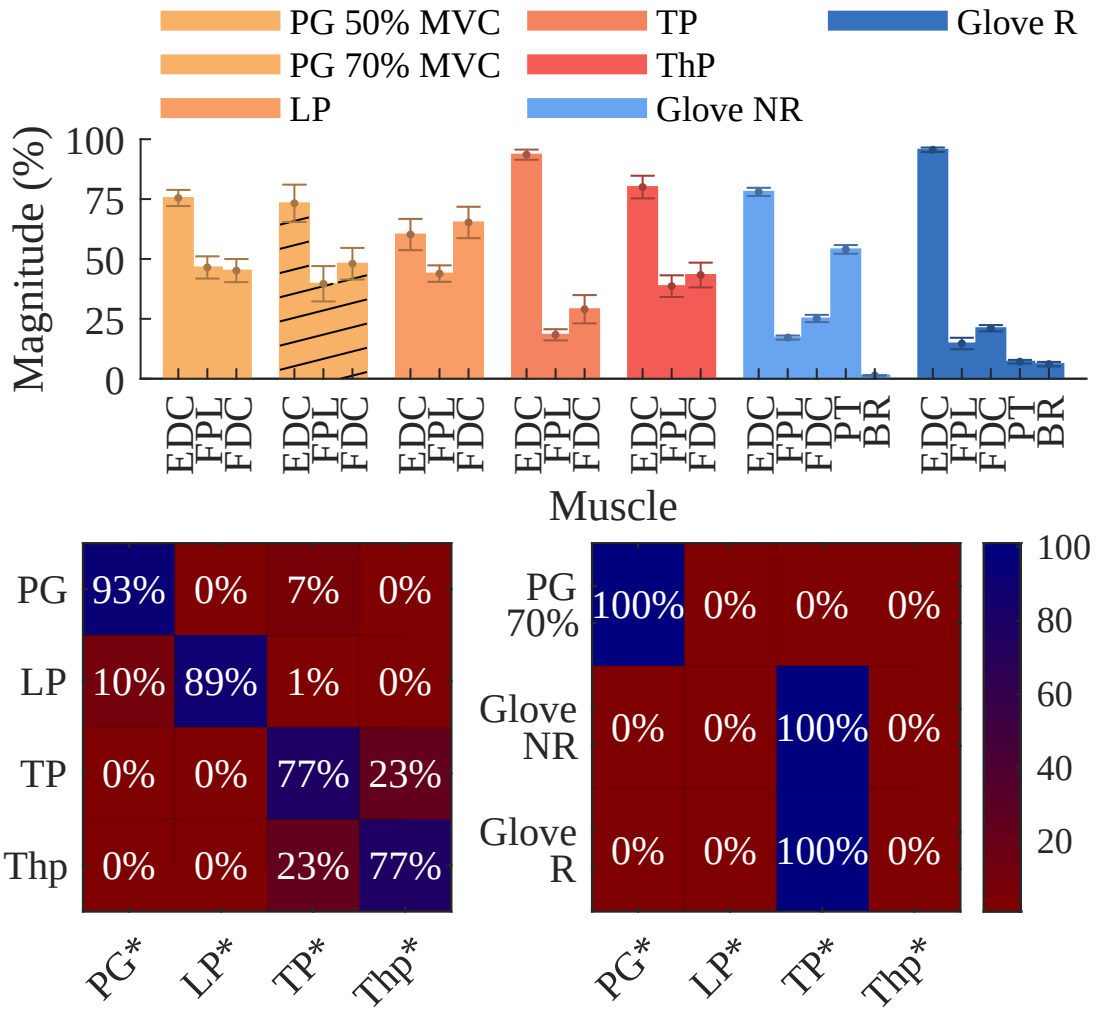

Figure 3.8: Batch normalized spatial synergies are shown as bars (top). The confusion matrix below shows the results of a multiple linear regression model trained on trial data and tested on simulated data including for four hand poses (bottom left), isometric sustained PG (bottom right, top row), and dynamic TP (right bottom two rows) is shown below.

Intent estimation (R^2 = 0.92) had low error rate which corresponded to kinematic similarity in poses [153]; the differences in the kinematically similar two and three finger pinch were harder to discern than other poses. The average RMSE of effort estimation was found to be less than 5% during 50% effort level PG repetitions, less than 20% for 70% effort level sustained PG, 5.6% for gloved no resistance, and 5.3% for gloved resistance trials. The average RMSE of fatigue estimation was less than 1% during 50% effort level PG repetitions, and less than 15% during 70% effort level sustained PG, representing better performance than many conventional sEMG linear time-invariant fatigue estimations [154].

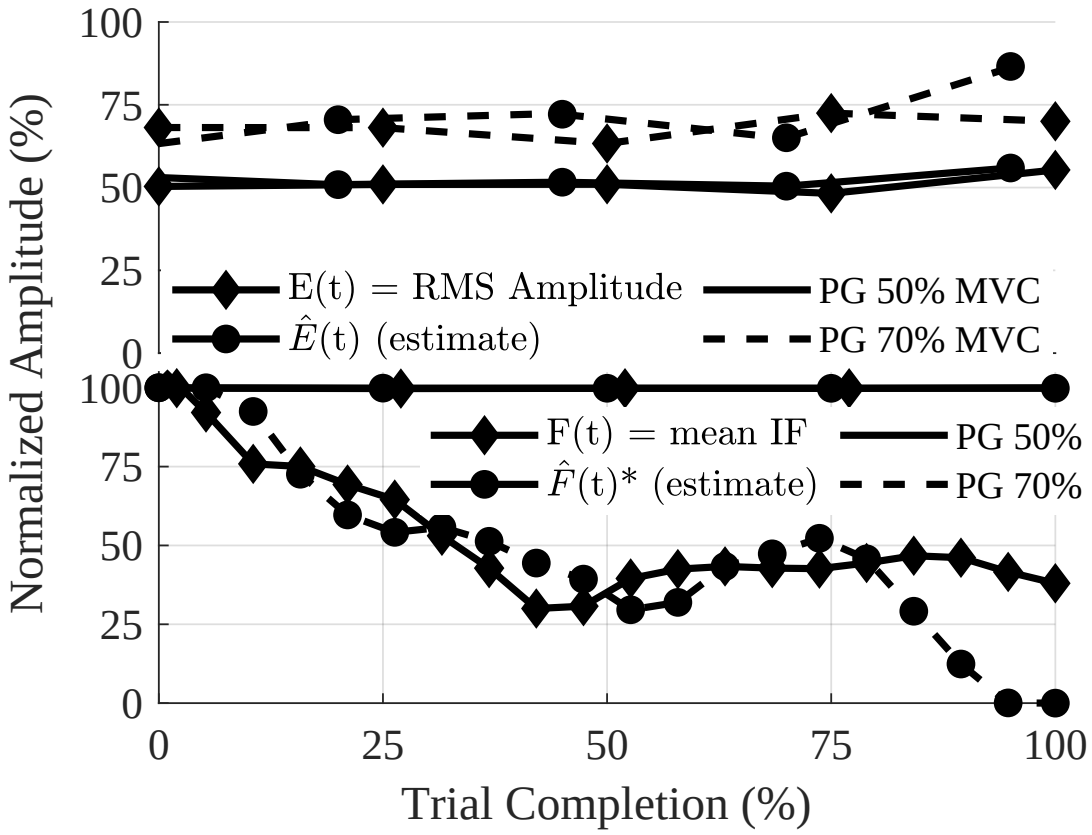

Figure 3.9: True and estimated effort ($E(t)$, $\hat{E}(t)$, top) and true and estimated fatigue ($F(t)$, $\hat{F}(t)$, bottom) are shown for sustained and repeated PG. Average estimation RMSE for 50% and 70% max voluntary contraction PG trials was less than 5% and 20% for effort and 0% and less than 10% for effort and fatigue respectively.

At higher effort levels where sEMG exhibits greater local stochasticity, the linear model with no higher order terms yields poorer yet still competitive performance (i.e., within 10% RMSE of other similar linear estimation approaches, per [154]. Table 3.1 indicates the relatively low R^2 values between effort and fatigue in the true and measured conditions (≤ 0.5) indicating the separation of effort and fatigue in the single linear domain of synergies without higher-order multiple-domain terms.

The results suggest that NM3F, an understood tool for extracting and correlating the spatial and temporal modules of neural signals with movement [92], was a valuable approach to linear estimation of neuromuscular states including intent, effort, and fatigue. These states typically require complex nonlinear analysis to extract, inhibiting their use in conventional HRI control applications.

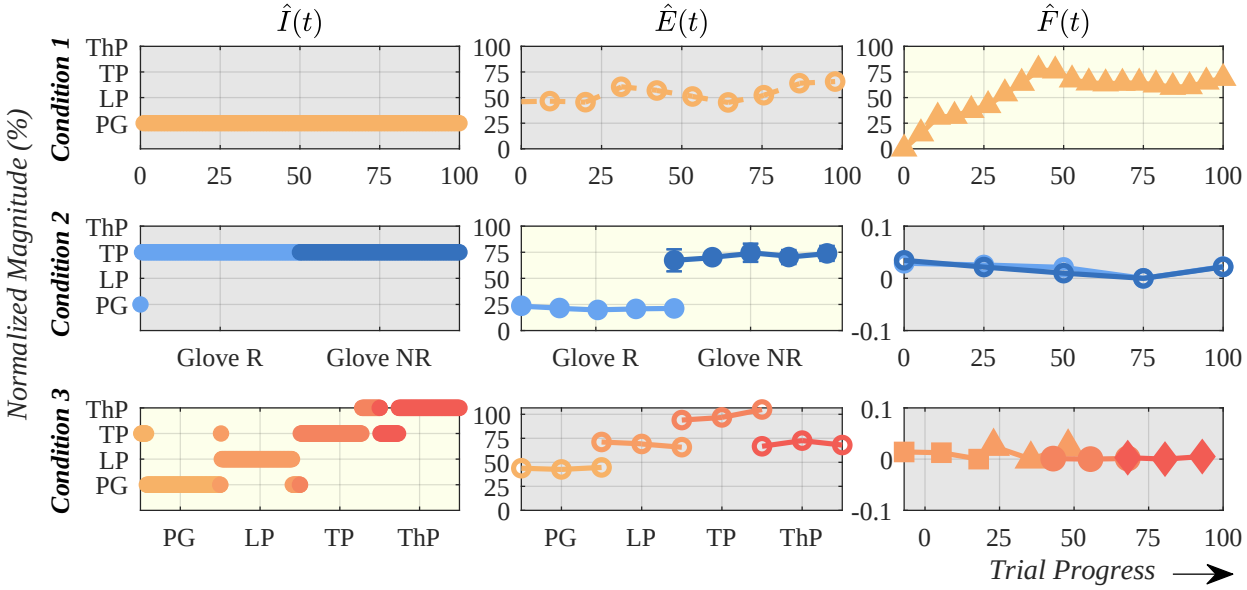

Figure 3.10: Estimation results are shown above for a participant in each experimental condition (Condition 1: intent fixed, effort fixed, fatigue variable; Condition 2: intent fixed, effort variable, fatigue fixed; Condition 3: intent variable, effort fixed, fatigue fixed). In row 1, the effects of fatigue (i.e., 100% - $\hat{F}(t)$) estimated by temporal synergies is shown, while effort and intent remain constant. In row 2, the glove resistance required more effort from the participant, but did not effect fatigue or intent classification. In row 3, the fatigue level stayed constant, and effort levels while not explicitly constrained between poses, remained consistent within poses, which were varied.

The results shown in this thesis suggest these neuromuscular states can be reliably characterized in the space of muscle synergies for HRI control. This solution was relevant in robot-aided rehabilitation, where the effects of muscle fatigue in patient motor performance can be estimated and counteracted while retaining accurate characterization of volitional effort and intent to enable longer duration robust therapy with less discomfort. The measurement model presented here will generate estimates to provide shaped, linear-domain inputs to conventional linear time-invariant control systems, reducing the need for learning-based and/or nonlinear approaches for hand assistive robots to assist unimpaired individuals. This outcome was not available in conventional synergy analysis which could not distinguish volitional effort and fatigue in a linear domain [6].

The results were empirically validated with time- and time-frequency domain ground truth metrics obtained from the raw sEMG vectors. However, several limitations remain to expand and validate the results presented here. First, with regards to the experimental protocol, the static

and dynamic constraints (i.e., rubber bulb dynamometer and robotic therapy glove) may introduce unmodeled statistical nonlinearities. Further, the limited number of participants and limited participant demographics included in this study may limit confidence in the scalability of the results. While the principles presented above hold for locally stable increments of sEMG data for unimpaired individuals, they may break down in cases of nonlinear time-varying neuromuscular impairments, where spatial synergies may exhibit significant time variance and temporal synergies may exhibit significant spatial variance.

During highly dynamic movements such as balancing and reflex tasks, or in cases of neuromuscular impairment like Parkinson's disease, high frequency artifacts can dominate neuromuscular patterns and violate stationary assumptions listed here [16]. However, for the muscles of unimpaired individuals involved coordinated finger flexion and extension for common hand poses, sEMG activation frequencies fall within nominal ranges that are captured by our assumptions of stationary behavior [16, 96]. Higher order parameters can aid in estimation in such cases [94].

Study #2

Next, the results of the second study are presented to validate the unsupervised intent recognition capabilities of NeuroSiGHT both in simulation and with human participants . From the pendulum state vector during simulated performance, a regular subset M of five points was consistently identifiable for each of the three fundamental manifolds corresponding to the pendulum state trajectory. Per the proposed method, these were used to construct candidate manifolds in each of three planes. The percent of data points from the start of each of three set-point switches until the model converged to account for 90% of the variance of orbital eccentricity for the state vector (VAF) was quantified. This "90% VAF time" metric is useful for demonstrating the value of the proposed method in real-time applications; given only a small portion of initial data, the model was able to account for 90% of the variance of the state vector trajectory. For each of the three set

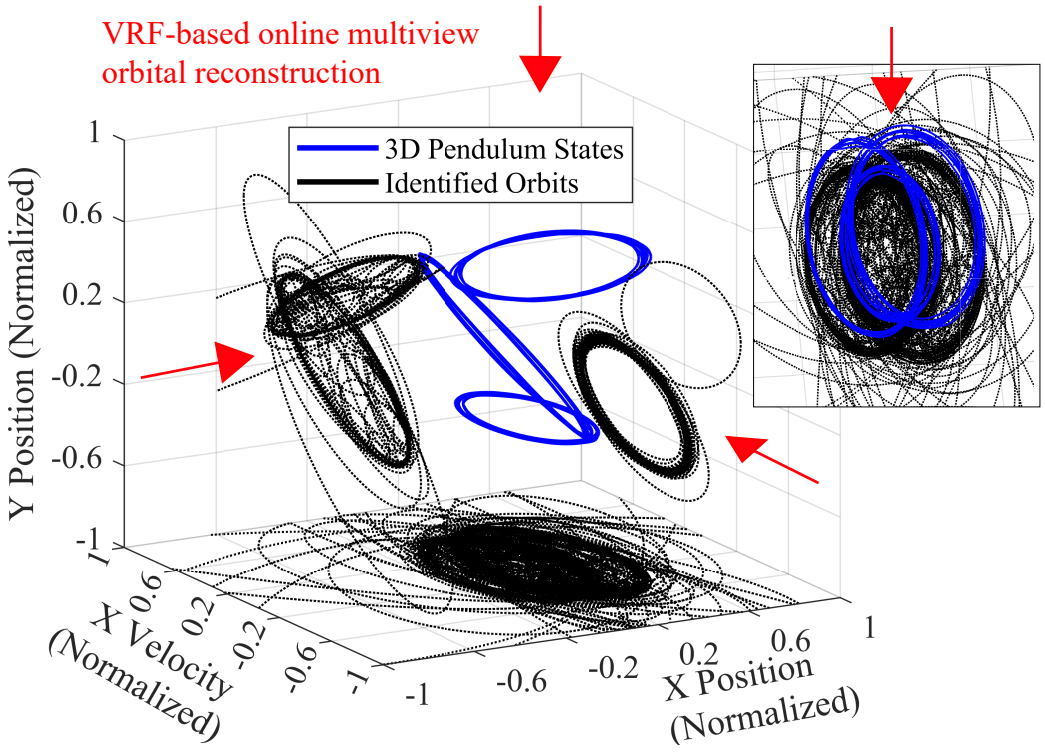

Figure 3.11: Trajectory segmentation and manifold detection using topological filtration. Elliptical regions are accurately identified across attractor switches. The percent of trajectory data required to allow the model to adapt to the new attractor dynamics and account for 90% of the variance (VAF) of the new orbits was 18%, 11%, and 3%.

point changes, the 90% VAF metric for the simulated trajectory was 18%, 11%, and 3%. This enabled resolution of the underlying elliptical structures as depicted in Fig 3.11. Degenerate subsets D (e.g., near-linear sequences) were rejected due to their poor contribution to persistence.

For the case of human participant data, which had four fundamental manifolds corresponding to four hand poses, the This “90% VAF time" metric was 16% for manifold 1, 13#% for manifold 2, 15% for manifold 3%, and 21% for manifold 4.

Due to the spatially mixed chacater of the data, which was less prevalent in the pendulum state dynamics, it was desired to quantify misclassification rates as well. While kinematically distinct poses like PG and LP were not misclassified, kinematically similar poses like two finger and three finger pinch were subject to $>$ 30% misclassification rates.

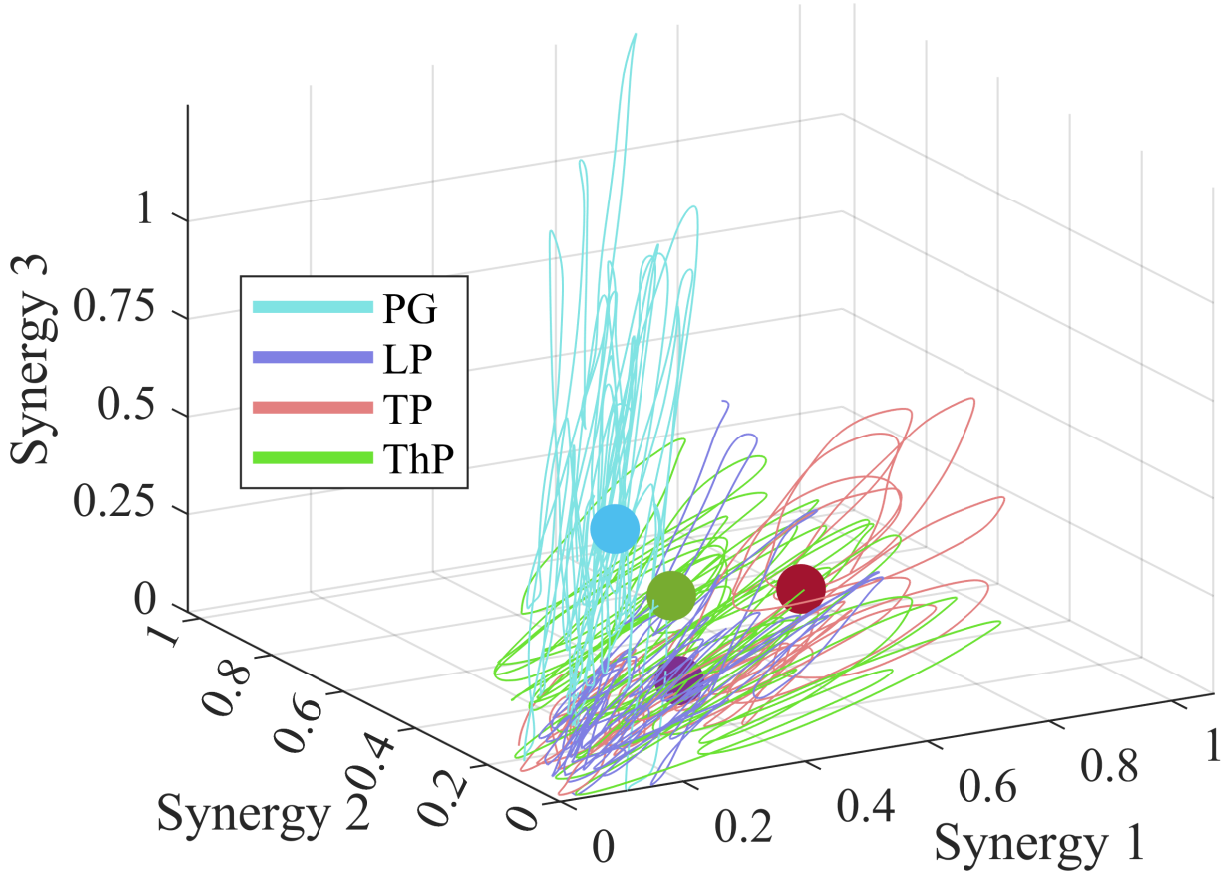

Figure 3.12: The trajectories of the three muscle synergies extracted from sEMG signals are shown, highlighting the mean-reverting behavior of hand pose repetitions. The identified attractors corresponding to the orbits are shown. With $< 21\%$ 90% VAF time, indicating succesful online, unsupervised application, and $< 33.3\%$ misclassification rates for very similar hand poses, e.g., two- and three-finger pinch, the proposed method was successful in unsupervised intent classification for highly mixed signals based on persistent homology of signal trajectories.

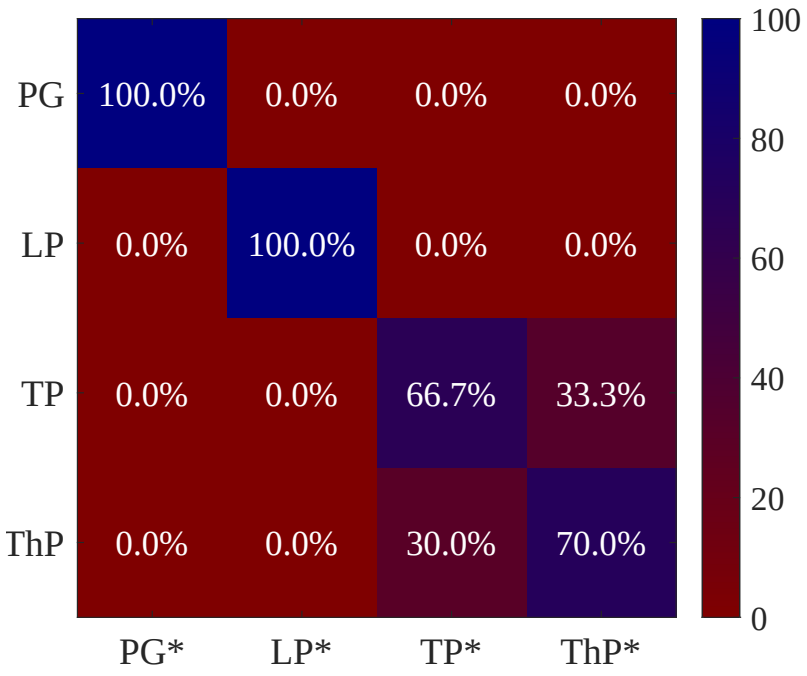

Figure 3.13: Confusion matrix showing the classification accuracy across four hand poses—Power Grasp (PG), Lateral Pinch (LP), Three-Finger Pinch (ThP), and Two-Finger Pinch (TP)—as inferred using the topological classification method. Diagonal elements indicate correct classifications, while off-diagonal entries reflect misclassifications.

The pendulum simulation served as a controlled analog of the human neuromechanical system, enabling a clean demonstration of how piecewise attractor transitions generate bounded, elliptical manifolds in a state-space trajectory. This behavior mirrors observations in the sEMG trajectories of the human hand, where each repeated pose evoked a quasi-stable orbital pattern in the sEMG signal space.

Both systems—simulated and biological—exhibited persistent topological features that could be captured using Vietoris-Rips filtration and resolved using a minimum subset of non-degenerate points. The pendulum simulation offered a noise-free, analytically tractable platform with precisely defined attractors, yielding rapid convergence and high clarity in identifying limit cycles. Specifically, 90% of trajectory variance was captured using just 3–18% of the orbit, confirming that the proposed topological kernel could rapidly recognize transition dynamics.

In contrast, the human sEMG data contained greater variability, sensor noise, and inter-subject differences, yet still gave rise to four identifiable manifolds corresponding to the repeated hand poses. The 90% VAF times ranged from 13–21%, slightly higher than the simulation but still remarkably low for biological data. This indicates that the neuromechanical system of the hand—despite its complexity and signal noise—exhibits comparable persistent structure in control space.

While the simulation cleanly resolved each attractor with negligible misclassification, the human data revealed practical limitations. Misclassification primarily occurred between kinematically similar poses (e.g., two-finger vs. three-finger pinch), where overlapping muscle activation patterns reduced separability. Importantly, however, poses with distinct mechanical demands (e.g., power grasp vs. lateral pinch) remained highly distinguishable.

This result aligns with the theory that manifold separability is a function of both the geometry of the task space and the neuromechanical distance between motor intents. Our method exploits this geometry by mapping persistent topological features rather than relying on high-dimensional raw sEMG variance.

The switching pendulum system can be viewed as a surrogate for the neuromechanical hand, capturing key dynamical features: (1) discrete attractor transitions, (2) quasi-periodic orbit formation, and (3) convergence under bounded noise. This abstraction allowed us to validate core topological mechanisms before deploying them in the higher-dimensional and noisier human system. The consistency of results across domains supports the generality of the proposed method as a latent-state tracker in any system where neuromuscular or control signals evolve on quasi-stable manifolds.

These findings highlight the promise of topological learning in real-time human-machine interfacing. By avoiding overreliance on supervised models or direct kinematic regression, our method enables adaptive, robust inference even under low-SNR or sparse data. The topological basis also offers a compelling model of motor learning, where stable movement patterns emerge through attractor refinement and manifold separation, potentially capturing principles of rehabilitation or skill acquisition.

Study #3

The results of the third study are presented to validate NeuroSiGHT in its capacity to model motor skill acquisition in a complex hand task. Human participants completed iterations of the Wrist Ninja task and their kinematic performance was recorded. Accuracy was measured from distances of movement trajectories from the target point cloud, and precision was measured as average trajectory variance. The results are displayed in Fig 3.14.

It was found that accuracy and precision fit an exponential profile with R^2 of 0.98, and 0.97 respectively. From this, it can be understood that a second order linear differential model for skill ascent with accuracy and precision skill states acting as virtual spring and virtual damping coefficients respectively is an appropriate model for the learning dynamic. Accordingly, the kinematic performance error at the target point reaching reaching task fit an exponential loss with R^2 0.95.

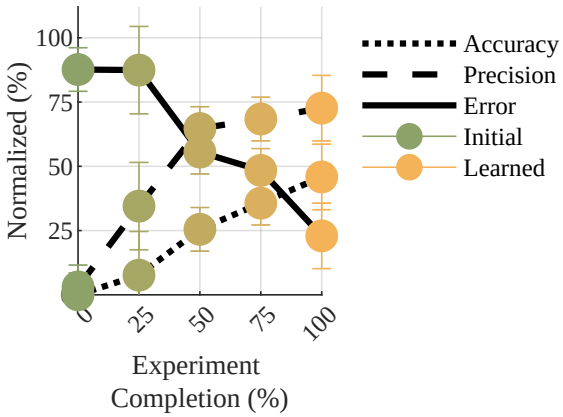

Figure 3.14: Average results for Wrist Ninja performance by fifteen participants over 10 repetitions is shown. The acquisition of accuracy and precision skills fit exponential models with $R^2 > 0.9$, suggesting the reliability of a linear second order differential equation model for skill ascent as proposed.

Study #4

Next, the results of the fourth study are presented to validate the capability of NeuroMERGE armed with NeuroSiGHT intent and effort modeling to form and navigate a bounded manifold for a dynamic system. State trajectories of the traditional REINFORCE and NeuroMERGE agents were recorded during simulated training. In the zero effort condition, with fixed random seed, the traditional and NeuroMERGE agents undertook 358 and 353 episodes, i.e., trajectories, respectively to achieve the preset cumulative sum of rewards threshold (where each trajectory was composed of 250 steps of approximately 2ms duration each). The exploration trajectories, i.e., cart position and velocity, are shown together for each agent in the top left four tiles of Fig. 3.17. The average inter-episodic deviation between trajectories taken by the REINFORCE agent and NeuroMERGE agent were found to be 57% and 42% respectively. Mean episodic ER is a safety metric.

The sliding window σ of the reward signal over epochs of three samples was used to quantify the posterior estimate of risk, (i.e., the Aleatoric Risk, AR, where ER represents the prior expectation of risk). NeuroMERGE control profile for varying effort levels with respect to AR is shown in the top right tile of Fig. 3.17), illustrating effort dynamic in the exploration trajectories for simulated constant effort levels.

Exploration trajectories and HRI dynamics (Fig. 3.17) were recorded during NeuroMERGE training in the hand HRI environment. The convexity of the control profile according to the safe set was indicated by the superimposed surface. Mean inter-episodic HRI performance including human effort, agent control action, and measured index actuator pressure are shown for a characteristic participant (participant 1) in the bottom row of Fig. 3.17.

To evaluate the hypothesis, safety and efficiency of exploration by the traditional RL and NeuroMERGE agents during training in the CP environment was characterized. Both the traditional and NeuroMERGE agents converged to a stable control policy in approximately 150s in the zero effort case; NeuroMERGE has comparable convergence efficiency with the traditional RL agent, and training time was not substantially impacted by the introduction of the penalty but was governed by the physical dynamics. Next, exploration trajectories for the traditional agent exhibited 15% more average inter-episodic deviation than the NeuroMERGE agent, indicating more widely variable exploration trajectory as depicted graphically in the top left four tiles of Fig. 3.17.

The three-dimensional distributions in the top right tile of Fig. 3.17 depict the tendency of the NeuroMERGE agent to avoid potentially risky states during the initial exploration (lighter colored points where $\leq 50\%$ of the training risk was experienced) and to take progressively riskier actions with growing confidence (darker colored points exceeding 50% risk). By contrast, the traditional unbounded agent initially explored high epistemic risk conditions with highly dynamic moves (lighter points exceeding 50% risk). These results together indicate that the NeuroMERGE agent was competitive with the traditional agent in exploration efficiency and outperforms the traditional agent in exploration safety.

Study #5

The results of the fifth study are presented to validate performance of the NeuroMERGE agent in HRI manifold navigation. The NeuroMERGE agent began exploration with low control dynamics under high expectation of risk (light markers starting below and away from the dark markers focused at the center in the bottom row of Fig. 3.17) and concluded training (dark

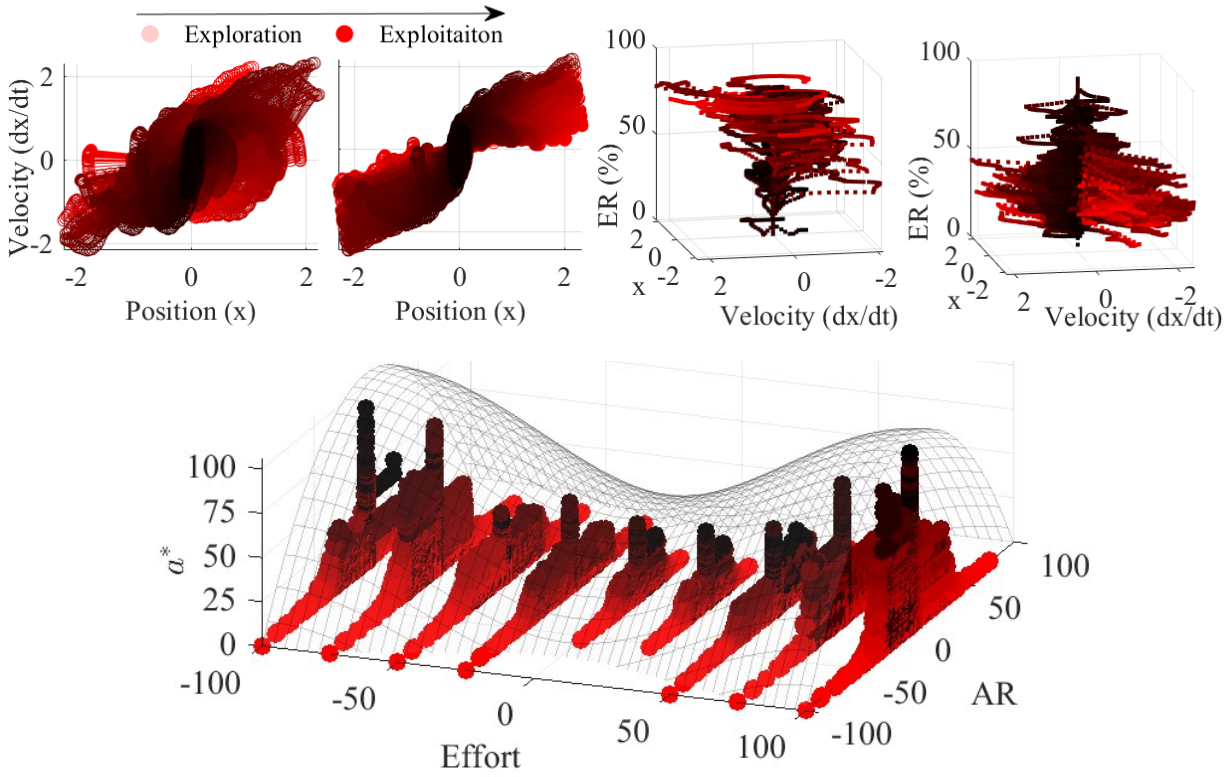

Figure 3.15: Phase portraits of the state exploration by conventional REINFORCE RL and NeuroMERGE agents (top left pair of tiles) and as well as 3D portraits illustrating risk (top right pair of tiles) in the CP simulated environment are shown. These illustrate the efficiency of exploration per the spread of the exploration trajectories and three dimensional distributions of risk with respect to the exploration trajectories. The immediate exploration of high risk states by REINFORCE is shown and the gradual exploration of high risk states by NeuroMERGE is apparent, illustrating the enhanced exploration safety of the NeuroMERGE agent.

color markers at the center of the space) with low expectation of risk and minimal episodic human effort. For each participant, mean episodic effort tended toward zero demonstrating subject-independent high-bandwidth 'tracking' of effort with rise-times competitive with modern control schemes. NeuroMERGE converged safely and efficiently to a stabilizing control policy in the HRI study by navigating a multivariate non-convex exploration trajectory, satisfying the hypothesis.

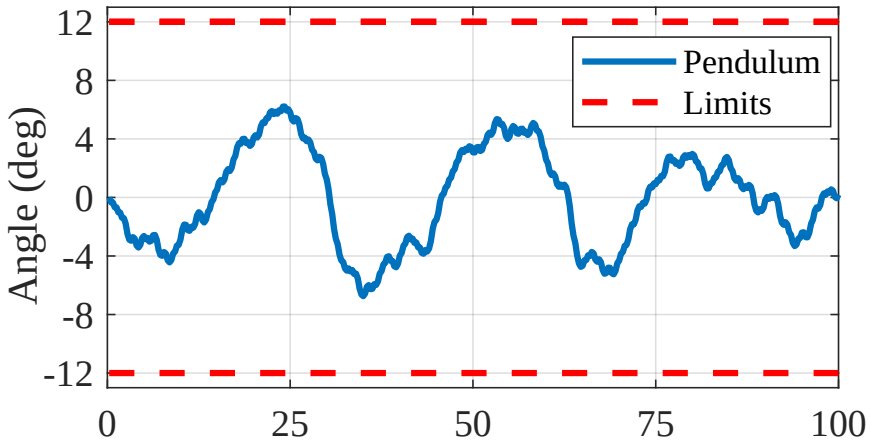

Figure 3.16: NeuroMERGE-based control of a cart-pole environment resulted in a succesful control policy with steady state behavior within prescribed bounds.

Study #6

NeuroGAIN-MPC was validated in simulation and experiments, to compare human-only and NeuroGAIN-MPC assisted performance in BBT without fatigue, with fatigue, and with assistance [148]. It was hypothesized that NeuroGAIN-MPC reduces neuromuscular effort and fatigue via predictive assistance.

The results from the MATLAB simulation are shown in Fig. 3.16, including virtual block trajectories in free space and cumulative volitional joint torques for the simulated participant performing BBT with a 0.5 kg block (without assistance: no fatigue and fatigue, and with assistance: MPC and NeuroGAIN-MPC). MPC was implemented in simulation because the model of the human was fully known ahead of time. Results demonstrate that that effort - measured in simulation by cumulative EPRG joint torque - required to complete the BBT without modeled fatigue (i.e., a baseline metric) was $53\% \pm 4.4\%$ higher with no assistance than with assistance by a classical MPC, and $66.8\% \pm 6.2\%$ higher than with assistance by NeuroGAIN-MPC.

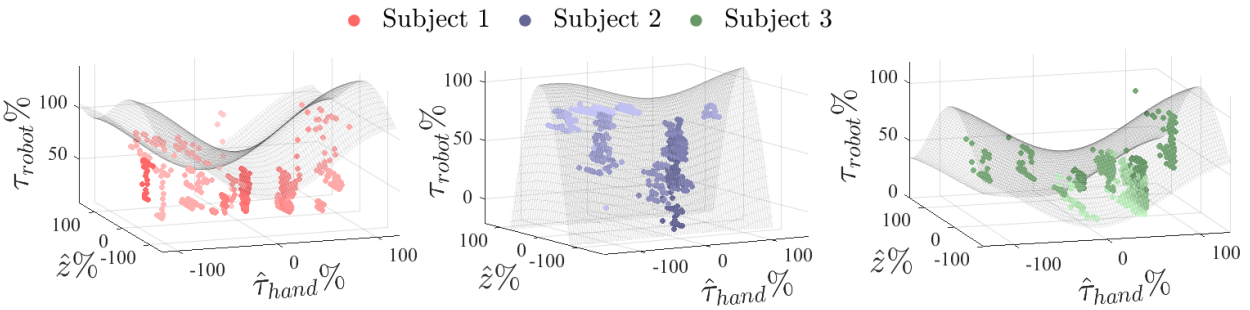

Figure 3.17: The performance of NeuroMERGE in the soft exoskeleton control study are shown below, where concatenated 3D distributions with respect to effort and AR reveal the predicted non-convex dynamic control profile of NeuroMERGE, which satisfies the hypothesis. NeuroMERGE exhibited the hypothesized non-convex dynamic exploration profile evidencing safe and efficient exploration during continuous user volitional effort. In both cases, the policies converge toward the origin of the state space, where the objective was minimized.

When fatigue was introduced via the previously developed data-based model $\mathscr{M}$ [1], the EPRG-based human neuromechanical analog was unable to avoid the BBT obstacle. Reduction in neuromuscular effort is a standard posteriori metric for muscle fatigue [6, 94]. The fatigue model, $\mathscr{M}$, drove the 46% reduction in effort from the start to the end of the trial. Muscle fatigue was indicated by the reduction of effort from the level required to successfully complete BBT, and was reduced with assistance.

Representative results from a single participant - P.1 - performing 25 BBT repetitions are shown in Fig. 3.19, including average movement trajectories with 95% confidence intervals and $\hat{E}$ from sEMG. This participant was able to sustain effort with less than 25% loss from the start to the end of the experiment and successfully avoid the BBT obstacle without fatigue in the 0 kg block condition. In the 0.5 kg block condition, with assistance from NeuroGAIN-MPC, the wearer required an average of 60.8% less effort to successfully complete BBT, and without assistance, effort reduced from the required level by over 55% from start to end, resulting in 30.6% of trajectories in obstacle collision, as visualized by the shaded confidence interval. MPC was not implemented here since the human model wasn't known a-priori.

Shown in Fig. 3.20, for the representative participant, NeuroGAIN was able to track effort with RMSE of 14.2%. During online control, NeuroGAIN predictions attained a mean percent

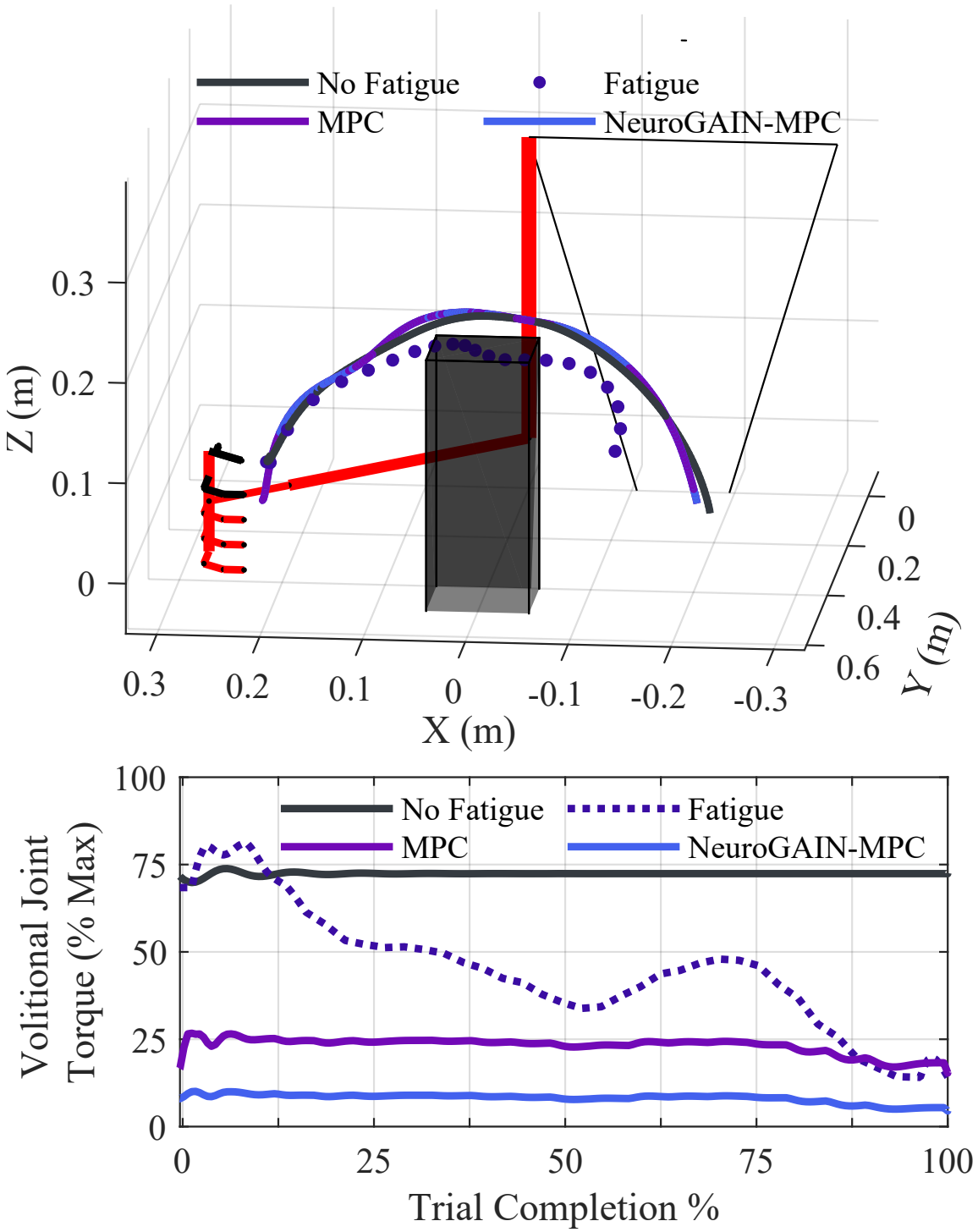

Figure 3.18: The simulated block trajectory for each of the human-only (with and without fatigue), HRI with classical MPC, and HRI with NeuroGAIN-MPC BBT conditions is shown (BBT obstacle is represented with as a black prism in the workspace). Both MPC and NeuroGAIN MPC ensure successful BBT completion, whereas human-only with fatigue does not avoid the obstacle. Cumulative volitional joint torques are shown on bottom. Muscle fatigue causes reduction of joint torque and collision with BBT obstacle. Performance without assistance requires more effort and induces more fatigue.

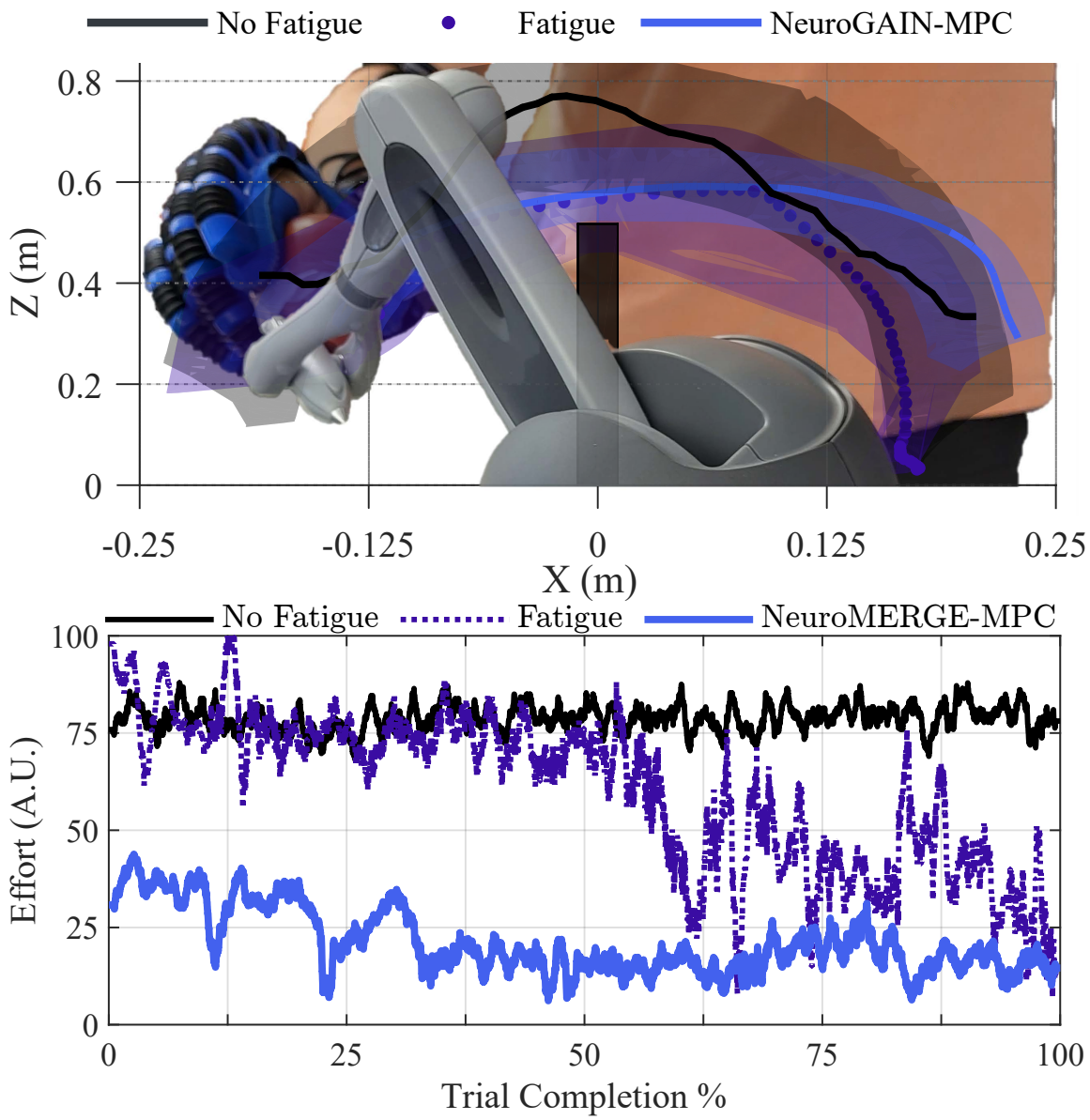

Figure 3.19: Trajectories of a representative participant are shown above, including the bulb trajectory with and without assistance from NeuroGAIN-MPC (top) (BBT obstacle is shown as a black prism). The shaded regions represent 95% confidence intervals. With assistance from NeuroGAIN-MPC, the wearer was able to perform all 25 BBT repetitions while avoiding the obstacle, whereas 25% of BBT trials without assistance yielded obstacle collisions. The effect of muscle fatigue, notable in obstacle collisions in the top plot, is shown on the bottom plot, where NeuroGAIN-MPC assistance reduces fatigue more than when unassisted. The vertical axis is in arbitrary units (A.U.), to show normalized effort. These results align with the simulated performance of NeuroGAIN-MPC to reduce effort and fatigue during BBT.

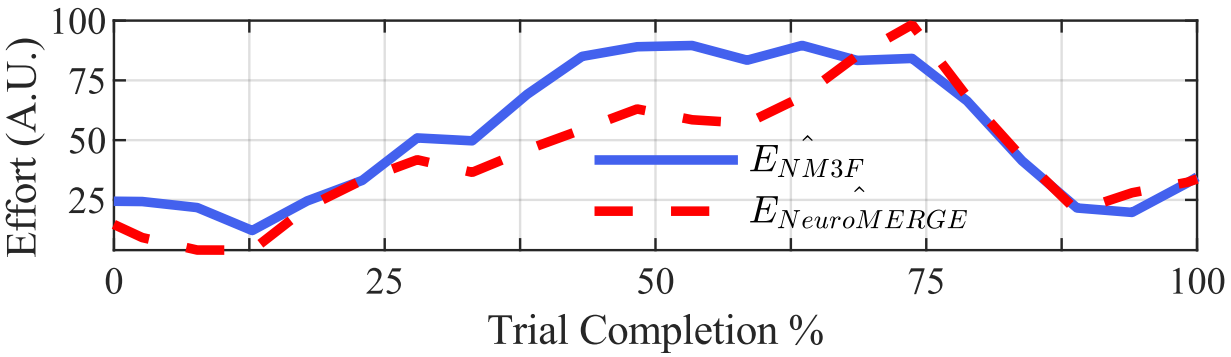

Figure 3.20: NeuroGAIN performance for a single representative participant, with arbitrary units (A.U.) of effort is visualized during a single characteristic BBT trial repetition. NeuroGAIN prediction performance was reliable, with mutual information index of 0.976 and RMSE of 14.2%

mutual information (MI) index (3.11) - a measure of the amount of information one random variable contains about another normalized against the minimum of their entropies H - of 90.9%, indicating modeling reliability. MI is a performance metric used to evaluate the generative model's outputs [155]:

$$\begin{aligned} I(X;Y) &= \sum_{x\in X}\sum_{y\in Y} p(x,y)\log\left(\frac{p(x,y)}{p(x)p(y)}\right) \\ \text{MI}\ (\%) &= \frac{I(X;Y)}{\min(H(X),H(Y))}\times 100 \end{aligned} \tag{3.11}$$

The results for the characteristic participant are representative of the other five study participants, as detailed in Table 1, where a summary description of the human participant results is provided. The results can be interpreted as: No Fatigue condition having high effort, low failure; Fatigue condition having reduced effort, high failure; and NeuroGAIN-MPC Assisted condition having low effort, low failure. NeuroGAIN-MPC assistance consistently reduces effort and improves performance.

The results from simulated and human participant experiments indicated that NeuroGAIN-MPC significantly enhanced the human performance in BBT.

The MATLAB simulation results demonstrate that NeuroGAIN-MPC effectively reduces the effort required to complete the BBT. Specifically, the cumulative volitional joint torque required

Table 3.2: The mean max-normalized $\hat{E}$ (%), % Failure (% of trajectories in obstacle collision), and MI between sEMG-derived and NeuroGAIN-predicted $\hat{E}$ are detailed for the five participants (P.1 - P.5) in each of the No Fatigue, Fatigue, and NeuroGAIN-MPC assisted conditions.

Condition	Metrics	P.1	P.2	P.3	P.4	P.5
No Fatigue	$\hat{E}$ (A.U.)	75.8	96.0	80.8	90.1	96.6
	% Failure	5.6	5.7	6.0	2.8	1.7
Fatigue	$\hat{E}$ (A.U.)	72.0	37.2	41.7	56.4	46.5
	% Failure	30.6	36.1	42.0	25.0	29.9
NeuroGAIN -MPC	$\hat{E}$ (A.U.)	6.0	2.6	1.5	2.6	13.5
	% Failure	11.0	7.6	8.0	6.6	12.6
	MI	90.9	91.4	90.9	94.5	97.6

with NeuroGAIN-MPC assistance was $66.8\% \pm 6.2\%$ lower than without any assistance and significantly better than classical MPC, which does not optimize its internal representation dynamically. This substantial decrease in required effort underscores NeuroGAIN-MPC's ability to optimize control strategies dynamically, accounting for both the nonlinear and time-varying dynamics of human movement, including muscle fatigue. The introduction of fatigue into the model revealed that human-only performance, without assistance, was insufficient to complete the BBT task without collisions, emphasizing the role of assistance in maintaining performance in the simulation environment. The 46% reduction in effort observed with fatigue modeling aligns with established metrics for muscle fatigue [6, 94].

The human participant experiment reinforced results obtained from the MATLAB simulation study. In the human participant experiments, NeuroGAIN-MPC enabled the representative participant to sustain effort required to complete BBT with less than 25% loss over 25 BBT repetitions. Without assistance, in 0.5 kg BBT condition, effort reduced by 55% from the level required to sustain BBT, yielding 25% BBT Failure. With assistance from NeuroGAIN-MPC, the wearer required 60.8% less effort to successfully complete BBT, and obstacle collision rate was reduced to 11%, compared to 30.6% without assistance.

Across participants, assistance with NeuroGAIN-MPC required over 50% less effort to successfully complete BBT with less than 13% failure. Effort level was less in the fatigue condition

than the no fatigue condition, but this is a marker of fatigue [94], which reduced muscle effort capability over time. This was verified in the % Failure quantity, which also increased from no fatigue to fatigue condition. Our findings indicate that NeuroGAIN-MPC reduces the physical burden on wearers but also enhances task performance and safety. The NeuroGAIN model was evaluated to find minimum MI of 90.9% across participants, confirming the reliability of NeuroGAIN's effort prediction model for tracking neuromuscular demands and adapting to wearer needs [155]. The results from all participants are summarized in Table 3.2. The reductions in effort required to successfully complete BBT (mean max-normalized $\hat{E}$) along with reductions in obstacle collisions (indicating the benefit of NeuroGAIN-MPC assistance), and the high MI of the NeuroGAIN model support NeuroGAIN-MPC as an accurate, and reliable method to reducing effort and improving performance.

By alleviating effort associated with rehabilitation exercise repetition, NeuroGAIN-MPC can make rehabilitation less taxing, encouraging sustained participation and adherence to therapy. The consistency of NeuroGAIN-MPC's performance in both simulated and real-world settings highlights its robustness and potential for practical application. The adaptability to real-time conditions and individual wearer variability makes it suitable for deployment in diverse rehabilitation scenarios, ranging from clinical environments to at-home use.

Chapter 4

Embodiments Towards Scalable Data-Driven HRI

This chapter explores virtual and physical embodiments of elements of the computational neuromechanical suite as simulation platforms for scalable and data-driven HRI development applications. First, we build upon the OpenSIM-based virtual embodiment of NeuroSiGHT in the optimization of a haptic policy for two-dimensional point cloud navigation with the 3D Systems Touch haptic interface. The haptic policy selects frequencies and amplitudes for a restorative force that drives the haptic interface to the nearest point on the optimal task path. This represents a challenging data-driven control problem that is difficult to solve due to the scale of the data required to guaratee robustness. NeuroSiGHT addresses this difficulty by providing an anthropomorphic platform for scalable data generation.

Next, we introduce a 3D-printed robotic hand analog that builds on a stream of research associated with anthropomorphic hand manakins [156]. We characterize challenges in the robust control of commercial-off-the-shelf (CoTS) soft hand exoskeletons [157] as a typical optimal control problem (OCP) [158] suitable for a data-reference control policy. We then describe a neuromechanical measurement model that can facilitate data-based linear quasi-stationary solution of the OCP [159]. We further describe the technical requirements for testbed simulation of this neuromechanical model. We present AGeNT, a testbed fulfilling these requirements, and present a case study in which robust optimal data-reference control of a CoTS soft hand exoskeleton is achieved through training with AGeNT.

4.1 Computational Embodiment

First, underpinning works in haptic feedback for hand motor learning, sensory modalities, adaptation mechanisms, and scheduling strategies are briefly reviewed. Haptic feedback plays a

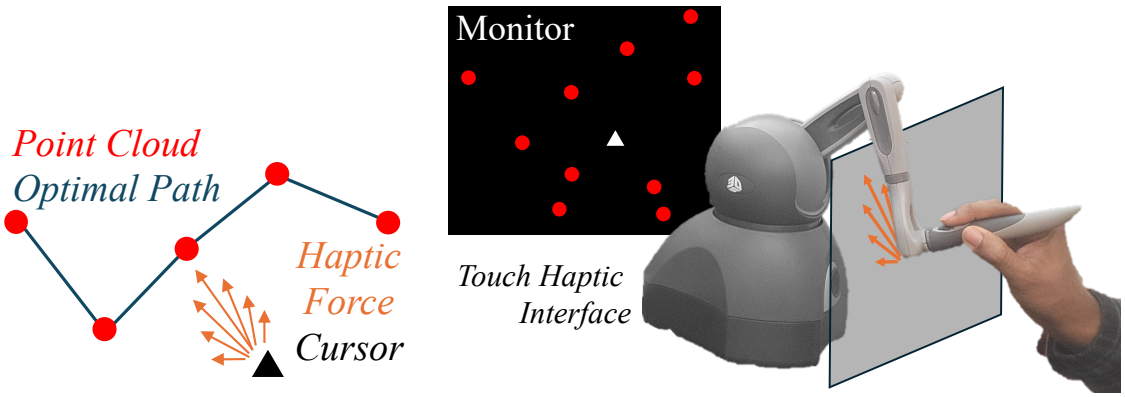

Figure 4.1: The experimental setup and haptic feedback scheme used to explore the capabilities of NeuroSiGHT includes the 3D Systems Touch haptic interface and a computer monitor which displayed a computer animation of a point cloud of 10 red dots which were refreshed to random locations every 5 seconds. Participants were instructed to reach each point on the screen from left to right using the cursor operated with the Touch interface. Precision was measured by average trajectory variance (with respect to a fixed point cloud variance). Accuracy was measured as the distance of the movement trajectory from the point cloud.

critical role in hand motor learning by enhancing proprioception, sensorimotor integration, and formation of internal models for volitional movement control. Johansson et al, 2009 [160] demonstrated that mechanoreceptor signals from the hand are essential for dexterous manipulation, enabling precise force modulation and object interaction. These findings established the importance of both cutaneous (e.g., vibration, pressure) and kinesthetic (e.g., force-feedback) cues in motor control. Expanding on this, [119] described how the brain constructs predictive internal models that integrate sensory feedback to guide movement execution. Their work emphasized that effective motor learning requires adaptive feedback strategies that dynamically update based on task conditions and user proficiency. These foundational studies motivate the development of haptic training policies that not only reinforce motor skill acquisition but also support real-time adaptation to optimize long-term retention and generalization.

Haptic feedback for motor learning can be categorized into cutaneous feedback, which stimulates mechanoreceptors in the skin, and kinesthetic feedback, which applies forces to muscles and joints to guide movement. Lieberman et al., 2007 [161] demonstrated that vibrotactile feedback enhances motor skill acquisition by providing corrective cues, though excessive reliance may hinder retention when feedback is removed. Comparing cutaneous and kinesthetic modalities, [162]

found that cutaneous feedback is superior for tasks requiring precision, while kinesthetic feedback is more effective in force-intensive interactions. These findings suggest that an optimal haptic training policy should integrate both modalities, leveraging their complementary strengths to enhance motor learning, retention, and transferability across different skill domains.

Haptic feedback policies can be classified into fixed policies, where feedback remains constant, and adaptive policies, which adjust based on user performance and task demands. Emken et al., 2007 [85] demonstrated that error augmentation—where robotic assistance exaggerates movement errors—can accelerate learning by promoting active correction, though excessive perturbation can destabilize motor adaptation. Kording et al., 2004 [88] introduced a Bayesian framework for sensorimotor learning, showing that the brain adaptively integrates sensory cues based on their reliability, reinforcing the need for dynamic feedback policies that adjust cue weighting in real time. Patton et al., 2006 [86] further highlighted the importance of variability in haptic training, finding that rigid trajectory constraints impair generalization, whereas introducing perturbations enhances skill transfer. These findings underscore the limitations of static feedback and the advantages of intermittent, adaptive, and probabilistic feedback policies in optimizing skill acquisition and retention.

The timing and frequency of haptic feedback significantly impact motor learning, influencing both short-term performance and long-term retention. Winstein et al., 1990 [163] found that continuous feedback enhances immediate performance but impairs retention, suggesting that intermittent feedback allows for better internalization of motor skills. Marchal et al., 2009 [84] expanded on this by applying the Challenge Point Framework to haptic training, demonstrating that optimal feedback frequency depends on task complexity and learner expertise. Huang et al., 2009 [43] reinforced this by showing that variability in practice conditions enhances motor memory robustness, supporting the idea that scheduled perturbations in haptic feedback can improve generalization. Collectively, these studies indicate that non-deterministic, adaptive scheduling of haptic cues is crucial for maximizing skill acquisition while minimizing dependency on external guidance.

Model-based haptic policy optimization relies on predefined mathematical representations of biomechanics, sensorimotor control, and neuromotor adaptation to generate feedback policies. Todorov et al., [27] introduced optimal feedback control models, demonstrating that the nervous system continuously refines motor commands based on sensory feedback to minimize task error. Extending this, [82] explored impedance control, showing that humans adapt muscle stiffness and damping in response to environmental forces, reinforcing the need for predictive haptic models. Similarly, [164] studied how the brain incorporates sensory uncertainty into motor planning, highlighting the importance of integrating probabilistic representations in haptic policy design. While model-based haptic optimization can offer good performance when human behavior can be accurately modeled, such as during repeatable whole-body movements [45] their sensitivity to model inaccuracies limits their adaptability in dynamic, real-world skill acquisition scenarios, such as in fine dexterous tasks.

Model-free haptic policy optimization relies on data-driven learning techniques, such as reinforcement learning (RL) and adaptive filtering, to refine feedback strategies without requiring explicit biomechanical models. Kormushev et al., 2011 [165] demonstrated that RL can be effectively applied to robotic skill acquisition, allowing policies to evolve through experience rather than relying on pre-defined dynamics. Extending this approach, [166] introduced deep reinforcement learning for continuous motor control, showing that neural networks can optimize haptic feedback policies in complex, high-dimensional environments. Müller-Putz et al, 2022 [167] utilized adaptive haptic guidance in motor training, demonstrating that real-time error correction can enhance skill acquisition in rehabilitation. While these approaches provide flexibility and adaptability, they often require extensive training data, long convergence times, and may struggle with real-time optimization in rapidly changing environments. These limitations motivate hybrid approaches that integrate structured priors (i.e., probability distributions) with data-driven adaptability.

Hybrid haptic policy optimization combines structured prior models with real-time learning to balance efficiency and adaptability. Ngyuen et al., 2011 [50], proposed a framework integrating

model-based and model-free learning, leveraging prior knowledge to reduce the sample complexity of reinforcement learning while allowing adaptation to unmodeled dynamics. Kalakrishnan et al, 2013 [19] further demonstrated that Gaussian Process-based adaptation enables robots to refine haptic policies with minimal data, improving generalization across tasks. Fernandez et al, 2021 [82] introduced techniques to enable systems to rapidly adjust feedback policies based on prior user interactions. These hybrid approaches mitigate the limitations of purely model-based methods, which struggle with real-world variability, and model-free methods, which require extensive data, making them ideal for applications like adaptive motor training and rehabilitation.

For non-stationary nonlinear high-dimensional systems, warm start learning approaches are inherently superior to cold start learning and robust model-reference adaptive control (MRAC). This is due to the sample complexity of learning, adaptation rate constraints, and robustness in uncertain environments. First, per [168], and [169], with $\mathscr{D}$ as the data available for policy learning, N, the number of samples required to achieve an error under $\varepsilon \in [0,1)$ follows a Probably Approximately Correct (PAC) bound, which for cold start, is $N = \mathscr{O}(1/\varepsilon^2)$, and for warm start is $N = \mathscr{O}(1/\varepsilon)$. This highlights the fact that adequate prior knowledge constrains exploration for faster convergence.

Next, if we assume that the same model is used to warm start a learning-based control method and to define the reference model in MRAC, the warm start learning approach still outperforms MRAC due to fundamental differences in adaptation mechanisms, stability constraints, and ability to generalize to non-stationary environments. First, MRAC updates each parameter individually through a gradient-based approach and each dimension must be learned separately over time. warm start learning, however, uses an offline-trained model as a high-dimensional function approximator, meaning it can leverage shared structure across dimensions. A deep neural network can warm start with correlated parameter updates, where MRAC adapts each parameter independently. MRAC needs direct experience in all regions of the state space to adapt correctly, whereas warm start learning can generalize from previous training data to unseen states, reducing required interactions. MRAC adaptation scales poorly because its updates rely solely on real-time tracking rather

than leveraging learned structure. MRAC assumes a structured model, meaning its adaptation is constrained to incremental parameter adjustments. warm start learning can use non-parametric function approximators, such as deep neural networks or Gaussian processes, to better capture nonlinearities. Deep representations in learning methods can also allow higher expressiveness and better nonlinear approximation. MRAC only adapts to the current error, meaning it has no long-term memory of previous system states. warm start methods can incorporate experience replay, Bayesian priors, or recurrent architectures to retain knowledge of past non-stationary shifts.

Algorithm 6 NeuroSiGHT warm started policy Optimization

Initialize parameters θ_0, prior neuromechanical model $\mathscr{M}$, hand-wrist OpenSim model $\mathscr{H}$, task goal q^*, learning rate η, exploration decay γ
Load OpenSim hand-wrist model $\mathscr{H}$ and prior neuromechanical model $\mathscr{M}$
Set $\pi_{\theta_0}(A_0, f_0|e_0, s_0)$ using pre-trained priors from $\mathscr{M}$
Define Gaussian policy priors $A_k = \mathscr{N}(\mu_{A,\theta}, \sigma^2_{A,\theta})$, $f_k = \mathscr{N}(\mu_{f,\theta}, \sigma^2_{f,\theta})$
for each trial $k = 1$ to T **do**
    Compute Sensory Prediction Error: $\hat{e}_k = \frac{\sum_i (w_i P_i)}{\sum_i w_i}$
    Update Equilibrium Point: $q_{\text{EP},k+1} = \pi_{\text{Cognition}}(q_{\text{EP}}, k, \hat{e}_k)$
    Compute Haptic Feedback Action: $(A_k, f_k) \sim \pi_\theta(A_k, f_k|e_k, s_k)$
    Apply Haptic Feedback: $h_k = A_k \sum_{k=1,3,5,\ldots}^{\infty} \frac{1}{i} \sin(t f_k i + \phi_k)$
    Update Skill State: $\mathbf{s}[k+1] = \mathbf{s}_\text{m} - (\mathbf{s}_\text{m} - \mathbf{s}[k]) e^{-\eta(1+\beta|m_k - m_{k-1}|)P[k]} + N([0,0]^T, \sigma_s^2)$
    Compute Policy Gradient: $\nabla_\theta J(\theta) = \mathbb{E}\left[\sum_{t=0}^{T} \nabla_\theta \log \pi_\theta(A_k, f_k|e_k, s_k) R(e_k, A_k, f_k)\right]$
    Update Policy Parameters: $\theta_{k+1} = \theta_k + \eta \nabla_\theta J(\theta)$
    Reduce Exploration Over Time: $\eta \leftarrow \eta \cdot e^{-\gamma k}$
end for
return Optimized policy π_θ

An OpenSIM biomechanical simulation model was used to develop a virtual learner of motor skills based on the NeuroSiGHT neuromechanical framework. The OpenSim ARMS Lab Hand-Wrist Model provides a biomechanically rigorous framework for simulating the dynamics of the human hand and wrist. This model integrates musculoskeletal anatomy, dynamic motion equations, and optimal control strategies, enabling detailed analysis of tasks such as gripping, pinching, and coordinated hand movements. Its design combines experimental validation with computational modeling, offering insights into joint torques, muscle activations, and force generation. The ARMS Lab Hand-Wrist Model includes 23 degrees of freedom (DOFs), distributed across F/E and Ab/Ad joints in the hand and wrist. The model's 22 rigid bodies are parameterized with inertial and

mass properties derived from experimental data to ensure biomechanical consistency. Passive joint properties are modeled as position-dependent torques for each F/E DOF and key Ab/Ad DOFs:

$$\tau = k_p \cdot (\theta - \theta_0), \tag{4.1}$$

where τ is the passive joint torque, k_p is the stiffness coefficient, θ is the joint angle, and θ_0 is the equilibrium angle.

Muscle-tendon actuators follow the Hill-type model, incorporating both active and passive force generation. The total muscle force F_m is expressed as:

$$F_m = A \cdot F_{\max} \cdot f_l(\ell) \cdot f_v(v) + F_p(\ell), \tag{4.2}$$

where A is the muscle activation, $F_{\max}$ is the peak isometric force, $f_l(\ell)$ is the force-length relationship, $f_v(v)$ is the force-velocity relationship, and $F_p(\ell)$ is a passive stiffness.

Tendon slack lengths (ℓ_{Ts}) are computed using the relation:

$$\ell_{Ts} = \ell_{MT} - \ell_M^o \cdot \cos(\alpha), \tag{4.3}$$

where ℓ_{MT} is the musculotendon length, ℓ_M^o is the optimal fiber length, and α is the pennation angle.

The model supports forward-dynamics simulations, enabling prediction of motion and force outputs under given muscle activations. For optimization tasks, an optimal control framework is employed, combining forward-dynamics with simulated annealing to maximize force outputs such as grip or pinch strength. The objective function for grip optimization, for instance, is defined as:

$$\text{Objective} = \sum_{k=0}^{T} \left(F_{\text{grip}} - \lambda \cdot \Delta\theta_{\text{wrist}}\right), \tag{4.4}$$

where F_{grip} is the grip force, λ is a penalty coefficient, and $\Delta\theta_{\text{wrist}}$ represents deviations from the initial wrist posture.

OpenSim's biomechanics engine supports constraint-based simulations using specialized numerical methods. It supports inverse kinematics analysis using nonlinear least squares to align the musculoskeletal model with observed motion data, typically from motion capture systems or IMU data. It supports forward and inverse dynamics using musculoskeletal equations of motion and muscle excitations or joint torques as inputs with numerical integration methods such as the implicit Euler or Runge-Kutta methods to simulate muscle contraction dynamics and joint interactions.

The ARMS Lab OpenSim model (shown in Fig 4.2) provides a detailed biomechanical framework encompassing the wrist, thumb, and fingers with specific degrees of freedom (DOFs), ranges of motion (ROM), and passive stiffness values. The wrist includes two hinge joints: flexion/extension, ranging from -60° to 60° with a stiffness of 0.5 Nm/rad, and radial/ulnar deviation, spanning -30° to 30° with a stiffness of 0.4 Nm/rad. The thumb features saddle joints at the carpometacarpal (CMC) level, allowing flexion/extension (-15° to 15°) and abduction/adduction (-30° to 30°), with stiffness values of 0.8 Nm/rad and 1.0 Nm/rad, respectively. The thumb's metacarpophalangeal (MCP) and interphalangeal (IP) joints, both hinge joints, exhibit flexion/extension ranges of -10° to 50° and -5° to 80°, with stiffnesses of 0.6 Nm/rad and 0.3 Nm/rad.

The index, middle, ring, and little fingers share similar configurations: MCP joints with flexion/extension (-10° to 90°) and abduction/adduction (-10° to 10°), proximal interphalangeal (PIP) joints with flexion/extension (0° to 100°), and distal interphalangeal (DIP) joints with flexion/extension (0° to 80°). Passive stiffness values for these joints are consistent, with 0.6 Nm/rad for MCP flexion/extension, 0.4 Nm/rad for MCP abduction/adduction, 0.7 Nm/rad for PIP flexion/extension, and 0.5 Nm/rad for DIP flexion/extension. This unified structure captures both anatomical accuracy and functional biomechanics. The ARMS Lab model does not feature any time-varying dynamics, like motor skill acquisition.

To evaluate the platform in data-driven haptics, 15 healthy human participants (13 male and 2 female) aged 20 to 35 were recruited to perform a dynamic trajectory task with visual feedback. Of these, 10 randomly selected participants performed the experiment with haptic guidance and 5

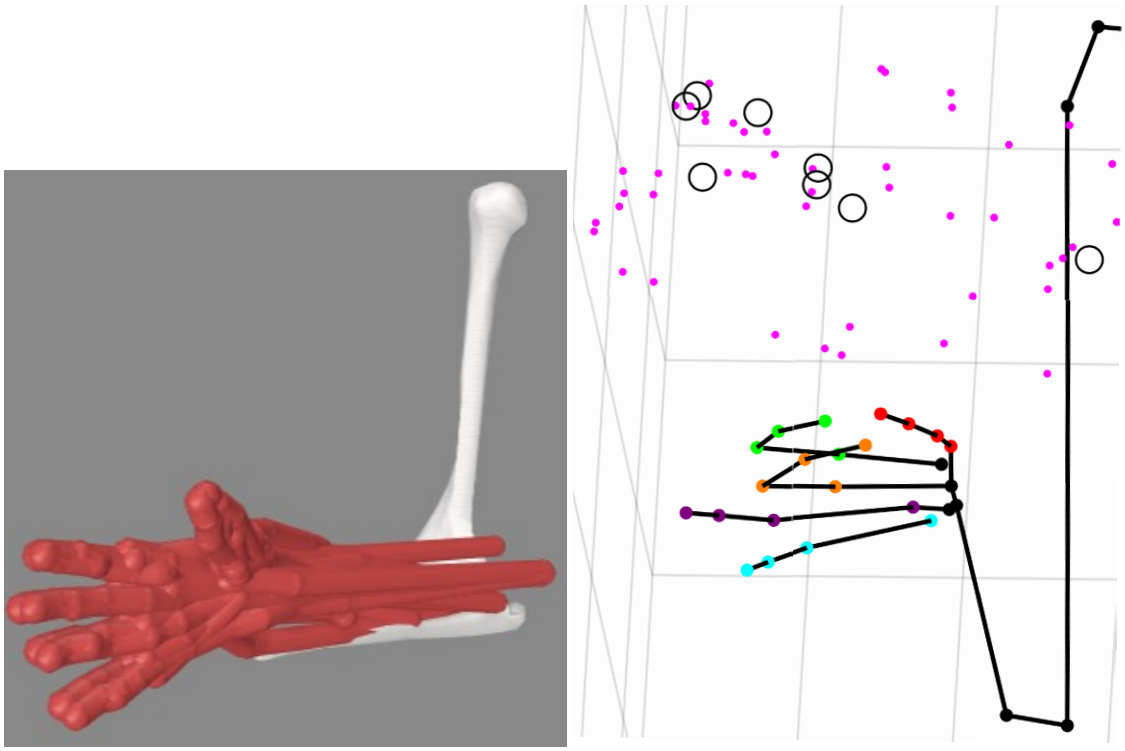

Figure 4.2: The ARMS Lab Wrist and Hand model in OpenSim (left); Example NeuroSiGHT simulation in MATLAB performing a 3-finger grasp and trajectory tracking task in 3D space. The NeuroSiGHT model is subject to biomechanical constraints imposed by the biomechanics engine of the OpenSim Wrist and Hand model (right).

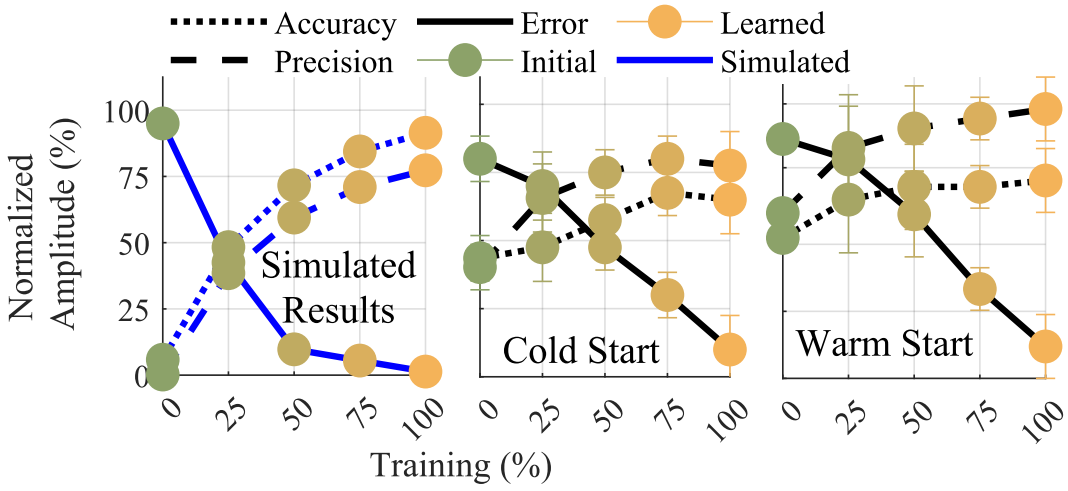

Figure 4.3: Performance of three characteristic participants trained with each of no haptics, cold started, and warm started policies including performance and motor skills in initial (yellow) and learned (green) stages of performance were averaged over training time (%). The simulated results show that trajectory tracking accuracy and precision increase with exponential saturation, while average task error decreases exponentially. This is consistent with human subject results of training and simulated motor skill acqusition (Fig. 3 . 1 4). Training without haptics yields poorer trained performance and poorer skill increase indicated by the final normalized amplitude of tracking error, accuracy, and movement precision. Training with warm start yields better performance, and better, accuracy, and movement precision.

participants did not receive any guidance via haptic feedback. Among those that received haptic feedback, 5 random participants were trained using a cold start REINFORCE, and 5 were trained using a warm start REINFORCE. Both algorithms were implemented resetless with human participants. The simulated learner was subject to the same biomechanical constraints modeled in OpenSim and operated under a probabilistic generative model of internal states including intent, effort, fatigue, and skill. The warm start REINFORCE instance was first trained within the OpenSim NeuroSiGHT environment. The goal of this experiment was to compare the performance of a warm start haptic policy to a cold started policy and to the null policy and quantify differences in motor adaptation and motor performance outcomes in trainees.

The Reach Ninja platform [20], which was developed for whole arm kinematic performance, was adapted to the 3D Systems Touch haptic interface to obtain target kinematics in a field that is localized to the wrist. It is referred to hear as Wrist Ninja. The Touch interface provided corrective guidance, so the task type and difficulty were aligned with the reach ninja scheme, but

the haptic scheme varies to focus on frequency and amplitude characteristics of guidance. The participants were instructed to rest their elbow on an arm chair adjusted to a comfortable height to allow operation of the Touch interface as pictured in Fig. 4.1.

Here we present the results of the human participant study, including simulated results of NeuroSiGHT training, and initial and learned performance and skill acquisition by human participants in (Fig. 4.3). In Table 4.1 we summarize core hypotheses and the corresponding validation from the experimental data.

Table 4.1: Comparison of participants with different training strategies in the task. (all p-values ≤ 0.05).

Hypothesis	**Effect (%)**
Training improves performance over baseline	67%
Training without haptics leads to poorer performance than with cold- and warm start	15%
Training with a cold start policy yields poorer performance than with a warm start	5%
Training with a cold start results in less accurate performance than with warm start	24%
Training with a cold start results in less precise performance than with a warm start	10%

Fig. 4.4 and Fig. 4.5 provide critical insights into the impact of warm and cold started policies on motor learning. Fig. 4.4 illustrates the learning outcome between initial and learned performance of three characteristic participants with no haptics, a cold started policy, and a warm started policy. Fig 4.5 illustrates the improved characteristics of (2.46) for the warm started policy at the start of training by comparing the motor performance of the learner and the frequency domain response of the policy.

The similarity in frequency response of the policies, which indexes amplitude and frequency characteristics of haptic policies, was examined with Rank-biserial correlation (r). The initial warm started policy was closer to the converged policy in either warm start ($r = 0.01$) and cold start ($r = 0.008$) case, than the initial cold started policy ($r = .06$, and $r = 0.1$, respectively).

The results demonstrate that the NeuroSiGHT-based warm start approach effectively accelerates convergence to optimized haptic policies and enhances the acquisition of motor skills like

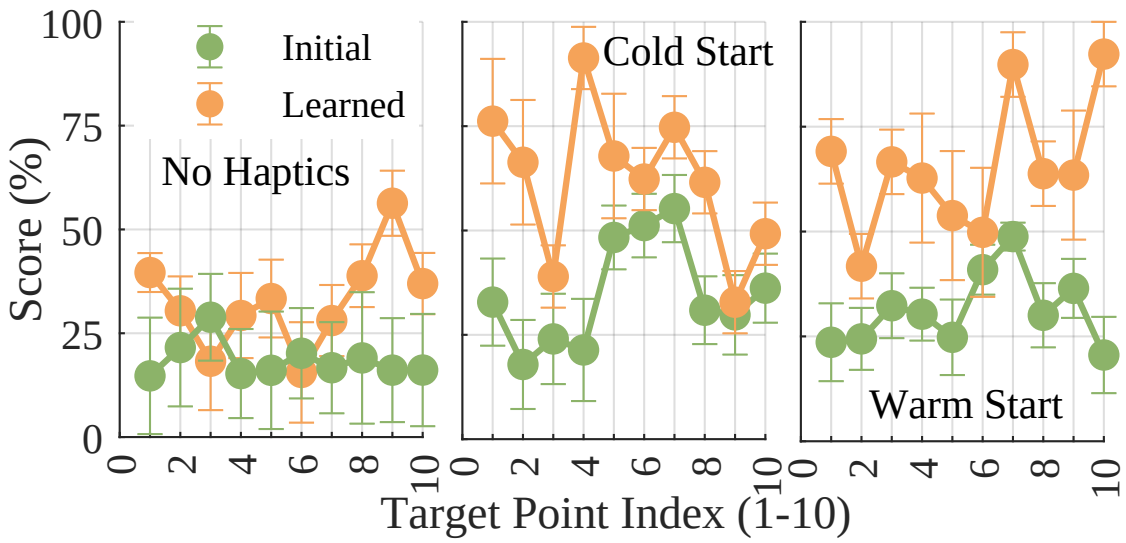

Figure 4.4: Tracking performance for the three characteristic participants, trained in each of no haptics, warm start, and cold start conditions, including accuracy in initial (yellow) and learned (green) stages, were averaged over each of the ten target points of each trial. The results show that trajectory tracking error decreases with training. Training without haptics yields poorer learned performance and training with warm start yields best performance.

movement precision and accuracy. Participants trained with the warm start REINFORCE policy exhibited higher accuracy and precision in tracking task trajectories than those trained with the cold started policy, and both resulted in better performance than training without haptics. The observed improvement in performance accuracy from the baseline suggests that integrating neuromotor control models in the warm start framework results in adaptable haptic policies that are better designed to enhance the formation of motor skills during motor learning.

Participants who trained without haptic feedback exhibited significantly poorer performance than those trained with guidance, supporting the role of somatosensory feedback in skill acquisition. However, the discrepancy between the cold start and warm start conditions emphasizes the limitations of initializing training without structured priors in high-dimensional, dynamic motor tasks. These findings suggest NeuroSiGHT's structured warm start priors improve learning outcomes by stabilizing error feedback mechanisms and reducing cognitive load during adaptation.

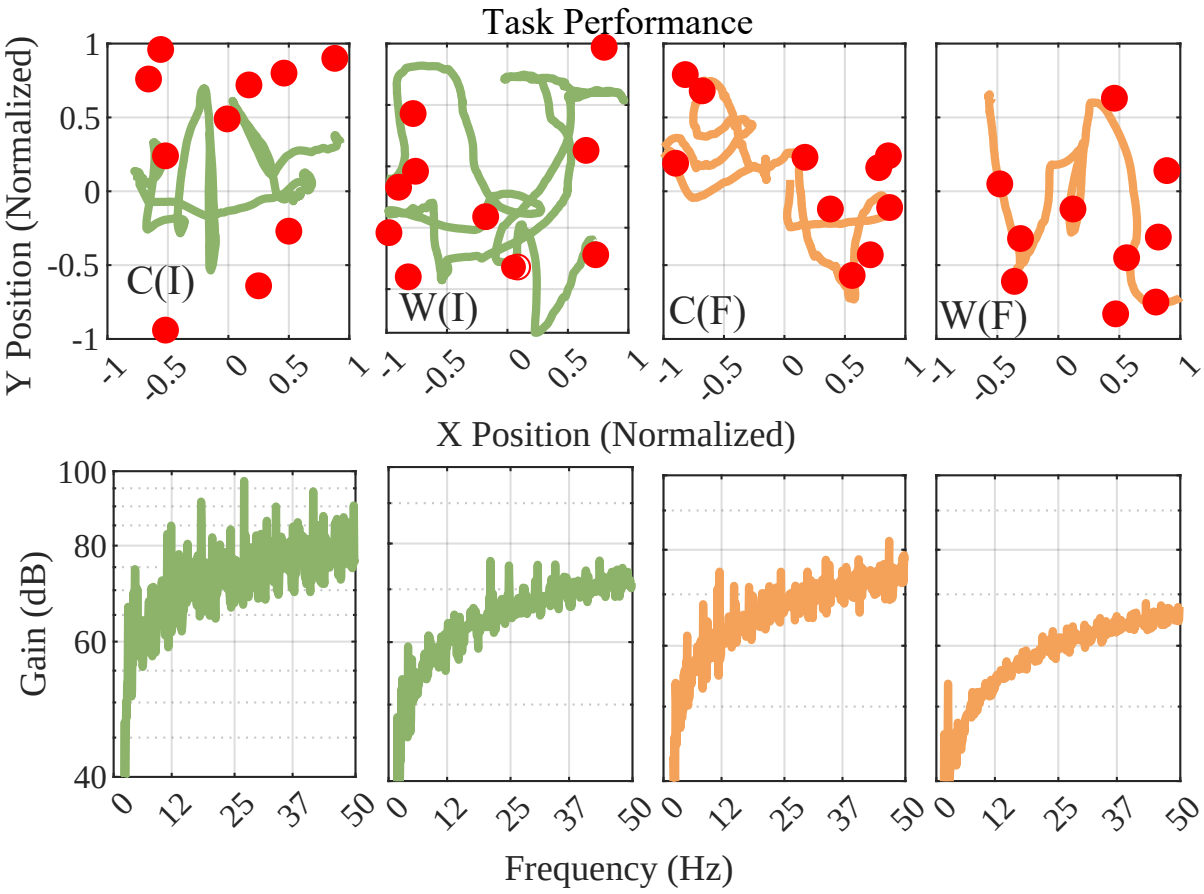

Figure 4.5: Characteristic task performance for a single task repetition (top row) and haptic policy frequency response (bottom) row are shown for the initial (I) and final (F) stages of the cold start (C) and warm start (W) training for the two characteristic participants trained with haptics in Fig 4.3. The warm started policy has the most comparable frequency response and task performance relative to the learned performance in either case. The cold start frequency response and task performance is less similar to the learned state in either case, indicating that the initial warm started policy is closer to the optimal policy.

4.2 Mechanical Embodiment: AGeNT

Hand exoskeletons can deliver assistance and neuro-rehabilitation in at-home contexts [10]. However, many rigid hand exoskeletons are too heavy, costly, and complex for widespread adoption [170]. Soft exoskeletons, with their enhanced manufacturability, usability, and economic feasibility, can help realize the potential of exoskeletons to deliver assistance and rehabilitation. Yet, coupled non-linearities between hand movement dynamics and compliant mechanisms in position and force domains frustrate efforts to deliver optimal control [99] for human-robot interaction (HRI). Data-reference control approaches including adaptive and learning-based control are being explored to address this [129]. But data-reference control requires substantial human participant experimental data which is challenging and costly to obtain. There remains a need for a robust anthropomorphic testbed to help realize the potential of soft devices to deliver comfortable and affordable at-home rehabilitation [44, 129, 144].

This work supports robust and efficient training of data-reference control architectures for soft hand exoskeletons by presenting the design and validation of an Anthropomorphic Generalized Neuromechanical Testbed (AGeNT). AGeNT is a 3D printable hand that mimics the passive and active biomechanics of the hand via closed loop tendon-driven actuation. Further, it integrates a neuromechanical model parameterized with cursory human participant sEMG data, which is well correlated with fine hand motor function while remaining non-collocated with the hand [29]. This enables AGeNT to represent biomechanics and neuromechanics (i.e., representing the neuromotor response of unique individuals to physical intervention). AGeNT is a comprehensive neuromuscular platform to supplant human experimentation.

We consider the robust control of a commercial-off-the-shelf (CoTS) soft hand exoskeleton [157] as a typical optimal control problem (OCP) [158] suitable for a data-reference control policy (Fig. 4.6). We then describe a neuromechanical measurement model that can facilitate data-based linear quasi-stationary solution of the OCP [159]. We further describe the technical requirements for testbed simulation of this neuromechanical model. We present AGeNT, a testbed

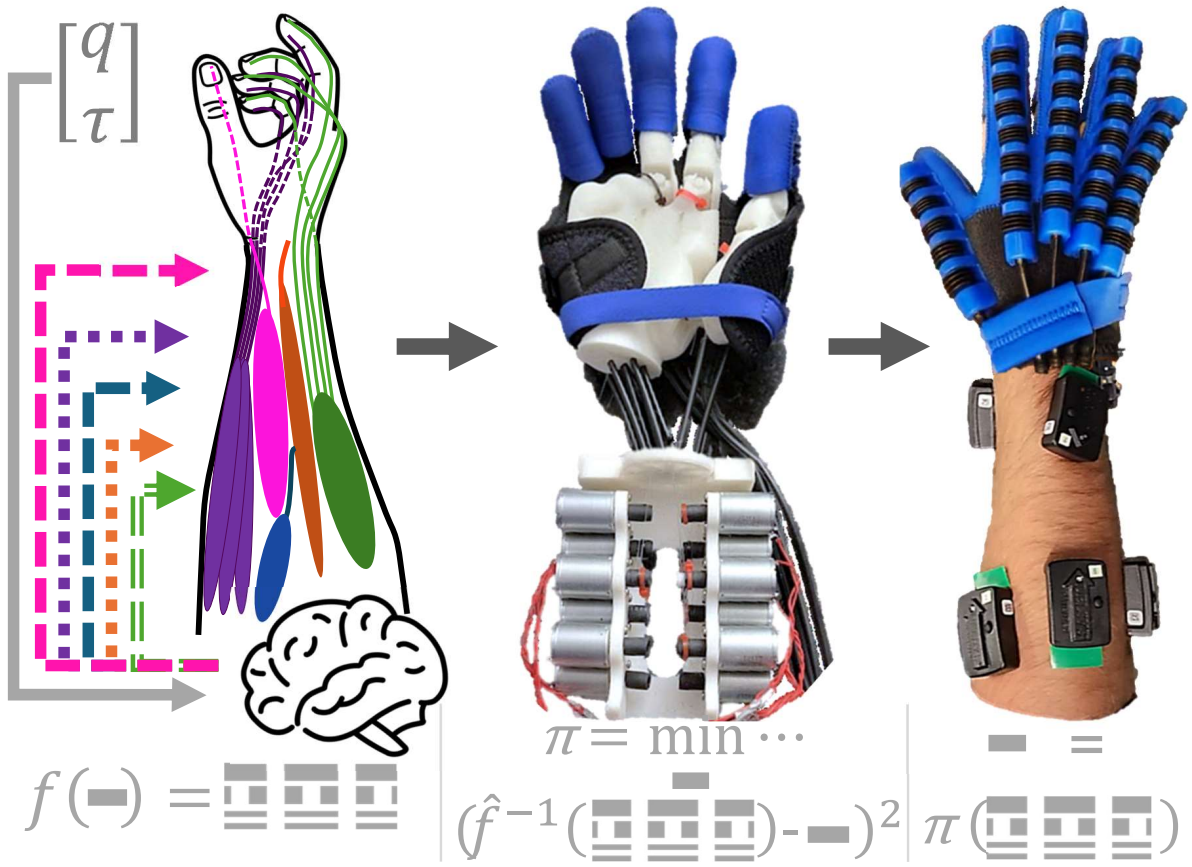

Figure 4.6: In this work, we present the Anthropomorphic Generalized Neuromechanical Testbed (AGeNT) as a simulation platform to train data-driven control architectures for hand exoskeletons. The testbed integrates anthropomorphic size, shape, and joint dynamics with a cohesive computational neuromechanical model to mimic human neuromotor function. As shown on the flow chart above, on the left, we obtained a robust model of the human neuromuscular force control parameterized with cursory human-participant sEMG data explaining how movement control is solved by transforming a mixture (f) of input signals (single solid dash representing visual/proprioceptive feedback) into muscle synergies (three dashed lines). We simulate this neuromuscular model $(\hat{f})$ on AGeNT, representing neuromuscular response to force and torque inputs to train a model-free optimal control policy π for a commercial-off-the-shelf (CoTS) soft exoskeleton. We then implement π on the CoTS device with human participants to find that training with AGeNT produces individualized optimal control policies with minimal requirements for human participant data. AGeNT simulates the biomechanics of the human hand as well as the neuromuscular dynamics of hand neural control to support data-reference exoskeleton control.

fulfilling these requirements, and present a case study in which robust optimal data-reference control of a CoTS soft hand exoskeleton is achieved through training with AGeNT.

Other works have tackled the challenge of representing the human body in a mechanical testbed device. Dežman et al., 2023 [171], proposed a mechatronic replica of the leg to validate lower limb exoskeletons. The ACT Hand closely mimics human anatomical structure and mechanics and has been used to study the intricacies of hand movements and interactions [44]. Other hand testbeds which render the kinematic structure and stiffnesses of human joints (e.g., [156, 172] have been proposed for exoskeleton validation. Several robotic hands (e.g.,[173, 174]), have used anthropomorphic design to achieve impressive dexterity. Each of these devices offer representations of hand physical structure and some of biomechanical function, but none have integrated a neuromechanical model for comprehensive human representation, and therefore none have displaced the need for human participants.

Others have developed computational neuromechanical models, such as Geng et. al., who quantified active joint stiffness control with neural recruitment of co-contracting muscles [99], Massion et. al. who modeled joint and body equilibrium control via the central nervous system to alter movement strategies [38] and Cristiano et. al. who modeled self-organizing neural structures which activate to accomplish whole tasks [175]. These computational models are useful for describing movement control but require a physical embodiment in the form of human participants to produce mechanical outputs. There remains a need to integrate anthropomorphic testbeds with computational neuromechanical models for high fidelity hand representations.

The first line of (4.5), the human-robot optimization problem to which the analytical solution is the optimal control policy $\pi^*_{anl.}$, describes the dynamics of each finger. It includes inertial parameters, M, joint angle-dependent passive viscoelastic stiffness, $\tau_{passive}(q)$, centripetal-Coriolis, C, and gravitational torques G, human volitional effort, τ_{vol} and flexion/extension angle of the fingers, q. The second line of (4.5) describes the dynamics of each serial pneumatic chain along each finger. This includes actuator pressure P (the optimization variable), volume V, strain energy density f_F, size f_r, differential thickness f_D (owing to the saw-tooth configuration of the bellow

surface), and silicone rubber flexural rigidity ($EIX_{i,n}^2/2$, for each of three (i) free human-robot joints per finger (n)), with parameters of wall thickness a, internal radius b, and thickness differential ϕ. More specific definition of these terms and their bounds are published elsewhere [126]. The mechanical impedance, Z, between the human and robot is to be minimized with targeted air pressures P to the serial pneumatic chains.

$$\begin{aligned}\pi_{\text{anl.}}^{*} &= \arg\min_{P(t)} Z(t) \\ &= M\ddot{q} + C\dot{q} + G + \tau_{\text{passive}}(q)q + \tau_{\text{vol}}(t) \\ &\quad - \frac{P(t)\Delta V(t)}{q_{i,n}} - \int_0^a \int_0^{2\pi} \left(f_F(f_r(a) + f_D(b,\phi))\right) d\phi\, d\tau - \frac{EIq_{i,n}^2}{2}\end{aligned} \tag{4.5}$$

In estimating the parameters of the human-robot interaction (HRI) model for healthy adults, we consider hysteresis of human and robot joints to be minimal [176]. Then, assuming an ideal pressure source, the robot design parameters (actuator energy function, profile size and shape, flexural rigidity) can be considered fixed. We assume air to be incompressible, so that the actuator pressure-to-volume relation is fixed and assume minimal loss due to radial deformation. The inertial and gravitational matrices associated with the size and shape of finger links and joint stiffnesses (M, G, C) can be estimated from literature [150].

To solve the optimal control problem, what remains to be defined is the control function f (as shown in Fig. 4.6) mediated by the neuromuscular system to achieve voluntary finger joint torques τ_{vol} in response to the environment. However, volitional muscle control and its associated musculotendinous contributions to finger movement have yet to be globally modeled with the somatosensory input space [81, 99, 175]. This is because human neuromotor control is highly dynamic, continuously variable at the policy level, subject dependent, and variable with high-order psychophysical dynamics like motor skill, stress, and fatigue [23, 24, 81]. It can be shown that such a Partially Observable Markov Decision Process (POMDP) [177] requires continuously variable data-reference control policies to establish provably optimal and robust control [158]. Without an

accurate and reliable holistic model of human neural control, which has yet to be obtained [24, 99, 159, 178], analytical solutions cannot be found, and data-driven solutions are required [177].

One significant neuromechanical feature space for describing human movement POMDPs is muscle synergies, neuronal superstructures which activate multiple muscles simultaneously to coordinate movement [47, 87]. Muscle synergies are modeled by measuring muscle activity, often via surface electromyography (sEMG) [31], which lead kinematic characteristics of movement and while remaining non-collocated with the hand [29]. In previous works [1, 6], we showed that the spatial and temporal muscle synergies composing sEMG signals, V, can be extracted and treated as independent and stationary for 5 ms epochs. We then demonstrated that V from five muscles in the forearm could be reliably decomposed into temporal, W_{T}, spatial, W_{S}, and activation modules, H, to account for over 90% of the sEMG variance using non-negative matrix tri-factorization (NM3F).

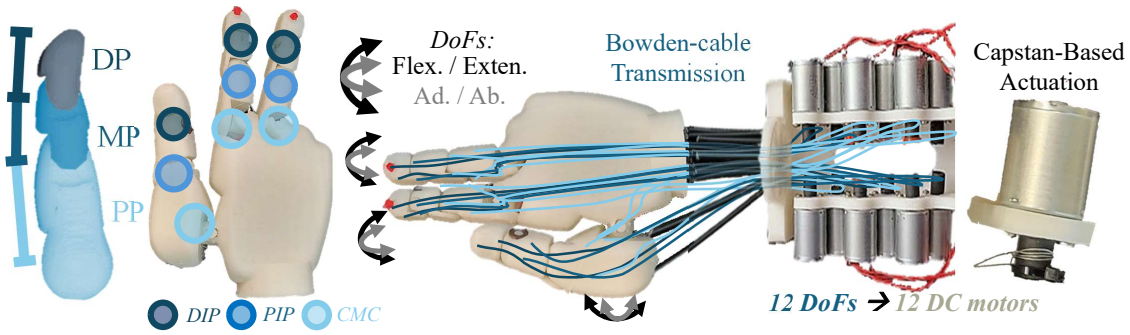

Figure 4.7: AGeNT features anthropomorphic design with the three fingers used most commonly in activities of daily living [44], with (DP), middle (MP), and proximal (PP) phalanges of each finger being independently actuated in flexion/extension and adduction/abduction (CMC joints only) by negligibly extensible bowden transmissions linked to 12 DC motors. The orientations, and ranges of motion (RoMs) of each of the distal interphalangeal (DIP), proximal interphalangeal (PIP), and carpometacarpal (CMC) joint of each finger reflect anthropomorphic data for healthy adults [150]. Tendons are routed through the body of each phalanx and the palm, leaving smooth outer surfaces for robot mounting.

The NM3F algorithm [95] seeds vectors of pre-allocated size and then modifies them to minimize the Frobenius norm sEMG re-construction error. NM3F was implemented in MATLAB, with an iterative update rule on $W_{T,S}$ as defined by [95] with convergence at rates as high as 100 Hz. These synergies can be used to decode time-variable neuromuscular states such as intent and effort. In prior works, we showed that a weighted mixture of spatial synergies yields $\hat{I}(t)$, a reliable

estimate of hand pose intent robust to effort [1]:

$$\hat{I}(t) \Leftrightarrow b_0 + b_1 W_{S,M1}(t) + b_2 W_{S,M2}(t) + b_3 W_{S,M3}(t) = \tag{4.6}$$

Index finger flexion/extension would be described as $\hat{I}(t) = [0\ 1\ 0\ 0\ 0]^T$ (Thumb, Index, Middle, Ring, and Little finger). It has been shown that the activation coefficient H tracks neuromuscular effort [100], and can be extracted as follows, where the number of spatial and temporal synergies are represented by $|nS|$ and $|nT|$:

$$\hat{E}(t) \triangleq \frac{1}{|nS|^{\frac{1}{2}}|nT|^{\frac{1}{2}}} \sum_{i \in nS} \sum_{j \in nT} V_{ij} \propto W_T^{-1} V W_S^{-1} \approx ||H|| \tag{4.7}$$

$\hat{E}(t)$ corresponds to the instantaneous mechanical finger impedance [159, 179], which when mixed with $\hat{I}(t)$, results in a comprehensive linear model of human movement from sEMG signals: $\hat{f}(\cdot) \approx \hat{I}(t) \times \hat{E}(t)$

To represent our computational neuromechanical model, an anthropomorphic testbed must:

- Accurately and repeatably emulate passive (i.e., joint inherent stiffnesses) [150, 176] active hand dynamics (i.e., joint dynamic profile in volitional motion) [44]
- They must model neurological inputs to muscles and how these inputs respond to exoskeleton action to capture the contextualize exoskeleton intervention [99]
- Finally, they must be sufficiently parameterized to mimic the unique differences between individuals to supplant human participant experimentation [25, 180].

AGeNT advances the state of the art by satisfying requirements for accurate, reliable, and repeatable emulation of passive and active hand dynamics. This is accomplished through independent actuation of anthropomorphically designed [150] finger joints by Bowden cable transmission via 12V DC motor capstan drives (Fig. 4.7). Further, it integrates our neuromechanical model (4.8) to represent motor control in response to exoskeleton action with human participant effort signals

to mimic unique differences between individuals. It is fully 3D printable (CAD files available at https://github.com/WeBRAvinash/AGeNT). It is capable of minimizing the need for extensive human testing, setting a new benchmark for developing data-driven control.

To control AGeNT, we rely on equilibrium point (EP) hypothesis [181], by which the brain is thought to perform pre-reference scaling for linear control of joint torques by shifting the internal representation of the equilibrium position (q_{ref}) of joints. By EP hypothesis, to linearly increase or decrease desired joint torque, the brain commands a reference positions to amplify or decrease the position error to a linear neuromuscular controller, f. Using this principle, $\hat{q}_{ref} \propto \hat{E}$ as both are linearly proportional to joint torque. A proportional control law is then used to mimic EP control:

$$\begin{aligned} q_{ref}(t) &\propto \hat{E}_{human}(t,q) \propto \tau_{vol}(t) \\ \tau_{AGeNT}(t) &\approx K_{AGeNT} \cdot q_{ref.} = K_{AGeNT} \cdot E_{human}(t,q) \end{aligned} \tag{4.8}$$

Importantly, per our computational neuromechanical model [1, 6] and EP hypothesis [181], τ_{AGeNT} can be used to model the neural signal V, so that AGeNT is able to simulate sEMG signals associated with HRI. When an exoskeleton moves to change the position of AGeNT's joint, it affects τ_{AGeNT}, which varies linearly with V when intent $\hat{I}$ is fixed. AGeNT can thereby serve as a comprehensive neuromechanical testbed, modeling neural control.

To validate the performance of AGeNT as a testbed for data-reference controllers, we develop a straightforward model-free extremum seeking control law (ESC) for the CoTS hand exoskeleton. We utilize a proportional-integral-derivative law with an adaptive gain K_p which, in essence, solves the following robust optimal control problem to obtain the action of a trained control policy π^*_{ESC}:

$$\pi^*_{ESC}(e) = \min_{a^*} \quad J = e(t)^2$$

Subject to:

$$\begin{aligned} e(t) &= E_{human}(T) - q_{AGeNT} \\ a^* &\triangleq K_p e(t) + K_i \int e(t)dt + K_d \frac{d}{dt} e(t) \\ \dot{K}_p &= -\mu_p \frac{\partial J}{\partial K_p} \end{aligned} \tag{4.9}$$

The ESC gradient-based policy update rules are shown. The control gains allow the policy to adapt iteratively with error-gradient via predefined learning rates μ_p. To reduce computational load associated with computing the gradient, we approximate the control gain with a small sinusoidal perturbation [182]: $K_p(t) = K_{p,0} + \delta K_p \sin(\omega_p t)$

We seek to validate AGeNT's 1) representation of hand passive biomechanics, 2) representation of neurological inputs and kinematic outputs in a position tracking task, and 3) utility as a testbed to train a robust optimal data-reference control system. 1) is accomplished by comparison of AGeNT performance with anthropmetric data, 2) is accomplished using sEMG data recorded during 120 seconds of thumb CMC joint abduction/adduction while holding a spherical instrumented bulb dynamometer between the thumb and index finger, and 3) is accomplished by performing the motor task with the assistance of a soft hand exoskeleton [157].

We first validated the capabilities of AGeNT to mimic the passive and active dynamics of the human hand. Mechanical stiffness mediated by musculotendinous structures drives much of the hand and wrist mechanical dynamics [40]. It was desired to confirm that these biomechanics are correctly simulated by AGeNT. We utilize independent time- (4.10) and frequency-domain (4.11) approaches to estimate the joint stiffness profile of one of AGeNT's finger joints [94] and correlate these results to validate time-frequency invariability of the HRI system. Prior works have provided parameterized exponential models for the stiffness of hand joints [176]. The flexion model is

shown; extension is similarly parameterized:

$$\tau_{passive} = a \cdot e^{bq} \tag{4.10}$$

To establish the capability of AGeNT to represent anthropomorphic exponential finger joint stiffnesses, we command a reference position of $q_{AGeNT,ref} = a \cdot e^{bq_{AGeNT}}$ to the index metacarpal phalangeal joint (MCP) (encircled in Fig. 4.9). We then load the joint using a strain gauge (essentially at 0 Hz), and measure joint deflection to obtain empirical stiffness.

Next, to establish the approximate frequency independence of the HRI system and validate the anthropomorphic finger joint stiffnesses across a space of realistic HRI frequencies (0.1, 0.2, 0.3, 0.4, 0.5, 1, 2 Hz) we excite the index MCP using the CoTS soft exoskeleton. To achieve frequency-domain system characterization under the superposition principle, by which the response of a linear system to mixed inputs is the sum of responses to individual inputs, we employ the Harmonic Balance method [183]. By HB, we decompose the response into its harmonics using FFT and sequential band-pass filtering with reference to the input frequency, then assess the input frequency to obtain an empirical transfer function estimate (ETFE), G, of AGeNT's mechanical dynamics filtered from harmonics due to nonlinearities [183]:

$$\begin{aligned} \hat{\tilde{G}}(e^{i\omega}) &\approx q(\omega) / \tau_{passive}(\omega)|_{\omega=0.10Hz,0.20Hz...2Hz} \\ \tau_{passive} &\approx \hat{\tilde{G}}^{-1} q|_{\omega=0.10Hz,0.20Hz...2Hz} \end{aligned} \tag{4.11}$$

We next validated AGeNT's performance as an HRI testbed. We utilized cursory human data from four male and one female aged 25-30 recruited to parameterize $E_{human}(t,q)$ for AGeNT Control per (4.8). Delsys sEMG electrodes were worn on the Flexor Digitorum Profundus, Flexor Pollicis Longus, Extensor Digitorum Communis, and Pronater Teres muscles (Fig 4.6). The participants performed a fine motor task while holding an instrumented bulb dynamometer as well as while wearing the CoTS hand exoskeleton on their dominant hand. This study was approved by Auburn University's Institutional Review Board (protocol #22-080 EP 2202).

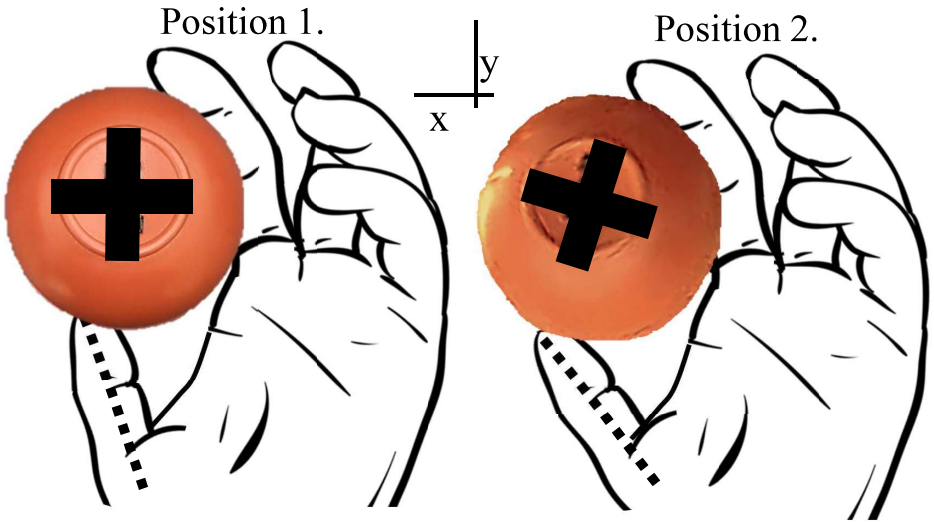

Figure 4.8: A fine motor task was developed to assess the capabilities of AGeNT to mimic human neuromechanical performance. Participants abducted and adducted the thumb CMC joint from position 1, to 2 and back to 1 to rotate a small red bulb dynamometer, the x and y position of which were recorded using a webcam. There was negligible displacement in the z axis. The fine motor task was repeated by human and AGeNT utilized to train the ESC policy to reduce neuromuscular effort, recorded from sEMG signals from the human, or as the internal EP-based control of AGeNT.

To validate AGeNT in training data-reference control policies, a simple but very fine motor task was developed in which participants held a spherical instrumented bulb dynamometer with negligible compliance between the thumb and index finger (Fig. 4.8). At position one, the thumb CMC joint is abducted to enable the finger tips to be co-linear and perpendicular with the ground plane. Then, at position two, the CMC is adducted resulting in a passive rotation of the bulb dynamometer. Single movements constitute starting at position 1, moving to 2 and back to 1. This motor skill is used during every day activities, like turning a key or using a spoon ($\hat{I}(t) = [1\,0\,0\,0\,0]^T$) [44].

The position of a small rectangular marker placed on the bulb dynamometer was recorded using a webcam, and the pressure in the bulb was logged throughout repetitions of the thumb CMC abduction/adduction movement. The movement was repeated once per second for 120 seconds across three trials by five human participants and the AGeNT platform while wearing the exoskeleton. In the first trial, the exoskeleton was not active at all. In the second trial, the ESC controller

was allowed to train using sEMG feedback from the human and using simulated sEMG signals (i.e., AGeNT's internal control signal). In the third trial, the ESC controller was implemented in its trained state.

Time- and frequency-domain models demonstrate that AGeNT accurately reproduces the passive and active dynamics of the hand (Fig. 4.9). The stiffness of a healthy human index MCP joint (gray line), experimental characterization of our prior passive instrumented hand [156] (light blue dots), AGeNT with no control (darker blue dots), and AGeNT with control (darkest blue dots) are shown. Solid lines are lines of best fit. AGeNT's passive stiffness was linear with $R^2 = 0.9$, and its active stiffness was exponential with $R^2 = 0.985$. The mean absolute percentage error between human MCP stiffness and active AGeNT MCP was 2.95%. The resulting exponential stiffness joint dynamics mean that AGeNT's control is able to accurately simulate human joint dynamics without significant high-order dynamic artifacts [40].

Time-frequency correlation, $\hat{G}^{-1}q \approx a \cdot e^{bq}$ validates the stiffness characteristics of the joint, and importantly, proves reliable, repeatable, time-invariant dynamics between the robot and human with negligible frequency-domain losses, without computationally expensive modeling [183]. Frequency-derived ETFE-based models of the active and passive stiffness of AGeNT are shown as dashed lines in Fig. 4.9. The ETFE results fit time-domain results with $R^2 = 0.985$ (active stiffness) and $R^2 = 0.875$ (passive stiffness), indicating stable dynamic performance of AGeNT across frequencies.

It was desired to demonstrate AGeNT's ability to track pre-recorded sEMG trajectories. $\hat{E}$ recorded during human un-assisted repetitions of the fine motor task were commanded to AGeNT. Tracking performance for one characteristic participant is visualized in Fig. 4.10 with 0.28% RMSE.

Next we quantify the performance of AGeNT during the fine motor task (Fig. 4.11). The max trajectory tracking error of the bulb dynamometer movement between AGeNT and human participants during the fine motor task in X and Y was 11% and 17.6% respectively (Fig. 4.11). Training of the adaptive gain and cumulative training loss for both cases are shown in Fig. 4.12.

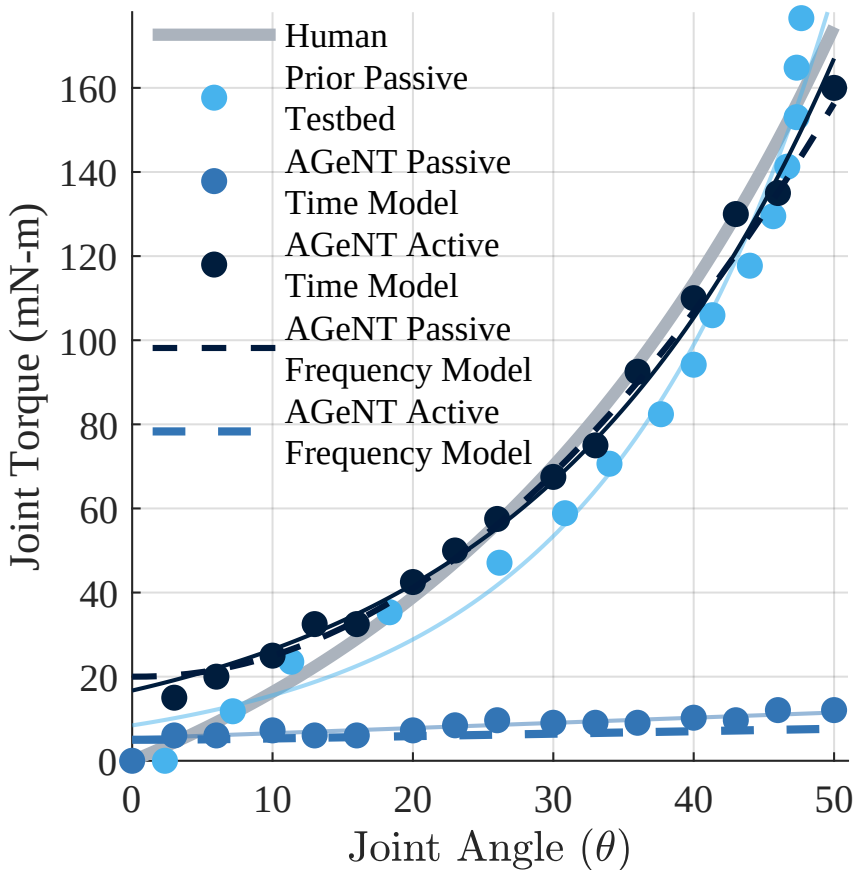

Figure 4.9: AGeNT accurately mimics the passive stiffness of human finger joints [156] with $R^2 = 0.985$. A variable sinusoidal load was applied to AGeNT's index finger by sweeping input frequencies (from 0.10 Hz to 2 Hz) through the hand exoskeleton. ETFE was extracted post-hoc, and correlated with 0 Hz data ($R^2 = 0.985$). This shows that the nonlinear biomechanical dynamics which dominate movement in human hands is well represented by AGeNT with high fidelity across the joint and frequency space.

The derivative of cumulative loss, which was the cumulative effort of the testbed (real human and AGeNT simulated $\hat{E}(t)$), diminished to indicate convergence to a stabilizing policy. Training with the human participant appears more dynamic because humans exhibit reflexive mechanical and tissue compression artifacts. The effort profile for one participant performing the movement with and without assistance are shown in Fig. 4.13.

The auto-normalized max and cumulative effort (loss) was found to be 88% and 86% less with robotic assistance respectively. The HRI effort profiles resulting from AGeNT- and human-trained ESC policies during the fine motor task were within one standard deviation (Fig. 4.13), indicating

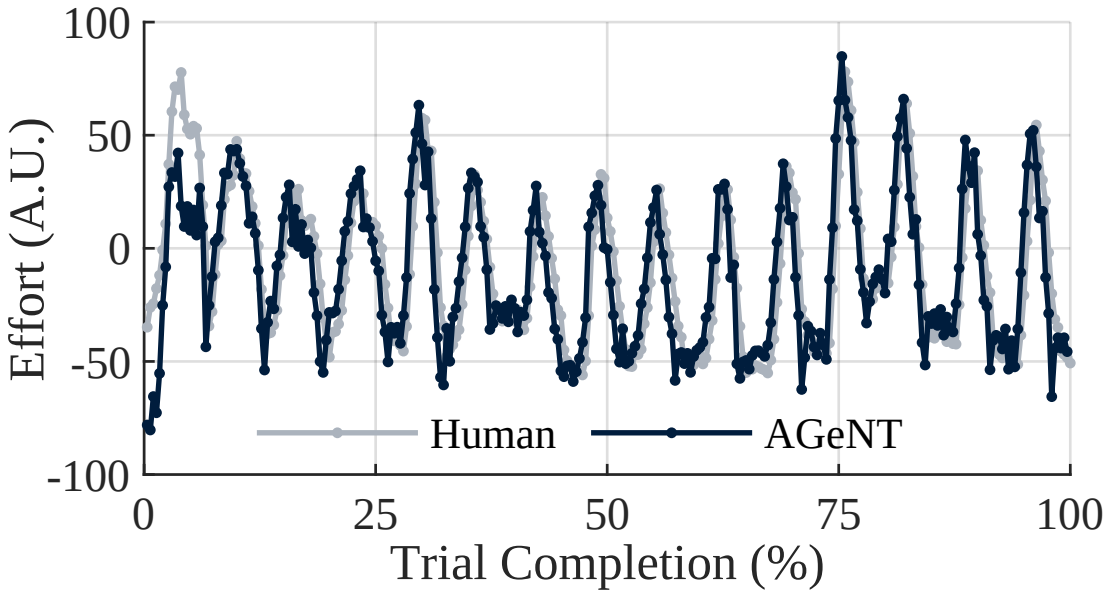

Figure 4.10: AGeNT is able to track the active effort dynamics of the human hand [1] with RMSE = 0.25%. Here human sEMG-based and AGeNT EP control-based effort are represented. The vertical axis is the inter-set min-max normalized effort amplitude, and the horizontal axis represents the progression of a 20 second trial recording of movement data.

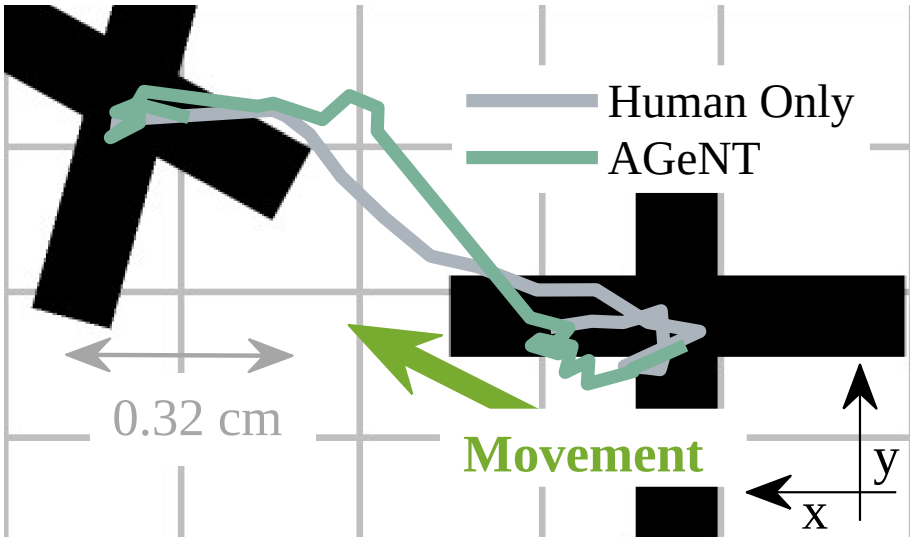

Figure 4.11: A fine motor task was designed to demonstrate AGeNT's neuromechanical representation of dexterous movement. During the task, participants adducted and abducted their thumb CMC joint to rotate a bulb dynamometer held between the thumb and index finger. AGeNT was commanded to repeat the same movement. The average movement trajectories are plotted above, along with a scale indicating 0.32 cm distance.The maximum tracking error of the bulb dynamometer between AGeNT and human participants during the fine motor task in X and Y was 11% and 17.6% respectively.

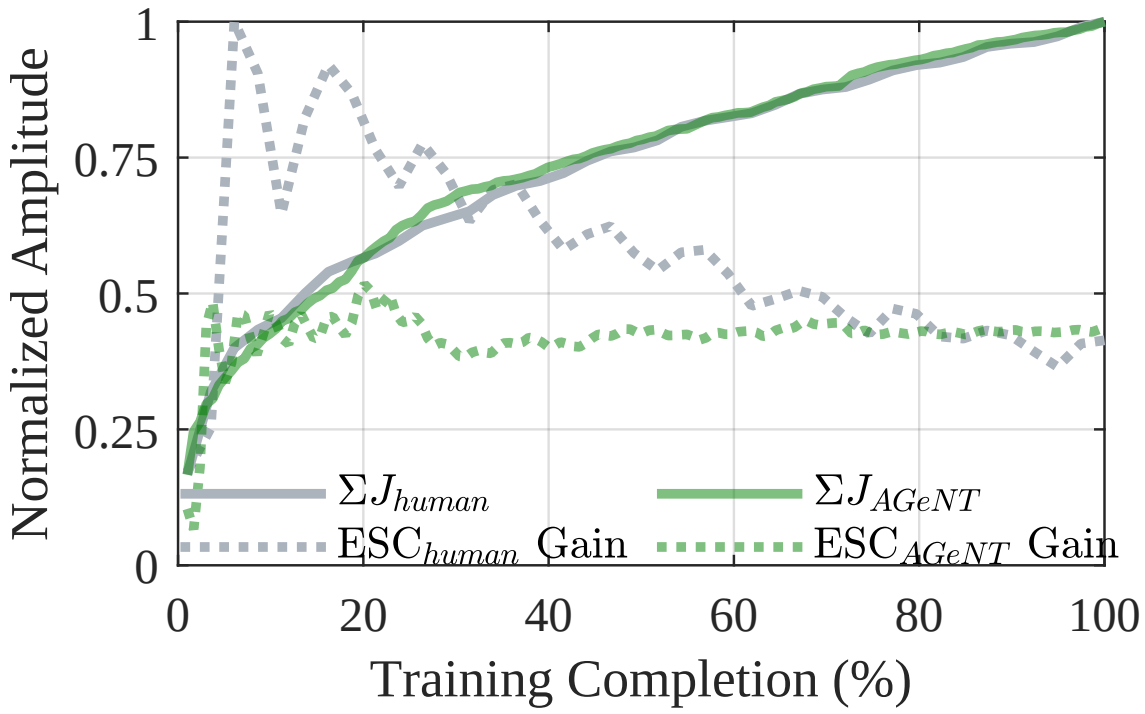

Figure 4.12: The ESC gain for the exoskeleton during training on the human (gray dotted) and on AGeNT (green dotted) are shown. The vertical axis represents the inter-set min-max normalized amplitude of the gain and cumulative loss and the horizontal axis represents progression of the 120 second trial. Training with the human participant is more dynamic because it is difficult for humans to move without reflex and tissue artifacts. The rate of the cumulative loss during training on the human (gray) and on AGeNT (green) decreases over the duration of training, indicating convergence.

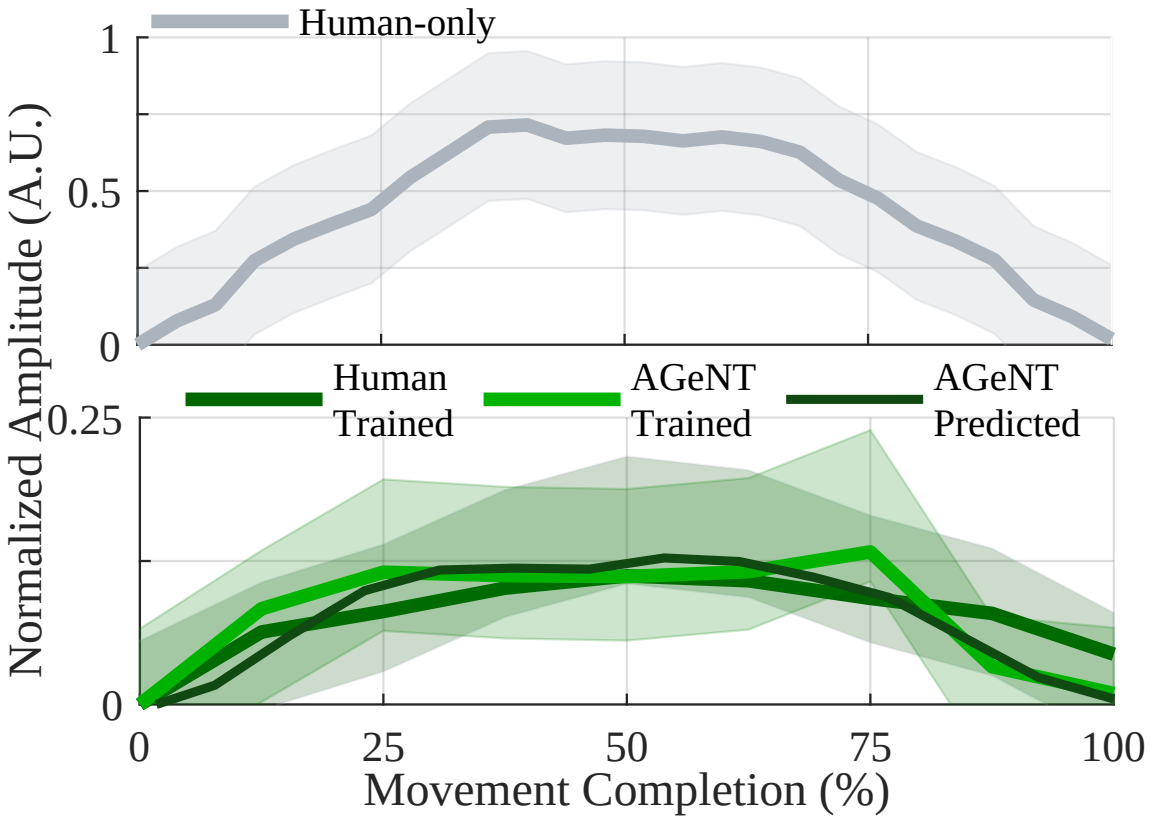

Figure 4.13: Resulting average sEMG-based effort profile for movement repetitions (i.e., abducting and adducting the thumb from position 1, to 2 and back to 1, representing 100% movement completion) of a characteristic human participant performing the motor task without assistance (gray plot) and with assistance by AGeNT (green plots) are shown. The vertical axis on both plots is min-max normalized effort. Human-trained and AGeNT-trained extremum seeking control yield reduction in neuromuscular effort when applied to the human by up to 80% compared to the human-only effort and are within 1 standard deviation of each other. AGeNT predicted profile - the effort of AGeNT with trained assistance - is within 1 standard deviation of the human effort profile, indicating its efficacy in mimicking neuromechanical response. The shaded regions are ± 1 standard deviation.

that AGeNT is competitive with human participants as a training platform. The effort profile of AGeNT after training was also within one standard deviation of the human-trained control performance, indicating that AGeNT can simulate unique neuromuscular responses to exoskeleton interventions.

In this study, we demonstrated the utility of AGeNT as a high-fidelity testbed that accurately mimics the passive and active dynamics of the human hand through validation against real human hand dynamics (Fig. 4.9) with 2.95% MAPE. We further demonstrate its ability to provide realistic, reliable, and repeatable control conditions for the development of data-reference soft exoskeleton control (Fig. 4.13). AGeNT matched human movement trajectories with maximum deviations less than 17% RMSE and effort trajectories within 1 standard deviation, yielding a model-free soft robot control policy that reduced human effort by up to 90%. AGeNT reduces human participant testing for validation for faster, more effective exoskeleton research.

However, while the testbed captured the biomechanical behavior under study, it neglected to incorporate full-hand dynamics including wrist and tissue dynamics, and inter-limb interactions in complex tasks. Furthermore, the ESC control strategy is only a basis for future work with more advanced machine learning techniques that could offer greater optimization and adaptability in handling HRI. We utilized ETFE to validate the linearity and reliability of joint stiffness across the frequency space. However ETFE is discrete in the frequency domain, largely valid with respect only to frequencies that are tested the system. ETFE is only valid for the tested frequencies and is a non-parametric estimate of the system model, which fails to capture critical information like actuator bandwidth corresponding to reachable sets.

Our future efforts will focus on expanding the capabilities of AGeNT to encompass more comprehensive models of human motor function including additional finger and wrist joints, somatosensory processing, and intrinsic tissue compliance. Further, we will evaluate more diverse data-driven control strategies including reinforcement and generative learning control which could adapt to time-variable phenomena like muscle fatigue. Lastly, these results motivate the extension of this approach to other joints and limbs.

This chapter presented a computational and physical embodiment as a first step to achieving scalable human-robot interaction experiments using elements of the computational neuromechanical suites. Elements including neuromechanical modeling, and estimation and forecasting of state transition dynamics control are yet to be fully captilized without functional embodiments that support high-fidelity multifaceted and longitudinal interaction studies .

Chapter 5

Conclusion

5.1 Summary and Contributions

This dissertation introduces a suite of computational neuromechanical tools—NeuroSiGHT, NeuroMERGE, and NeuroGAIN—designed to address the critical challenge of modeling, estimating, and controlling dynamic neuromechanical states at the human hand. These tools collectively represent a fundamental shift toward understanding neuromechanical interactions not as static, isolated kinematic configurations, but as complex, time-evolving states shaped by the interplay of muscle activity, sensorimotor feedback, cognitive load, and learning dynamics. Motivated by the practical limitations of conventional hand-assistive robotics—often restricted to stationary neuromechanical conditions—this body of work proposes computationally efficient, data-driven solutions that preserve robustness under real-world, nonstationary conditions such as fatigue, adaptation, and variable user intent.

Building upon the need for computationally tractable neuromuscular estimation, this work introduced a low-dimensional linear neuromuscular estimator that outperforms traditional classifiers by capturing underlying synergy dynamics while minimizing computational overhead. This approach bridges the gap between linear estimation, which often neglects dynamic coordination patterns, and nonlinear models that demand significant time-frequency computation. This estimator lays the foundation for real-time implementation in wearable robotics and holds promise for deployment in populations with neuromuscular disabilities, where disease-specific synergy patterns require adaptive control strategies.

To address the challenges of learning and control in unstable environments, this dissertation introduced NeuroMERGE, a model-free reinforcement learning framework integrating neuromuscular theory, Bayesian inference, and constrained optimization. NeuroMERGE enables adaptive

exploration of dynamic state spaces while maintaining safety and interpretability. It achieves this by employing a feedback structure grounded in muscle synergy models, allowing assistive systems to safely and autonomously identify the underlying structure of a user's neuromechanical state transitions. The methodology demonstrates both efficiency and safety improvements over traditional reinforcement learning techniques and can be readily tuned to operate more conservatively or aggressively depending on the application context.

NeuroGAIN further advances these ideas by integrating a generative forecasting framework with model predictive control (MPC). It leverages a combination of Non-negative Matrix Tri-Factorization (NM3F) and LSTM-based Variational Autoencoders (LSTM-VAE) to predict neuromechanical demands from sEMG data. This enables exoskeletons and assistive interfaces to dynamically anticipate user needs, providing a personalized and responsive control experience. NeuroGAIN-MPC demonstrates significant improvements in both simulation and human-subject experiments, validating its ability to deliver individualized assistance while preserving computational efficiency. The result is a system capable of supporting high-frequency, real-time control that adapts to user-specific dynamics without requiring extensive recalibration.

Finally, NeuroSiGHT combines elements of all previous models into a unified simulation framework for motor skill acquisition driven by haptic feedback. By modeling sensorimotor control as a partially observable Markov decision process (POMDP), and warm-starting policy optimization using structured neuromechanical priors, NeuroSiGHT enables faster convergence and greater precision in high-dimensional motor tasks. Empirical validation shows a substantial improvement in learning accuracy and efficiency, suggesting that embedding structured priors into reinforcement learning frameworks can drastically enhance the effectiveness of haptic guidance protocols. The open-source release of this framework fosters future research into scalable, generalizable training systems for surgical skill acquisition, physical rehabilitation, and cognitive HRI applications.

5.2 Future Directions

The models and methods introduced in this dissertation open several avenues for future research. A critical next step involves translating these tools into clinical and field settings where nonstationary neuromechanical dynamics—such as those introduced by fatigue, recovery, and training—must be handled in real-time. This includes adapting NeuroMERGE and NeuroGAIN for use with diverse clinical populations, including individuals recovering from stroke, spinal cord injury, or degenerative neuromuscular diseases. Clinical translation will also require closer integration with wearable hardware, refinement of user calibration protocols, and the development of interpretable feedback systems for both users and clinicians.

Moreover, as the field of computational neuromechanics evolves, there is increasing value in fusing data across sensing modalities—e.g., sEMG, RT, inertial measurements, and neural recordings—to construct multi-scale models of human motor behavior. These hybrid systems could provide more complete state estimates and enable more nuanced interpretations of user intent and capability. Extending the current frameworks to incorporate probabilistic graphical models, Bayesian filters, or neural ODEs could further enhance adaptability and resilience to uncertainty in sensing or actuation.

There is also strong potential for collaboration between engineers, clinicians, and cognitive scientists to define standard neuromechanical benchmarks and publicly available datasets that support reproducibility and fair comparison across modeling methods. Future work should prioritize robust benchmarking practices and community-driven tool development, particularly for applications in telemedicine, point-of-care diagnostics, and at-home rehabilitation.

5.3 Conclusion

Together, the methods presented in this dissertation form a cohesive framework for understanding and improving human–robot interaction at the neuromechanical level. They demonstrate how structured modeling, adaptive control, and machine learning can converge to support robust,

personalized, and scalable hand-assistive technologies. Whether applied to clinical diagnosis, rehabilitation after neurological injury, or the development of dexterous training systems, these contributions lay the groundwork for a future where neuromechanical models are not only computationally feasible but also clinically impactful and accessible. By advancing both the science and engineering of neuromechanics, this work contributes meaningfully to the broader goal of enabling intelligent, human-centered robotics in complex, real-world environments.

Bibliography

[1] A. Baskaran, D. S. Hollinger, R. O. Hailey, M. E. Zabala, and C. G. Rose. "Neuromuscular State Estimation Via Space-by-Time Neural Signal Decomposition1". In: *ASME Letters in Dynamic Systems and Control* 3.4 (Dec. 2023), p. 041005. ISSN: 2689-6117. DOI: doi.org/10.1115/1.4064069.

[2] A. Baskaran, R. D. Hoehn, and C. G. Rose. "Neuromechanical Models of Mild Traumatic Brain Injury Conditioned on Reaction Time: A Systematic Review and Meta-Analysis". In: *Journal of Clinical Medicine* 13.24 (2024). ISSN: 2077-0383. DOI: doi.org/10.3390/jcm13247648.

[3] A. Baskaran, S. Basyal, B. C. Allen, and C. G. Rose. "Neuromechanical Generative Model-Predictive Control of a Soft Hand Exoskeleton for Assistance in Functional Tasks". In: *Journal of Medical Robotics Research* (2025). In Press.

[4] A. Baskaran, S. Basyal, B. C. Allen, and C. G. Rose. "NeuroGAIN: Neuromechanical Generative Demand Forecasting Toward Optimal Control of Soft Hand Exoskeletons". In: *2024 International Symposium on Medical Robotics (ISMR)*. 2024, pp. 1–6. DOI: doi.org/10.1109/ISMR63436.2024.10585782.

[5] A. Baskaran, S. Basyal, B. C. Allen, and C. G. Rose. "Neuromechanical Model-free Epistemic Risk Guided Exploration (NeuroMERGE) for Safe Autonomy in Human-Robot Interaction". In: *2024 American Control Conference (ACC)*. 2024, pp. 4518–4523. DOI: doi.org/10.23919/ACC60939.2024.10644395.

[6] A. Baskaran and C. G. Rose. "Assessment of Neuromuscular Fatigue from Muscle Synergies in Hand Poses". In: *IFAC-PapersOnLine*. Vol. 55. Elsevier B.V., 2022, pp. 382–387. DOI: doi.org/10.1016/j.ifacol.2022.11.213.

[7] E. B. Quinlan, L. Dodakian, J. See, A. McKenzie, V. Le, M. Wojnowicz, B. Shahbaba, and S. C. Cramer. “Neural function, injury, and stroke subtype predict treatment gains after stroke”. In: *Annals of neurology* 77.1 (2015), pp. 132–145. DOI: doi.org/10.1002/ana.24309.

[8] M. Solomonow. “Sensory–motor control of ligaments and associated neuromuscular disorders”. In: *Journal of Electromyography and Kinesiology* 16.6 (2006), pp. 549–567. DOI: doi.org/10.1016/j.jelekin.2006.08.004.

[9] C. Liu, J. Lu, H. Yang, and K. Guo. “Current State of Robotics in Hand Rehabilitation after Stroke: A Systematic Review”. In: *Applied Sciences (Switzerland)* 12 (9 May 2022). ISSN: 20763417. DOI: doi.org/10.3390/app12094540.

[10] F. Porciuncula, A. V. Roto, D. Kumar, I. Davis, S. Roy, C. J. Walsh, and L. N. Awad. “Wearable Movement Sensors for Rehabilitation: A Focused Review of Technological and Clinical Advances”. In: *PM and R* 10 (9 Sept. 2018), S220–S232. ISSN: 19341482. DOI: doi.org/10.1016/j.pmrj.2018.06.013.

[11] S. E. Fasoli, H. I. Krebs, and N. Hogan. “Robotic technology and stroke rehabilitation: Translating research into practice”. In: *Topics in Stroke Rehabilitation* 11 (4 Sept. 2004), pp. 11–19. ISSN: 10749357. DOI: doi.org/10.1310/G8XB-VM23-1TK7-PWQU.

[12] P. Tran, S. Jeong, K. R. Herrin, and J. P. Desai. “Review: Hand Exoskeleton Systems, Clinical Rehabilitation Practices, and Future Prospects”. In: *IEEE Transactions on Medical Robotics and Bionics* 3 (3 Aug. 2021), pp. 606–622. ISSN: 25763202. DOI: doi.org/10.1109/TMRB.2021.3100625.

[13] A. M. Okamura. “Haptic feedback in robot-assisted minimally invasive surgery”. In: *Current Opinion in Urology* 19 (1 Jan. 2009), pp. 102–107. ISSN: 09630643. DOI: doi.org/10.1097/MOU.0b013e32831a478c.

[14] D. F. Pepley, A. B. Gordon, M. A. Yovanoff, K. A. Mirkin, S. R. Miller, D. C. Han, and J. Z. Moore. "Training Surgical Residents With a Haptic Robotic Central Venous Catheterization Simulator". In: *Journal of Surgical Education* 74 (6 Nov. 2017), pp. 1066–1073. ISSN: 18787452. DOI: doi.org/10.1016/j.jsurg.2017.06.003.

[15] S. S. Kantak and C. J. Winstein. "Learning-performance distinction and memory processes for motor skills: A focused review and perspective". In: *Behavioural Brain Research* 228 (1 Mar. 2012), pp. 219–231. ISSN: 01664328. DOI: doi.org/10.1016/j.bbr.2011.11.028.

[16] M. Ison, I. Vujaklija, B. Whitsell, D. Farina, and P. Artemiadis. "High-Density Electromyography and Motor Skill Learning for Robust Long-Term Control of a 7-DoF Robot Arm". In: *IEEE Transactions on Neural Systems and Rehabilitation Engineering* 24 (4 Apr. 2016), pp. 424–433. ISSN: 15344320. DOI: doi.org/10.1109/TNSRE.2015.2417775.

[17] L. A. Jones and S. J. Lederman. *Human Hand Function*. New York: Oxford University Press, 2006. ISBN: 9780195173154. URL: global.oup.com/academic/product/human-hand-function-9780195173154.

[18] C. Pacchierotti, S. Sinclair, M. Solazzi, A. Frisoli, V. Hayward, and D. Prattichizzo. "Wearable haptic systems for the fingertip and the hand: Taxonomy, review, and perspectives". In: *IEEE Transactions on Haptics* 10 (4 2017), pp. 580–600. ISSN: 23294051. DOI: doi.org/10.1109/TOH.2017.2689006.

[19] M. Kalakrishnan, P. Pastor, L. Righetti, and S. Schaal. "Learning objective functions for manipulation". In: *2013 IEEE International Conference on Robotics and Automation*. 2013, pp. 1331–1336. DOI: doi.org/10.1109/ICRA.2013.6630743.

[20] K. Ghonasgi, R. Mirsky, S. Narvekar, B. Masetty, A. M. Haith, P. Stone, and A. D. Deshpande. "Capturing Skill State in Curriculum Learning for Human Skill Acquisition". In: *IEEE International Conference on Intelligent Robots and Systems*. Institute of Electrical

and Electronics Engineers Inc., 2021, pp. 771–776. ISBN: 9781665417143. DOI: doi.org/10.1109/IROS51168.2021.9636850.

[21] M. R. Senesh and D. J. Reinkensmeyer. "Breaking Proportional Recovery After Stroke". In: *Neurorehabilitation and Neural Repair* 33 (11 Nov. 2019), pp. 888–901. ISSN: 15526844. DOI: doi.org/10.1177/1545968319868718.

[22] R. A. Schmidt and R. A. Bjork. "New Conceptualizations of Practice: Common Principles in Three Paradigms Suggest New Concepts for Training". In: *Psychological Science* 3 (4 1992), pp. 207–217. ISSN: 14679280. DOI: doi.org/10.1111/j.1467-9280.1992.tb00029.x.

[23] K. Nishikawa, A. A. Biewener, P. Aerts, A. N. Ahn, H. J. Chiel, M. A. Daley, T. L. Daniel, R. J. Full, M. E. Hale, T. L. Hedrick, A. K. Lappin, T. R. Nichols, R. D. Quinn, R. A. Satterlie, and B. Szymik. "Neuromechanics: An integrative approach for understanding motor control". In: *Integrative and Comparative Biology* 47 (1 July 2007), pp. 16–54. ISSN: 15407063. DOI: doi.org/10.1093/icb/icm024.

[24] F. Garro, M. Chiappalone, S. Buccelli, L. D. Michieli, and M. Semprini. "Neuromechanical Biomarkers for Robotic Neurorehabilitation". In: *Frontiers in Neurorobotics* 15 (Oct. 2021). ISSN: 16625218. DOI: doi.org/10.3389/fnbot.2021.742163.

[25] G. Torres-Oviedo and L. H. Ting. "Subject-specific muscle synergies in human balance control are consistent across different biomechanical contexts". In: *Journal of Neurophysiology* 103 (6 June 2010), pp. 3084–3098. ISSN: 00223077. DOI: doi.org/10.1152/jn.00960.2009.

[26] A. Prochazka and S. Yakovenko. "The neuromechanical tuning hypothesis". In: *Progress in brain research* 165 (2007), pp. 255–265. DOI: doi.org/10.1016/S0079-6123(06)65016-4.

[27] E. Todorov and M. I. Jordan. “Optimal feedback control as a theory of motor coordination”. In: *Nature Neuroscience* 5 (11 2002), pp. 1226–1235. ISSN: 10976256. DOI: doi.org/10.1038/nn963.

[28] M. Hamaya, T. Matsubara, T. Teramae, T. Noda, and J. Morimoto. “Design of physical user–robot interactions for model identification of soft actuators on exoskeleton robots”. In: *International Journal of Robotics Research* 40 (1 Jan. 2021), pp. 397–410. ISSN: 17413176. DOI: doi.org/10.1177/0278364919853618.

[29] D. Leonardis, M. Barsotti, C. Loconsole, M. Solazzi, M. Troncossi, C. Mazzotti, V. P. Castelli, C. Procopio, G. Lamola, C. Chisari, M. Bergamasco, and A. Frisoli. “An EMG-controlled robotic hand exoskeleton for bilateral rehabilitation”. In: *IEEE Transactions on Haptics* 8 (2 Apr. 2015), pp. 140–151. ISSN: 19391412. DOI: doi.org/10.1109/TOH.2015.2417570.

[30] P. Gómez-Vilda, A. Gómez-Rodellar, J. M. Vicente, J. Mekyska, D. Palacios-Alonso, V. Rodellar-Biarge, A. Álvarez-Marquina, I. Eliasova, M. Kostalova, and I. Rektorova. “Neuromechanical Modelling of Articulatory Movements from Surface Electromyography and Speech Formants”. In: *International Journal of Neural Systems*. Vol. 29. World Scientific Publishing Co. Pte Ltd, Mar. 2019. DOI: doi.org/10.1142/S0129065718500399.

[31] I. Delis, P. M. Hilt, T. Pozzo, S. Panzeri, and B. Berret. “Deciphering the functional role of spatial and temporal muscle synergies in whole-body movements”. In: *Scientific Reports* 8 (1 2018). ISSN: 20452322. DOI: doi.org/10.1038/s41598-018-26780-z.

[32] D. C. McFarland, B. I. Binder-Markey, J. A. Nichols, S. J. Wohlman, M. De Bruin, and W. M. Murray. “A musculoskeletal model of the hand and wrist capable of simulating functional tasks”. In: *IEEE transactions on biomedical engineering* 70.5 (2022), pp. 1424–1435. DOI: doi.org/10.1109/TBME.2022.3217722.

[33] M. Kawato. “Internal models for motor control and trajectory planning”. In: *Current Opinion in Neurobiology* 9.6 (1999), pp. 718–727. ISSN: 0959-4388. DOI: doi.org/10.1016/S0959-4388(99)00028-8.

[34] J. R. Anderson. “ACT-R: A theory of higher level cognition and its relation to visual attention”. In: *Human-Computer Interaction* 12 (4 1997), pp. 439–462. ISSN: 07370024. DOI: doi.org/10.1207/s15327051hci1204_5.

[35] A. A. Frolov, D. Húsek, E. V. Biryukova, P. D. Bobrov, O. A. Mokienko, and A. V. Alexandrov. “Principles of motor recovery in post-stroke patients using hand exoskeleton controlled by the brain-computer interface based on motor imagery”. In: *Neural Network World* 27 (1 Jan. 2017), pp. 107–137. ISSN: 12100552. DOI: doi.org/10.14311/NNW.2017.27.006.

[36] E. Bizzi, N. Hogan, F. A. Mussa-Ivaldi, and S. Giszter. “Does the nervous system use equilibrium-point control to guide single and multiple joint movements?” In: *Behavioral and Brain Sciences* 15 (04 Dec. 1992), pp. 603–613. ISSN: 0140-525X. DOI: doi.org/10.1017/s0140525x00072538.

[37] K. Uno, T. Oku, P. Phatiwuttipat, K. Koba, Y. Yamashita, K. Murakami, M. Uemura, H. Hirai, and F. Miyazaki. “A novel muscle synergy extraction method to explain the equilibrium-point trajectory and endpoint stiffness during human upper-limb movements on a horizontal plane”. In: *5th IEEE RAS/EMBS International Conference on Biomedical Robotics and Biomechatronics*. IEEE. 2014, pp. 621–626. DOI: doi.org/10.1109/BIOROB.2014.6913847.

[38] J. Massion, V. Gurfinkel, M. Lipshits, A. Obadia, and K. Popov. “Strategy and synergy: two levels of equilibrium control during movement. Effects of the microgravity”. In: *Comptes rendus de l’Académie des sciences. Série III, Sciences de la vie* 314.2 (1992), pp. 87–92. URL: pubmed.ncbi.nlm.nih.gov/1559185/.

[39] F. Hug, C. Goupille, D. Baum, B. J. Raiteri, P. W. Hodges, and K. Tucker. "Nature of the coupling between neural drive and force-generating capacity in the human quadriceps muscle". In: *Proceedings of the Royal Society B: Biological Sciences* 282 (1819 Nov. 2015). ISSN: 14712954. DOI: doi.org/10.1098/rspb.2015.1908.

[40] A. D. Deshpande, N. Gialias, and Y. Matsuoka. "Contributions of intrinsic visco-elastic torques during planar index finger and wrist movements". In: *IEEE Transactions on Biomedical Engineering* 59 (2 Feb. 2012), pp. 586–594. ISSN: 00189294. DOI: doi.org/10.1109/TBME.2011.2178240.

[41] S. A. Winges. "Somatosensory feedback refines the perception of hand shape with respect to external constraints". In: *Neuroscience* 293 (May 2015), pp. 1–11. ISSN: 18737544. DOI: doi.org/10.1016/j.neuroscience.2015.02.047.

[42] K. J. Cole and J. H. Abbs. "Coordination of three-joint digit movements for rapid finger-thumb grasp". In: *Journal of neurophysiology* 55.6 (1986), pp. 1407–1423. DOI: doi.org/10.1152/jn.1986.55.6.1407.

[43] V. S. Huang and J. W. Krakauer. "Robotic neurorehabilitation: A computational motor learning perspective". In: *Journal of NeuroEngineering and Rehabilitation* 6 (1 2009). ISSN: 17430003. DOI: doi.org/10.1186/1743-0003-6-5.

[44] T. D. Niehues and A. D. Deshpande. "Human-inspired object manipulation control with the anatomically correct testbed hand". In: *2018 IEEE International Conference on Robotics and Automation (ICRA)*. IEEE. 2018, pp. 6861–6866. DOI: doi.org/10.1109/ICRA.2018.8463166.

[45] B. T. Volpe, H. I. Krebs, N. Hogan, L. Edelstein, C. Diels, and M. Aisen. "A novel approach to stroke rehabilitation: Robot-aided sensorimotor stimulation". In: *Neurology* 54 (10 May 2000), pp. 1938–1944. ISSN: 00283878. DOI: doi.org/10.1212/WNL.54.10.1938.

[46] K. Ghonasgi, R. Mirsky, A. M. Haith, P. Stone, and A. D. Deshpande. “Quantifying Changes in Kinematic Behavior of a Human-Exoskeleton Interactive System”. In: *2022 IEEE/RSJ International Conference on Intelligent Robots and Systems (IROS)*. 2022, pp. 10734–10739. DOI: doi.org/10.1109/IROS47612.2022.9981032.

[47] A. D’Avella, P. Saltiel, and E. Bizzi. “Combinations of muscle synergies in the construction of a natural motor behavior”. In: *Nature Neuroscience* 6 (3 Mar. 2003), pp. 300–308. ISSN: 10976256. DOI: doi.org/10.1038/nn1010.

[48] E. P. Gardner and K. O. Johnson. *The Somatosensory System: Receptors and central pathways*. Ed. by E. R. Kandel, J. H. Schwartz, T. M. Jessell, S. A. Siegelbaum, and A. J. Hudspeth. 5th ed. McGraw-Hill Education, 2012. ISBN: 978-0-07-139011-8.

[49] M. Santello, M. Flanders, and J. F. Soechting. “Postural hand synergies for tool use”. In: *Journal of neuroscience* 18.23 (1998), pp. 10105–10115. DOI: doi.org/10.1523/JNEUROSCI.18-23-10105.1998.

[50] D. Nguyen-Tuong and J. Peters. “Model learning for robot control: A survey”. In: *Cognitive Processing* 12 (4 Nov. 2011), pp. 319–340. ISSN: 16124782. DOI: doi.org/10.1007/s10339-011-0404-1.

[51] L. Rier, R. Zamyadi, J. Zhang, Z. Emami, Z. A. Seedat, S. Mocanu, L. E. Gascoyne, C. M. Allen, J. W. Scadding, P. L. Fopturlong, G. Gooding-Williams, M. W. Woolrich, N. Evangelou, M. J. Brookes, and B. T. Dunkley. “Mild Traumatic Brain Injury Impairs the Coordination of Intrinsic and Motor-Related Neural Dynamics”. In: *NeuroImage: Clinical* 32 (2021). DOI: doi.org/10.1016/j.nicl.2021.102841.

[52] D. Dumphy. “The Effect of Mild Traumatic Brain Injury on Reaction Time, Dual-tasking Reaction Time and Heart Rate Variability in Driving Simulation”. In: (2015). URL: http://knowledgecommons.lakeheadu.ca/handle/2453/784.

[53] C. I. Halterman, J. Langan, A. Drew, E. Rodriguez, L. R. Osternig, L. S. Chou, and P. V. Donkelaar. “Tracking the Recovery of Visuospatial Attention Deficits in Mild Traumatic

Brain Injury". In: *Brain* 129 (3 2006), pp. 747–753. DOI: doi.org/10.1093/brain/awh705.

[54] B. L. Brooks, H. Daya, S. Khan, H. L. Carlson, A. Mikrogianakis, and K. M. Barlow. "Cognition in the Emergency Department as a Predictor of Recovery after Pediatric Mild Traumatic Brain Injury". In: *Journal of the International Neuropsychological Society* 22 (4 2016), pp. 379–387. DOI: doi:10.1017/S1355617715001368.

[55] A. P. Kontos, R. S. Kotwal, R. J. Elbin, R. H. Lutz, R. D. Forsten, P. J. Benson, and K. M. Guskiewicz. "Residual Effects of Combat-Related Mild Traumatic Brain Injury". In: *Journal of Neurotrauma* 30 (8 2013), pp. 680–686. DOI: doi.org/10.1089/neu.2012.2506.

[56] K. A. Frencham, A. M. Fox, and M. T. Maybery. "Neuropsychological Studies of Mild Traumatic Brain Injury: A Meta-Analytic Review of Research Since 1995". In: *Journal of Clinical and Experimental Neuropsychology* 27 (2005), pp. 334–351. DOI: doi.org/10.1080/13803390490520328.

[57] S. Gazzellini, A. Napolitano, G. Bauleo, E. Bisozzi, M. L. Lispi, E. Ardu, E. Castelli, and F. Benso. "Time–Frequency Analyses of Reaction Times and Theta/Beta EEG Ratio in Pediatric Patients with Traumatic Brain Injury: A Preliminary Study". In: *Developmental Neurorehabilitation* 20 (7 2017), pp. 393–407. DOI: doi.org/10.1080/17518423.2016.1216470.

[58] P. J. A. Dean, J. R. Sato, G. Vieira, A. McNamara, and A. Sterr. "Multimodal Imaging of Mild Traumatic Brain Injury and Persistent Postconcussion Syndrome". In: *Brain and Behavior* 5 (1 2015), pp. 45–61. DOI: doi.org/10.1002/brb3.292.

[59] C. N. Feller, M. Goldenberg, P. D. Asselin, K. Merchant-Borna, B. Abar, C. M. C. Jones, R. Mannix, K. Kawata, and J. J. Bazarian. "Classification of Comprehensive Neuro- Ophthalmologic Measures of Postacute Concussion". In: *JAMA Network Open* 4 (2021). DOI: doi.org/10.1001/jamanetworkopen.2021.0599.

[60] M. B. Pontifex, P. M. O'Connor, S. P. Broglio, and C. H. Hillman. "The Association Between Mild Traumatic Brain Injury History and Cognitive Control". In: *Neuropsychologia* 47 (2009), pp. 3210–3216. DOI: doi.org/10.1016/j.neuropsychologia.2009.07.021.

[61] A. J. Pearce, D. J. Kidgell, A. K. Frazer, D. A. King, M. E. Buckland, and M. Tommerdahl. "Corticomotor Correlates of Somatosensory Reaction Time and Variability in Individuals with Post Concussion Symptoms". In: *Somatosensory and Motor Research* 37 (1 2020), pp. 14–21. DOI: doi.org/10.1080/08990220.2019.1699045.

[62] T. D. Fischer, S. D. Red, A. Z. Chuang, E. B. Jones, J. J. McCarthy, S. S. Patel, and A. B. Sereno. "Detection of Subtle Cognitive Changes After mTBI Using a Novel Tablet-Based Task". In: *Journal of Neurotrauma* 33 (13 2016), pp. 1237–1246. DOI: doi.org/10.1089/neu.2015.3990.

[63] D. S. DeWitt, R. Perez-Polo, C. E. Hulsebosch, P. K. Dash, and C. S. Robertson. "Challenges in the Development of Rodent Models of Mild Traumatic Brain Injury". In: *Journal of Neurotrauma* 30 (9 2013), pp. 688–701. DOI: doi.org/10.1089/neu.2012.2349.

[64] G. K. Henry. "Response Time Measures on the Word Memory Test Do Not Add Incremental Validity to Accuracy Scores in Predicting Noncredible Neurocognitive Dysfunction in Mild Traumatic Brain Injury Litigants". In: *Applied Neuropsychology: Adult* (2022). DOI: doi.org/10.1080/23279095.2022.2126320.

[65] C. Karton, T. Blaine Hoshizaki, and M. D. Gilchrist. "A novel repetitive head impact exposure measurement tool differentiates player position in National Football League". In: *Scientific reports* 10.1 (2020), p. 1200. DOI: doi.org/10.1038/s41598-019-54874-9.

[66] H. Arciniega, J. Shires, S. Fopturlong, A. Kilgore-Gomez, A. Cerreta, N. G. Murray, and M. E. Berryhill. “Impaired Visual Working Memory and Reduced Connectivity in Undergraduates with a History of Mild Traumatic Brain Injury”. In: *Scientific Reports* 11 (2021). DOI: doi.org/10.1038/s41598-021-80995-1.

[67] J. B. Caccese, J. T. Eckner, L. Franco-MacKendrick, J. B. Hazzard, M. Ni, S. P. Broglio, T. W. McAllister, M. McCrea, and T. A. Buckley. “Clinical Reaction-Time Performance Factors in Healthy Collegiate Athletes”. In: *Journal of Athletic Training* 55 (6 2020), pp. 601–607. DOI: doi.org/10.4085/1062-6050-164-19.

[68] C. Adams, P. Bazzigaluppi, T. L. Beckett, J. Bishay, I. Weisspapir, A. Dorr, J. R. Mester, J. Steinman, L. Hirschler, J. M. Warnking, et al. “Neurogliovascular dysfunction in a model of repeated traumatic brain injury”. In: *Theranostics* 8.17 (2018), p. 4824. DOI: doi.org/10.7150/thno.24747.

[69] J. Cui, L. J. Ng, and V. Volman. “Callosal Injury-Induced Working Memory Impairment: A Computational Network Modeling Study”. In: *NeuroReport* 28 (14 2017), pp. 865–871. DOI: doi.org/10.1097/wnr.0000000000000842.

[70] A. R. Mayer, M. V. Mannell, J. Ling, R. Elgie, C. Gasparovic, J. P. Phillips, D. Doezema, and R. A. Yeo. “Auditory Orienting and Inhibition of Return in Mild Traumatic Brain Injury: A FMRI Study”. In: *Human Brain Mapping* 30 (12 2009), pp. 4152–4166. DOI: doi.org/10.1002/hbm.20836.

[71] J. Cui, L. J. Ng, and V. Volman. “Callosal Dysfunction Explains Injury Sequelae in a Computational Network Model of Axonal Injury”. In: *Journal of Neurophysiology* 116 (2016), pp. 2892–2908. DOI: doi.org/10.1152/jn.00603.2016.

[72] J. A. Gould, K. J. Ciuffreda, N. K. Yadav, P. Thiagarajan, and B. Arthur. “The Effect of Retinal Defocus on Simple Eye-Hand and Eye-Foot Reaction Time in Traumatic Brain Injury (TBI)”. In: *Brain Injury* 27 (2013), pp. 1643–1648. DOI: doi.org/10.3109/02699052.2013.831124.

[73] J. Q. Truong and K. J. Ciuffreda. "Comparison of Pupillary Dynamics to Light in the Mild Traumatic Brain Injury and Normal Populations". In: *Brain Injury* 30 (11 2016), pp. 1378–1389. DOI: doi.org/10.1080/02699052.2016.1195922.

[74] P. J. Dean and A. Sterr. "Long-term effects of mild traumatic brain injury on cognitive performance". In: *Frontiers in Human Neuroscience* 7 (2013). ISSN: 1662-5161. DOI: doi.org/10.3389/fnhum.2013.00030.

[75] J. Maruta, J. Tong, S. W. Lee, Z. Iqbal, A. Schonberger, and J. Ghajar. "EYE-TRAC: monitoring attention and utility for mTBI". In: 8371 (2012). Ed. by S. O. Southern, A. H. J. Kolk, K. N. Montgomery, C. W. Taylor, B. V. K. V. Kumar, S. Prabhakar, and A. A. Ross, p. 83710L. DOI: doi.org/10.1117/12.927790.

[76] F. Yu, D. K. Shukla, R. C. Armstrong, C. M. Marion, K. L. Radomski, R. G. Selwyn, and B. J. Dardzinski. "Repetitive Model of Mild Traumatic Brain Injury Produces Cortical Abnormalities Detectable by Magnetic Resonance Diffusion Imaging, Histopathology, and Behavior". In: *Journal of Neurotrauma* 34 (7 2017), pp. 1364–1381. DOI: doi.org/10.1089/neu.2016.4569.

[77] F. Hussain and S. Wood. "Computational Modelling of Deficits in Attentional Networks in Mild Traumatic Brain Injury: An Application in Neuropsychology". In: *Proceedings of the 31st Annual Conference of the Cognitive Science Society*. Amsterdam, Netherlands, 2009, pp. 2675–2680. URL: escholarship.org/uc/item/1313q32b.

[78] B. I. Prilutsky and D. H. Edwards, eds. *Neuromechanical Modeling of Posture and Locomotion*. Vol. 10. Springer Series in Computational Neuroscience. New York, NY: Springer, 2016. ISBN: 978-1-4939-3266-5. DOI: doi.org/10.1007/978-1-4939-3267-2.

[79] G. B. Wilkerson, D. R. Grooms, and S. N. Acocello. "Neuromechanical considerations for postconcussion musculoskeletal injury risk management". In: *Current Sports Medicine Reports* 16.6 (2017), pp. 419–427. DOI: doi.org/10.1249/JSR.0000000000000430.

[80] P. Technology. *Pison Technology: Enabling Effortless Human-Machine Interaction*. pison.com.

[81] G. Durandau, D. Farina, G. Asín-Prieto, I. Dimbwadyo-Terrer, S. Lerma-Lara, J. L. Pons, J. C. Moreno, and M. Sartori. "Voluntary control of wearable robotic exoskeletons by patients with paresis via neuromechanical modeling". In: *Journal of NeuroEngineering and Rehabilitation* 16 (1 July 2019). ISSN: 17430003. DOI: doi.org/10.1186/s12984-019-0559-z.

[82] F. C. Fernandez and W. Caarls. "Deep reinforcement learning for haptic shared control in unknown tasks". In: *arXiv propteprint arXiv:2101.06227* (2021). DOI: doi.org/10.48550/arXiv.2101.06227.

[83] J. E. Britt, M. K. O'Malley, and C. G. Rose. "Electromyographic Classification to Control the SPAR Glove". In: *IFAC-PapersOnLine*. Vol. 54. Elsevier B.V., Nov. 2021, pp. 244–250. DOI: doi.org/10.1016/j.ifacol.2021.11.182.

[84] L. Marchal-Crespo and D. J. Reinkensmeyer. "Review of control strategies for robotic movement training after neurologic injury". In: *Journal of NeuroEngineering and Rehabilitation* 6 (1 2009). ISSN: 17430003. DOI: doi.org/10.1186/1743-0003-6-20.

[85] J. L. Emken, R. Benitez, and D. J. Reinkensmeyer. "Human-robot cooperative movement training: Learning a novel sensory motor transformation during walking with robotic assistance-as-needed". In: *Journal of NeuroEngineering and Rehabilitation* 4 (2007). ISSN: 17430003. DOI: doi.org/10.1186/1743-0003-4-8.

[86] J. L. Patton, M. E. Stoykov, M. Kovic, and F. A. Mussa-Ivaldi. "Evaluation of robotic training forces that either enhance or reduce error in chronic hemiparetic stroke survivors". In: *Experimental Brain Research* 168 (3 Jan. 2006), pp. 368–383. ISSN: 00144819. DOI: doi.org/10.1007/s00221-005-0097-8.

[87] R. E. Singh, K. Iqbal, G. White, and T. E. Hutchinson. “A systematic review on muscle synergies: From building blocks of motor behavior to a neurorehabilitation tool”. In: *Applied Bionics and Biomechanics* 2018 (2018). ISSN: 17542103. DOI: doi.org/10.1155/2018/3615368.

[88] K. P. Kording and D. M. Wolpert. “Bayesian integration in sensorimotor learning”. In: *Nature* 427.6971 (2004), pp. 244–247.

[89] V. C. Cheung, A. Turolla, M. Agostini, S. Silvoni, C. Bennis, P. Kasi, S. Paganoni, P. Bonato, and E. Bizzi. “Muscle synergy patterns as physiological markers of motor cortical damage”. In: *Proceedings of the National Academy of Sciences of the United States of America* 109 (36 Aug. 2012), pp. 14652–14656. ISSN: 10916490. DOI: doi.org/10.1073/pnas.1212056109.

[90] J. Roh, W. Z. Rymer, E. J. Perreault, S. B. Yoo, and R. F. Beer. “Alterations in upper limb muscle synergy structure in chronic stroke survivors”. In: *J Neurophysiol* 109 (2013), pp. 768–781. DOI: doi.org/10.1152/jn.00670.2012.-Previous.

[91] J. Taborri, V. Agostini, P. K. Artemiadis, M. Ghislieri, D. A. Jacobs, J. Roh, and S. Rossi. “Feasibility of muscle synergy outcomes in clinics, robotics, and sports: a systematic review”. In: *Applied bionics and biomechanics* 2018.1 (2018), p. 3934698. DOI: doi.org/10.1155/2018/3934698.

[92] C. Brambilla, M. Atzori, H. Müller, A. d’Avella, and A. Scano. “Spatial and Temporal Muscle Synergies Provide a Dual Characterization of Low-dimensional and Intermittent Control of Upper-limb Movements”. In: *Neuroscience* 514 (Mar. 2023), pp. 100–122. ISSN: 18737544. DOI: doi.org/10.1016/j.neuroscience.2023.01.017.

[93] M. F. Rabbi, C. Pizzolato, D. G. Lloyd, C. P. Carty, D. Devaprakash, and L. E. Diamond. “Non-negative matrix factorisation is the most appropriate method for extraction of muscle synergies in walking and running”. In: *Scientific Reports* 10 (1 Dec. 2020). ISSN: 20452322. DOI: doi.org/10.1038/s41598-020-65257-w.

[94] K. E. Madden, D. Djurdjanovic, and A. D. Deshpande. “Using a system-based monitoring paradigm to assess fatigue during submaximal static exercise of the elbow extensor muscles”. In: *Sensors (Switzerland)* 21 (4 Feb. 2021), pp. 1–23. ISSN: 14248220. DOI: doi.org/10.3390/s21041024.

[95] I. Delis, A. Onken, P. G. Schyns, S. Panzeri, and M. G. Philiastides. “Space-by-time decomposition for single-trial decoding of M/EEG activity”. In: *NeuroImage* 133 (June 2016), pp. 504–515. ISSN: 10959572. DOI: doi.org/10.1016/j.neuroimage.2016.03.043.

[96] R. B. N. Swamy. “Sparse topical analysis of dyadic data using matrix tri-factorization”. In: *Machine Learning* 104 (2-3 Sept. 2016), pp. 441–466. ISSN: 15730565. DOI: doi.org/10.1007/s10994-015-5537-5.

[97] B. Hajiloo, M. Anbarian, H. Esmaeili, and M. Mirzapour. “The effects of fatigue on synergy of selected lower limb muscles during running”. In: *Journal of Biomechanics* 103 (Apr. 2020). ISSN: 18732380. DOI: doi.org/10.1016/j.jbiomech.2020.109692.

[98] J. Zeng, Y. Zhou, Y. Yang, J. Yan, and H. Liu. “Fatigue-Sensitivity Comparison of sEMG and A-Mode Ultrasound based Hand Gesture Recognition”. In: *IEEE Journal of Biomedical and Health Informatics* 26 (4 Apr. 2022), pp. 1718–1725. ISSN: 21682208. DOI: doi.org/10.1109/JBHI.2021.3122277.

[99] G. Li, M. S. Shourijeh, D. Ao, C. Patten, and B. J. Fregly. “How Well Do Commonly Used Co-contraction Indices Approximate Lower Limb Joint Stiffness Trends During Gait for Individuals Post-stroke?” In: *Frontiers in Bioengineering and Biotechnology* 8 (Jan. 2021). ISSN: 22964185. DOI: doi.org/10.3389/fbioe.2020.588908.

[100] C. Ding, T. Li, W. Peng, and H. Park. “Orthogonal nonnegative matrix t-factorizations for clustering”. In: (2006), pp. 126–135. DOI: doi.org/10.1145/1150402.1150420.

[101] N. Hogan. “Impedance Control: An Approach to Manipulation”. In: *1984 American Control Conference*. 1984, pp. 304–313. DOI: doi.org/10.23919/ACC.1984.4788393.

[102] D. M. Wolpert, R. C. Miall, and M. Kawato. “Internal models in the cerebellum”. In: *Trends in cognitive sciences* 2.9 (1998), pp. 338–347. DOI: doi.org/10.1016/S1364-6613(98)01221-2.

[103] D. M. Wolpert, J. Diedrichsen, and J. R. Flanagan. “Principles of sensorimotor learning”. In: *Nature Reviews Neuroscience* 12 (12 Dec. 2011). ISSN: 1471003X. DOI: doi.org/10.1038/nrn3112.

[104] R. Shadmehr and F. A. Mussa-Ivaldi. “Adaptive representation of dynamics during learning of a motor task”. In: *Journal of neuroscience* 14.5 (1994), pp. 3208–3224. DOI: doi.org/10.1523/JNEUROSCI.14-05-03208.1994.

[105] R. S. Johansson and Å. B. Vallbo. “Tactile sensory coding in the glabrous skin of the human hand”. In: *Trends in neurosciences* 6 (1983), pp. 27–32. DOI: doi.org/10.1016/0166-2236(83)90011-5.

[106] M. M. Merzenich and T. Harrington. “The sense of flutter-vibration evoked by stimulation of the hairy skin of primates: comparison of human sensory capacity with the responses of mechanoreceptive afferents innervating the hairy skin of monkeys”. In: *Experimental Brain Research* 9.3 (1969), pp. 236–260. DOI: doi.org/10.1007/BF00234457.

[107] V. B. Mountcastle. *The Sensory Hand: Neural Mechanisms of Somatic Sensation*. Cambridge, MA and London, England: Harvard University Press, 2005. ISBN: 9780674019744. DOI: doi.org/10.4159/9780674275447.

[108] E. H. Weber. *E.H. Weber on the Tactile Senses*. Ed. by D. J. Murray and H. E. Ross. Hove, UK: Psychology Press, 1996. ISBN: 9780863774218. URL: www.routledge.com/EH-Weber-On-The-Tactile-Senses/Murray-Ross/p/book/9780863774218.

[109] S. S. Stevens. “On the Psychophysical Law”. In: *Psychological Review* 64.3 (1957), pp. 153–181. DOI: doi.org/10.1037/h0046162.

[110] A. Prochazka. “Proprioceptive Feedback and Movement Regulation”. In: *Comprehensive Physiology*. Wiley, Dec. 1996, pp. 89–127. DOI: doi.org/10.1002/cphy.cp120103.

[111] G. Macefield, S. C. Gandevia, and D. Burke. “Conduction velocities of muscle and cutaneous afferents in the upper and lower limbs of human subjects”. In: *Brain* 112.6 (1989), pp. 1519–1532. DOI: doi.org/10.1093/brain/112.6.1519.

[112] H. Forssberg, S. Grillner, and S. Rossignol. “Phase dependent reflex reversal during walking in chronic spinal cats”. In: *Brain research* 85.1 (1975), pp. 103–107. DOI: doi.org/10.1016/0006-8993(75)91013-6.

[113] K. G. Pearson. “Proprioceptive regulation of locomotion”. In: *Current opinion in neurobiology* 5.6 (1995), pp. 786–791. DOI: doi.org/10.1016/0959-4388(95)80107-3.

[114] S. Rossignol, R. Dubuc, and J.-P. Gossard. “Dynamic sensorimotor interactions in locomotion”. In: *Physiological reviews* 86.1 (2006), pp. 89–154. DOI: doi.org/10.1152/physrev.00028.2005.

[115] J. Duysens and K. Pearson. “Inhibition of flexor burst generation by loading ankle extensor muscles in walking cats”. In: *Brain Research* 187.2 (1980), pp. 321–332. ISSN: 0006-8993. DOI: doi.org/10.1016/0006-8993(80)90206-1.

[116] A. R. Mayer, Z. Yang, R. A. Yeo, A. Pena, J. M. Ling, M. V. Mannell, M. Stippler, and K. Mojtahed. “A Functional MRI Study of Multimodal Selective Attention Following Mild Traumatic Brain Injury”. In: *Brain Imaging and Behavior* 6.3 (2012), pp. 343–354. DOI: 10.1007/s11682-012-9178-z.

[117] M. C. Möller, L. E. Nordin, A. Bartfai, P. Julin, and T.-Q. Li. “Fatigue and Cognitive Fatigability in Mild Traumatic Brain Injury are Correlated with Altered Neural Activity

during Vigilance Test Performance". In: *Frontiers in Neurology* Volume 8 - 2017 (2017). ISSN: 1664-2295. DOI: doi.org/10.3389/fneur.2017.00496.

[118] M. O. Ernst. *A Bayesian View on Multimodal Cue Integration*. Ed. by G. Knoblich, I. Thornton, M. Grosjean, and M. Shiffrar. Oxford University Press, 2006, pp. 105–131. URL: books.google.com/books?hl=en&lr=&id=iRkCDYXRRX0C&oi=fnd&pg=PA105.

[119] C. M. Harris and D. M. Wolpert. "Signal-dependent noise determines motor planning". In: *Nature* 394.6695 (1998), pp. 780–784. DOI: doi.org/10.1038/29528.

[120] M. A. Guadagnoll and T. D. Lee. "Challenge Point: A Framework for Conceptualizing the Effects of Various Practice Conditions in Motor Learning". In: *Journal of Motor Behavior* 36 (2 June 2004), pp. 212–224. ISSN: 00222895. DOI: doi.org/10.3200/JMBR.36.2.212-224.

[121] G. Wulf, C. Shea, and J. H. Park. "Attention and motor performance: Preferences for and advantages of an external focus". In: *Research Quarterly for Exercise and Sport* 72 (4 2001), pp. 335–344. ISSN: 21683824. DOI: doi.org/10.1080/02701367.2001.10608970.

[122] R. F. Stengel. *Optimal Control and Estimation*. Mineola, NY: Dover Publications, 1994. ISBN: 9780486682006. URL: stengel.mycpanel.princeton.edu/OptConEst.html.

[123] V. Shute, S. Rahimi, and B. Emihovich. "Assessment for Learning in Immersive Environments". In: *Virtual, Augmented, and Mixed Realities in Education*. Singapore: Springer Singapore, 2017, pp. 71–87. ISBN: 978-981-10-5490-7. DOI: doi.org/10.1007/978-981-10-5490-7_5.

[124] D. E. Rumelhart, J. L. McClelland, and P. R. Group. *Parallel Distributed Processing: Explorations in the Microstructure of Cognition, Volume 1: Foundations*. Cambridge, MA:

MIT Press, 1986. ISBN: 9780262181204. DOI: doi.org/10.7551/mitpress/5236.001.0001.

[125] V. C. Cheung, B. M. Cheung, J. H. Zhang, Z. Y. Chan, S. C. Ha, C. Y. Chen, and R. T. Cheung. "Plasticity of muscle synergies through fractionation and merging during development and training of human runners". In: *Nature Communications* 11 (1 Dec. 2020). ISSN: 20411723. DOI: doi.org/10.1038/s41467-020-18210-4.

[126] H. L. Heung, Z. Q. Tang, X. Q. Shi, K. Y. Tong, and Z. Li. "Soft Rehabilitation Actuator With Integrated Post-stroke Finger Spasticity Evaluation". In: *Frontiers in Bioengineering and Biotechnology* 8 (Feb. 2020). ISSN: 22964185. DOI: doi.org/10.3389/fbioe.2020.00111.

[127] D. Kawahara, S. Ozeki, and I. Mizuuchi. "A Curiosity Algorithm for Robots Based on the Free Energy Principle". In: *2022 IEEE/SICE International Symposium on System Integration, SII 2022*. Institute of Electrical and Electronics Engineers Inc., 2022, pp. 53–59. ISBN: 9781665445405. DOI: doi.org/10.1109/SII52469.2022.9708819.

[128] W. C. Cheung. "Exploration-Exploitation Trade-off in Reinforcement Learning on Online Markov Decision Processes with Global Concave Rewards". In: *arXiv preprint arXiv:1905.06466* (2019). DOI: 10.48550/arXiv.1905.06466.

[129] J. Kober, J. A. Bagnell, and J. Peters. "Reinforcement learning in robotics: A survey". In: *International Journal of Robotics Research* 32 (11 Sept. 2013), pp. 1238–1274. ISSN: 02783649. DOI: doi.org/10.1177/0278364913495721.

[130] A. Isaly, B. C. Allen, R. G. Sanfelice, and W. E. Dixon. "Zeroing Control Barrier Functions for Safe Volitional Pedaling in a Motorized Cycle". In: *IFAC-PapersOnLine*. Vol. 53. Elsevier B.V., 2020, pp. 218–223. DOI: doi.org/10.1016/j.ifacol.2021.04.100.

[131] Y. Zhang, B. Zhao, and D. Liu. "Deterministic policy gradient adaptive dynamic programming for model-free optimal control". In: *Neurocomputing* 387 (Apr. 2020), pp. 40–50. ISSN: 18728286. DOI: doi.org/10.1016/j.neucom.2019.11.032.

[132] R. Amit, R. Meir, and K. Ciosek. “Discount Factor as a Regularizer in Reinforcement Learning”. In: Proceedings of Machine Learning Research 119 (2020), pp. 269–278. DOI: 10.48550/arXiv.2007.02040.

[133] M. Pirotta, M. Restelli, and L. Bascetta. “Adaptive Step-Size for Policy Gradient Methods”. In: 26 (2013). Ed. by C. J. C. Burges, L. Bottou, M. Welling, Z. Ghahramani, and K. Q. Weinberger, pp. 1394–1402.

[134] M. Tsao, R. Iglesias, and M. Pavone. *Stochastic Model Predictive Control for Autonomous Mobility on Demand*. 2018. ISBN: 9781728103235. DOI: doi.org/10.0/Linux-x86_64.

[135] S. Arimoto, H. Hashiguchi, M. Sekimoto, and R. Ozawa. “Generation of natural motions for redundant multi-joint system: A differential-geometric approach based upon the principle of least actions”. In: *Journal of Robotic Systems* 22 (11 Nov. 2005), pp. 583–605. ISSN: 07412223. DOI: doi.org/10.1002/rob.20086.

[136] J. Wang, S. Sun, and Y. Sun. “A muscle fatigue classification model based on lstm and improved wavelet packet threshold”. In: *Sensors* 21 (19 Oct. 2021). ISSN: 14248220. DOI: doi.org/10.3390/s21196369.

[137] A. J. Lew and M. J. Buehler. “Encoding and exploring latent design space of optimal material structures via a VAE-LSTM model”. In: *Forces in Mechanics* 5 (Nov. 2021). ISSN: 26663597. DOI: doi.org/10.1016/j.finmec.2021.100054.

[138] D. Buongiorno, C. Camardella, G. D. Cascarano, L. Pelaez Murciego, M. Barsotti, I. De Feudis, A. Frisoli, and V. Bevilacqua. “An undercomplete autoencoder to extract muscle synergies for motor intention detection”. In: *2019 International Joint Conference on Neural Networks (IJCNN)*. 2019, pp. 1–8. DOI: doi.org/10.1109/IJCNN.2019.8851975.

[139] C. Ma, C. Lin, O. W. Samuel, W. Guo, H. Zhang, S. Greenwald, L. Xu, and G. Li. “A Bi-Directional LSTM Network for Estimating Continuous Upper Limb Movement from

Surface Electromyography". In: *IEEE Robotics and Automation Letters* 6 (4 Oct. 2021), pp. 7217–7224. ISSN: 23773766. DOI: doi.org/10.1109/LRA.2021.3097272.

[140] Y. Li, Z. Chen, D. Zha, M. Du, J. Ni, D. Zhang, H. Chen, and X. Hu. "Towards Learning Disentangled Representations for Time Series". In: *Proceedings of the ACM SIGKDD International Conference on Knowledge Discovery and Data Mining*. Association for Computing Machinery, Aug. 2022, pp. 3270–3278. ISBN: 9781450393850. DOI: doi.org/10.1145/3534678.3539140.

[141] The MathWorks, Inc. *Reinforcement Learning Toolbox, Version 2.3 (R2022b)*. www.mathworks.com/products/reinforcement-learning.html. Natick, Massachusetts, USA, 2022.

[142] C. Maher, S. Yoon, S. Donovan, and R. J. Mendonca. "Reliability of the Bulb Dynamometer for Assessing Grip Strength". In: *The Open Journal of Occupational Therapy* 6 (2 Apr. 2018). DOI: doi.org/10.15453/2168-6408.1404.

[143] Z. Wan, N. Chandramoorthy, K. Swaminathan, P. Y. Chen, V. J. Reddi, and A. Raychowdhury. "BERRY: Bit Error Robustness for Energy-Efficient Reinforcement Learning-Based Autonomous Systems". In: *Proceedings - Design Automation Conference*. Vol. 2023-July. Institute of Electrical and Electronics Engineers Inc., 2023. ISBN: 9798350323481. DOI: doi.org/10.1109/DAC56929.2023.10247999.

[144] H. Zhu, J. Yu, A. Gupta, D. Shah, K. Hartikainen, A. Singh, V. Kumar, and S. Levine. "The Ingredients of Real-World Robotic Reinforcement Learning". In: *arXiv preprint arXiv:2004.12570* (2020). DOI: 10.48550/arXiv.2004.12570.

[145] E. D. Oña, A. Jardón, and C. Balaguer. "The automated box and blocks test an autonomous assessment method of gross manual dexterity in stroke rehabilitation". In: *Lecture Notes in Computer Science (including subseries Lecture Notes in Artificial Intelligence and Lecture Notes in Bioinformatics)*. Vol. 10454 LNAI. Springer Verlag, 2017, pp. 101–114. ISBN: 9783319641065. DOI: doi.org/10.1007/978-3-319-64107-2_9.

[146] P. H. Kuo and A. D. Deshpande. “Muscle-tendon units provide limited contributions to the passive stiffness of the index finger metacarpophalangeal joint”. In: *Journal of Biomechanics* 45 (15 Oct. 2012), pp. 2531–2538. ISSN: 00219290. DOI: doi.org/10.1016/j.jbiomech.2012.07.034.

[147] E. Colamarino, V. D. Seta, J. Toppi, F. Pichiorri, I. Conforti, I. Mileti, E. Palermo, D. Mattia, and F. Cincotti. “Distinctive physiological muscle synergy patterns define the Box and Block Task execution as revealed by electromyographic features”. In: *Proceedings of the Annual International Conference of the IEEE Engineering in Medicine and Biology Society, EMBS*. Vol. 2022-July. Institute of Electrical and Electronics Engineers Inc., 2022, pp. 5124–5127. ISBN: 9781728127828. DOI: doi.org/10.1109/EMBC48229.2022.9871699.

[148] J. S. Hebert and J. Lewicke. “Case report of modified box and blocks test with motion capture to measure prosthetic function”. In: *Journal of Rehabilitation Research and Development* 49 (8 2012), pp. 1163–1174. ISSN: 07487711. DOI: doi.org/10.1682/JRRD.2011.10.0207.

[149] M. L. Canny, J. M. Thompson, and M. J. Wheeler. “Reliability of the Box and Block Test of Manual Dexterity for Use With Patients With Fibromyalgia”. In: *The American Journal of Occupational Therapy* 63.4 (July 2009), pp. 506–510. ISSN: 0272-9490. DOI: doi.org/10.5014/ajot.63.4.506.

[150] A. Buryanov and V. Kotiuk. “Proportions of Hand Segments”. In: *International Journal of Morphology* 28 (3 Sept. 2010). DOI: doi.org/10.4067/s0717-95022010000300015.

[151] X. Q. Shi, H. L. Heung, Z. Q. Tang, K. Y. Tong, and Z. Li. “Verification of Finger Joint Stiffness Estimation Method With Soft Robotic Actuator”. In: *Frontiers in Bioengineering and Biotechnology* 8 (Dec. 2020). ISSN: 22964185. DOI: doi.org/10.3389/fbioe.2020.592637.

[152] 3D Systems, Inc. “Touch Haptic Device”. In: (2025). Accessed: 2025-04-19.

[153] N. Bhatt and S. K. Varadhan. “Posture similarity index: A method to compare hand postures in synergy space”. In: *PeerJ* 2018 (12 2018). ISSN: 21678359. DOI: doi.org/10.7717/peerj.6078.

[154] M. S. Norberto, T. B. de Arruda, and M. Papoti. “A New Approach to Evaluate Neuromuscular Fatigue of Extensor Elbow Muscles”. In: *Frontiers in Physiology* 11 (Sept. 2020). ISSN: 1664042X. DOI: doi.org/10.3389/fphys.2020.553296.

[155] J.-H. Kim, Y. Kim, J. Lee, K. M. Yoo, and S.-W. Lee. “Mutual Information Divergence: A Unified Metric for Multimodal Generative Models”. In: 35 (2022). Ed. by S. Koyejo, S. Mohamed, A. Agarwal, D. Belgrave, K. Cho, and A. Oh, pp. 35072–35086.

[156] A. Baskaran, P. Esmatloo, M. Times, A. D. Deshpande, and C. G. Rose. “An anthropomorphic passive instrumented hand for validating wearable robotic systems”. In: *IEEE/ASME International Conference on Advanced Intelligent Mechatronics, AIM*. Vol. 2021-July. Institute of Electrical and Electronics Engineers Inc., July 2021, pp. 134–139. ISBN: 9781665441391. DOI: doi.org/10.1109/AIM46487.2021.9517589.

[157] Amazon.com. “Rehabilitation Robot Gloves Hand Stroke Recovery Equipment”. In: (2022). Accessed: 2022-11-05.

[158] M. Millard, M. Sreenivasa, and K. Mombaur. “Predicting the motions and forces of wearable robotic systems using optimal control”. In: *Frontiers Robotics AI* 4 (AUG Aug. 2017). ISSN: 22969144. DOI: doi.org/10.3389/frobt.2017.00041.

[159] J. M. Inouye and F. J. Valero-Cuevas. “Muscle Synergies Heavily Influence the Neural Control of Arm Endpoint Stiffness and Energy Consumption”. In: *PLoS Computational Biology* 12 (2 Feb. 2016). ISSN: 15537358. DOI: doi.org/10.1371/journal.pcbi.1004737.

[160] R. S. Johansson and J. R. Flanagan. “Coding and use of tactile signals from the fingertips in object manipulation tasks”. In: *Nature Reviews Neuroscience* 10 (5 May 2009), pp. 345–359. ISSN: 1471003X. DOI: doi.org/10.1038/nrn2621.

[161] J. Lieberman and C. Breazeal. “TIKL: Development of a wearable vibrotactile feedback suit for improved human motor learning”. In: *IEEE Transactions on Robotics*. Vol. 23. Oct. 2007, pp. 919–926. DOI: doi.org/10.1109/TRO.2007.907481.

[162] A. Frisoli, M. Solazzi, M. Reiner, and M. Bergamasco. “The contribution of cutaneous and kinesthetic sensory modalities in haptic perception of orientation”. In: *Brain Research Bulletin* 85 (5 June 2011), pp. 260–266. ISSN: 03619230. DOI: doi.org/10.1016/j.brainresbull.2010.11.011.

[163] C. J. Winstein and R. A. Schmidt. “Reduced Frequency of Knowledge of Results Enhances Motor Skill Learning”. In: *Journal of Experimental Psychology: Learning, Memory, and Cognition* 16.4 (1990), pp. 677–691. DOI: doi.org/10.1037/0278-7393.16.4.677.

[164] K. Wei and K. Körding. “Uncertainty of feedback and state estimation determines the speed of motor adaptation”. In: *Frontiers in Computational Neuroscience* 4 (2010), pp. 1–9. ISSN: 16625188. DOI: doi.org/10.3389/fncom.2010.00011.

[165] P. Kormushev, S. Calinon, and D. G. Caldwell. “Reinforcement learning in robotics: Applications and real-world challenges”. In: *Robotics* 2 (3 Sept. 2013), pp. 122–148. ISSN: 22186581. DOI: doi.org/10.3390/robotics2030122.

[166] T. P. Lillicrap, J. J. Hunt, A. Pritzel, N. Heess, T. Erez, Y. Tassa, D. Silver, and D. Wierstra. “Continuous Control with Deep Reinforcement Learning”. In: *arXiv preprint arXiv:1509.02971* (2015). DOI: doi.org/10.48550/arXiv.1509.02971.

[167] G. R. Müller-Putz, R. J. Kobler, J. Pereira, C. Lopes-Dias, L. Hehenberger, V. Mondini, V. Martínez-Cagigal, N. Srisrisawang, H. Pulferer, L. Batistić, and A. I. Sburlea. “Feel Your Reach: An EEG-Based Framework to Continuously Detect Goal-Directed Movements and Error Processing to Gate Kinesthetic Feedback Informed Artificial Arm Control”. In: *Frontiers in Human Neuroscience* 16 (2022), p. 841312. DOI: doi.org/10.3389/fnhum.2022.841312.

[168] N. Srinivas, A. Krause, S. M. Kakade, and M. Seeger. “Gaussian Process Optimization in the Bandit Setting: No Regret and Experimental Design”. In: *arXiv preprint arXiv:0912.3995* (2009). DOI: doi.org/10.48550/arXiv.0912.3995.

[169] C. Finn, P. Abbeel, and S. Levine. “Model-Agnostic Meta-Learning for Fast Adaptation of Deep Networks”. In: *Proceedings of the 34th International Conference on Machine Learning*. Ed. by D. Precup and Y. W. Teh. Vol. 70. Proceedings of Machine Learning Research. PMLR, June 2017, pp. 1126–1135. URL: proceedings.mlr.press/v70/finn17a.html.

[170] T. Shahid, D. Gouwanda, S. G. Nurzaman, and A. A. Gopalai. “Moving toward soft robotics: A decade review of the design of hand exoskeletons”. In: *Biomimetics* 3 (3 Sept. 2018). ISSN: 23137673. DOI: doi.org/10.3390/biomimetics3030017.

[171] M. Dežman, S. Massardi, D. Pinto-Fernandez, V. Grosu, C. Rodriguez-Guerrero, J. Babič, and D. Torricelli. “A mechatronic leg replica to benchmark human–exoskeleton physical interactions”. In: *Bioinspiration and Biomimetics* 18 (3 May 2023). ISSN: 17483190. DOI: doi.org/10.1088/1748-3190/accda8.

[172] S. N. Yousaf, V. S. Joshi, J. E. Britt, C. G. Rose, and M. K. O’Malley. “Design and Characterization of a Passive Instrumented Hand”. In: *ASME Letters in Dynamic Systems and Control* 1 (1 Jan. 2021). ISSN: 2689-6117. DOI: doi.org/10.1115/1.4046449.

[173] O. A. M. Andrychowicz, B. Baker, M. Chociej, R. Józefowicz, B. McGrew, J. Pachocki, A. Petron, M. Plappert, G. Powell, A. Ray, J. Schneider, S. Sidor, J. Tobin, P. Welinder, L. Weng, and W. Zaremba. “Learning dexterous in-hand manipulation”. In: *International Journal of Robotics Research* 39 (1 Jan. 2020), pp. 3–20. ISSN: 17413176. DOI: doi.org/10.1177/0278364919887447.

[174] J. Butterfass, M. Grebenstein, H. Liu, and G. Hirzinger. “DLR-Hand II: next generation of a dextrous robot hand”. In: 1 (2001), 109–114 vol.1. DOI: doi.org/10.1109/ROBOT.2001.932538.

[175] C. Alessandro, I. Delis, F. Nori, S. Panzeri, and B. Berret. “Muscle synergies in neuroscience and robotics: From input-space to task-space perspectives”. In: *Frontiers in Computational Neuroscience* (APR 2013 Apr. 2013). ISSN: 16625188. DOI: doi.org/10.3389/fncom.2013.00043.

[176] P.-H. Kuo, J. DeBacker, and A. D. Deshpande. “Design of robotic fingers with human-like passive parallel compliance”. In: *2015 IEEE International Conference on Robotics and Automation (ICRA)*. 2015, pp. 2562–2567. DOI: doi.org/10.1109/ICRA.2015.7139543.

[177] Y. Liu, Z. Li, H. Liu, and Z. Kan. “Skill transfer learning for autonomous robots and human–robot cooperation: A survey”. In: *Robotics and Autonomous Systems* 128 (2020), p. 103515. ISSN: 0921-8890. DOI: doi.org/10.1016/j.robot.2020.103515.

[178] J. Chen and H. Qiao. “Muscle-Synergies-Based Neuromuscular Control for Motion Learning and Generalization of a Musculoskeletal System”. In: *IEEE Transactions on Systems, Man, and Cybernetics: Systems* 51 (6 June 2021), pp. 3993–4006. ISSN: 21682232. DOI: doi.org/10.1109/TSMC.2020.2966818.

[179] M. S. Shourijeh and B. J. Fregly. “Muscle synergies modify optimization estimates of joint stiffness during walking”. In: *Journal of Biomechanical Engineering* 142 (1 Jan. 2020). ISSN: 15288951. DOI: doi.org/10.1115/1.4044310.

[180] K. Zhao, Z. Zhang, H. Wen, and A. Scano. “Intra-subject and inter-subject movement variability quantified with muscle synergies in upper-limb reaching movements”. In: *Biomimetics* 6 (4 Dec. 2021). DOI: doi.org/10.3390/biomimetics6040063.

[181] S. Mitra, M. A. Riley, R. C. Schmidt, and M. T. Turvey. “Vision and the Level of Synergies”. In: (1998). Ed. by L. R. Harris and M. Jenkin, pp. 314–331. URL: books.google.com/books?id=SeywHSh2YKkC&pg=PA314.

[182] C. Manzie and M. Krstic. “Extremum Seeking With Stochastic Perturbations”. In: *IEEE Transactions on Automatic Control* 54.3 (2009), pp. 580–585. DOI: doi.org/10.1109/TAC.2008.2008320.

[183] R. Pintelon and J. Schoukens. *System Identification: A Frequency Domain Approach*. New York: Wiley-IEEE Press, 2001. ISBN: 978-0780360006. DOI: 10.1002/0471723134. URL: www.wiley.com/en-us/System+Identification%3A+A+Frequency+Domain+Approach%2C+2nd+Edition-p-x000546362.